PHYSICAL REVIEW VOLUME 145, NUMBER 1 6 MAY 1966

Second-Harmonic Generation of Light by Focused Laser Beams

D. A. KLEINMAN, A. ASHKIN, AND G. D. BOYD
Bell Telephone Laboratories, Murray Hill, New Jersey

(Received 22 October 1965)

An experimental and theoretical study is reported on second-harmonic generation (SHG) by focused laser beams in nonlinear crystals which are large compared with the extent of the focus. The gas-laser beam is in the lowest order (Gaussian) mode and very close to index-matching conditions in the crystal. The intensity pattern of the SHG observed photographically has roughly the shape of a half moon with a very sharp edge. The distribution on the bright side of the edge has been measured using a traveling slit and photomultiplier detector. Fine structure has been observed consisting of a series of fringes extending from the edge into the bright region. The nature of the fine structure depends upon where the pattern is observed. The pattern at the surface of the crystal has fringes at the positions one would expect for diffraction of a second-harmonic beam by a straight-edged screen placed at the focus. The pattern at great distance from the crystal has uniformly spaced fringes; in this case fringes have also been seen on the dim side of the edge. It has been shown that the position of the edge relative to the axis of the laser beam is sensitive to extremely fine adjustments of the crystal orientation. The power has also been measured as a function of crystal orientation, and the position of the edge has been determined for the orientation giving maximum power. The theoretical treatment of the problem, which occupies most of the paper, is based upon an exact formula for the second-harmonic field for the case in which the laser beam is in a Guassian mode. In a far-field approximation this formula is decomposed into three types of terms having different dependence upon distance. The leading term in the limit of large distance has a sharp edge and describes the gross behavior on the bright side of the edge. The other terms are associated with fine structure of the Fresnel and Fraunhofer types arising from the focus and the crystal surfaces, respectively. The theory contains a parameter to specify the phase-matching conditions which can be simply related to changes in the crystal orientation. The power is obtained as a function of this parameter, and the optimum matching condition corresponding to maximum power is thereby determined. A detailed analysis of the experimental data is presented which shows the theory to be in quantitative as well as qualitative agreement with experiment.

1. INTRODUCTION

IN a previous paper,[1] hereafter referred to as BADK, we have described the properties of second-harmonic generation (SHG) by *parallel* laser beams in very long crystals. Experimentally this work was an extension of the work of Ashkin, Boyd, and Dziedzic,[2] who demonstrated that under index-matching conditions the gas laser is capable of producing useful amounts of SHG, and used the effect to measure the second-order polarization coefficient d_{36} for potassium dihydrogen phosphate (KDP). The success of these experiments was due to the very long coherence length possible with the gas laser in single-mode operation. The fact that the crystal was an order of magnitude shorter than the estimated coherence length of the beam indicated that new experiments should be carried out using much longer crystals. Previously, it had been pointed out[3] that the effective coherence length (the aperture length) for very parallel beams in perfect crystals would ultimately be limited by *double refraction*, and would be proportional to the aperture of the beam. This double-refraction effect was observed experimentally and found to be in quantitative agreement with theory as reported in BADK. The effect has also been observed in photographs of the SHG by Bhawalkar, Gambling, Smith, and Watkins.[4]

The theory of the double-refraction effect in SHG was given in BADK from two points of view. It was shown first that the standard theory[3,5,6] of SHG by unbounded plane waves can be formulated in such a way that double refraction, absorption, and the finite aperture of the beam can all be introduced in a plausible manner. This *heuristic* approach for parallel beams has the advantage of being intuitive, easy to follow, and relatively nonmathematical. It was applied specifically to the experimental situation in which the fundamental beam is in the Gaussian (lowest order, TEM_{00}) mode of the laser resonator. It could equally well be applied to more complicated modes or to any superposition of modes in the laser beam. The other theoretical point of view presented in BADK was the *formal* approach, which is presumably rigorous in that it rests upon the accepted and well verified theory of SHG by unbounded plane waves without additional assumptions. When the finite aperture of the beam is taken into account by representing the laser and second harmonic beams as Fourier integrals over plane-wave components, it is found that double refraction comes in automatically, and a formula is obtained in agreement with the heuristic theory for the case of a parallel beam.

The assumption of a parallel beam of finite aperture cannot be strictly true, but is an excellent approximation in the region of the focus (minimum beam radius)

---

[1] G. D. Boyd, A. Ashkin, J. M. Dziedzic, and D. A. Kleinman, Phys. Rev. 137, A1305 (1965).

[2] A. Ashkin, G. D. Boyd, and J. M. Dziedzic, Phys. Rev. Letters 11, 14 (1963).

[3] D. A. Kleinman, Phys. Rev. 128, 1761 (1962).

[4] D. D. Bhawalkar, W. A. Gambling, R. C. Smith, and L. S. Watkins, Phys. Letters 15, 220 (1965).

[5] J. A. Armstrong, N. Bloembergen, J. Ducuing, and P. S. Pershan, Phys. Rev. 127, 1918 (1962).

[6] N. Bloembergen and P. S. Pershan, Phys. Rev. 128, 606 (1962).

of a laser employing spherical mirrors of large radius of curvature. The experiments reported in BADK were carried out in the *near field*, the region sufficiently near to the focus that the laser beam is essentially parallel. In the *far field* at much greater distances from the focus the beam eventually diverges with a constant diffraction angle inversely proportional to the minimum spot size of the beam.[7] Ordinarily the beam emerging from a gas laser[1] has a very long near field (~300 cm), a correspondingly small diffraction angle (~0.03°) and a correspondingly large spot size (~0.07 cm) as required by the theory[7] of optical resonators. It is then quite practical as was done in BADK to work in the near field, but relatively difficult to work in the far field. By means of *focusing lenses*, however, it is possible to obtain a very short near field (~0.013 cm) with correspondingly large diffraction angle (~4°) and small spot size ($\sim 5\,\mu$). In this way the far field can be reached in a crystal of reasonable size. Therefore the essential distinction which must be made between SHG by unfocused and by focused beams is the following: In the case of unfocused (parallel) beams interest centers on the near field, while in the case of focused beams it centers on the far field.

Experimentally the motive for focusing has usually been to increase the *intensity* and thereby enhance nonlinear optical effects. Thus, Franken *et al.*,[8] by focusing the beam from a ruby laser in quartz, were able to observe SHG, although index matching was not used and the coherence length was therefore very short ($\sim 14\,\mu$). It was found by Ashkin, Boyd, and Dziedzic,[2] however, that SHG does not increase monotonically as the spot size is reduced and the intensity increased by focusing, but goes through a maximum. They suggest that, under index-matching conditions, the effective coherence length of the beam is inversely proportional to its diffraction angle, and the maximum corresponds to a coherence length comparable to the crystal length. These ideas were sharpened somewhat in BADK, where it was shown that the effective coherence length associated with the diffraction angle is actually identical with the aperture length arising from double refraction. In view of the frequent experimental use of focusing, the ease of reaching the far field within ordinary crystal samples, and the potential importance of the problem of maximizing the nonlinear interactions of light beams, it is clear that a need exists for a discussion of the properties of SHG in the far field under matching conditions, which forms the subject of this paper.

In attempting to arrive at an understanding of these properties we have followed a course guided both by experiment and by theory. To begin with it should be emphasized that the far-field pattern of intensity in SHG is surprisingly complex and completely different from the near-field pattern. There is therefore a complicated transition region between the near and far field in which the intensity pattern undergoes radical changes as the distance from the focus increases. We shall not attempt a general discussion of this intermediate field. The dominant feature of the far-field pattern whenever double refraction is present is a *sharp edge* dividing the pattern into a dim region and a bright region. A *fine structure* can also be seen in both regions. As the distance from the focus increases the edge becomes sharper and the fine structure weaker. Nevertheless, with sufficient exposure an elaborate fine structure can be recorded photographically at any distance from the focus. The fine structure may have a uniform or a nonuniform spacing of fringes. These facts have been observed experimentally, and serve to define the main objectives of the theory which are: (1) to explain the sharp edge in the intensity pattern, (2) describe the gross intensity distribution on the bright side of the edge, and (3) explain and describe the fine structure.

The theory given here proceeds from the formal approach of BADK which is completely general and not limited to parallel beams. As shown in BADK the theory takes into account all mixing effects between plane-wave components of the nonlinear polarization. It is shown that the theory can be cast in a Green's-function formulation which directly relates the second-harmonic electric field to the distribution of polarization producing it. For practical calculations it may be more advantageous to make use of the Fourier transform of the second-harmonic polarization. By either method, an exact formula is obtained for the second-harmonic field for the case in which the laser beam is in a Gaussian mode. The method could also be applied to higher modes, since convenient analytical expressions for all the modes of a confocal resonator have been given by Boyd and Gordon.[7] For small diffraction angles (paraxial approximation) these expressions take the *diffraction* of the laser beam into account exactly. Only the laser beam is assumed to be in a single mode; the theory gives an explicit expression for the second-harmonic field which in general does not correspond to a single mode. The formula obtained here reduces in the near field to that obtained in BADK assuming a parallel beam. Although the formula is valid in the intermediate field, it is difficult to obtain much information from it except for the special case in which double refraction is absent.

The most interesting results of the theory follow from a *far-field approximation* which neglects that part of the field falling off faster than the inverse square of the distance from the focus. The resulting expression is analyzed from the point of view of the three objectives mentioned above. It is decomposed into three types of terms having different dependence upon distance. The leading term in the limit of large distance has a sharp edge and describes the gross behavior of the intensity distribution on the bright side of the edge. This will

---

[7] G. D. Boyd and J. P. Gordon, Bell System Tech. J. **40**, 489 (1961).

[8] P. A. Franken, A. E. Hill, C. W. Peters, and G. Weinreich, Phys. Rev. Letters **7**, 118 (1961).

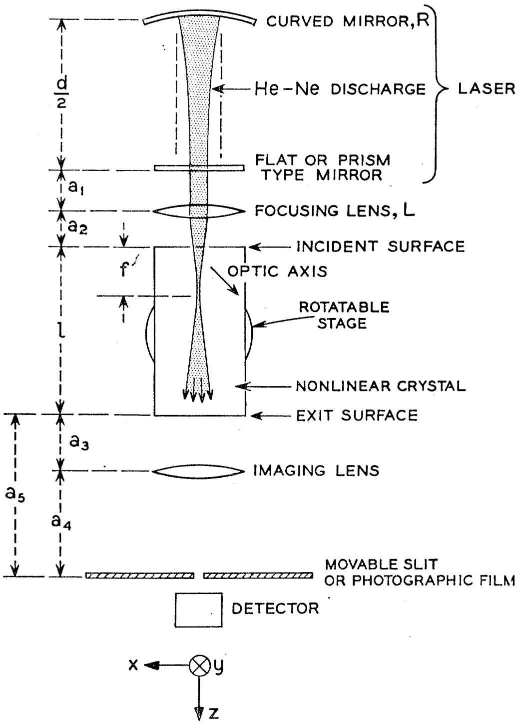

FIG. 1. Experimental arrangement for measuring the SHG by a focused laser beam.

be called the dominant term. The other terms are associated with the structure of the edge and with the surfaces of the crystal, and give rise, through interference with the dominant term and with each other, to two general kinds of fine structure. In this way the theory meets the objectives dictated by experiment. The desire to test the predictions of the theory led to further experiments of a more quantitative nature. The results reported here indicate that theory and experiment are in excellent agreement.

Previously, a theory has been given[3] for SHG by focused beams neglecting double refraction. In this theory the region of the focus was replaced by an appropriate cylindrical volume containing a uniform plane second-harmonic polarization wave. The radiation from this volume into a surrounding isotropic medium was calculated using the standard Green's function of physical optics. This treatment clearly showed the importance of phase matching in SHG by focused beams in both the power and the intensity distribution, but was too crude to predict the effects that have been observed. The theory given here supersedes the previous theory. The "plane wave in a cylinder" approximation has been eliminated and the birefringence of the medium has been retained. All phase-matching (coherence) effects, including double refraction and diffraction, are now contained in the Green's function, which is derived from first principles. The dependence of the intensity and the power upon the matching conditions are discussed in detail.

Experimentally the sharp edge in the intensity pattern has been reported for focused ruby laser beams by Maker, Terhune, Nisenoff, and Savage.[9] These authors explain the effect in terms of the *mixing* of various rays present in the focused beam. The edge presumably corresponds to the matching direction for a ray along the beam axis; on the bright side mixing of off-axis rays can take place under matching conditions, but on the dim side mixing can only take place under nonmatching conditions. For the ruby laser beam which may contain many modes this simple theory may be quite appropriate. In such a case the various Fourier components of the beam may be regarded as essentially uncorrelated, and the second-harmonic waves arising from the various mixing processes are also uncorrelated. When the laser beam is in a single mode, however, this is obviously not the case, and it is not clear to what extent the simple mixing-matching theory applies. For the near field this question was considered in BADK, where it was shown that considering the beam as a diverging pencil of rays gives the correct effective coherence length for the power, but does not give the correct intensity distribution. In the far field, however, we find experimentally and theoretically that a sharp edge is present, so the simple mixing-matching theory is to some extent vindicated. Actually, the sharp edge is observed not along the beam axis but closer to the double-refraction direction through the focus. This might be taken into account in the mixing-matching theory in the manner of the heuristic theory of BADK by postulating that the second harmonic energy propagates (from the focus) along the double-refraction direction. It may also be possible to offer simple explanations for the fine structure similar to those offered by Giordmaine[10] for the fringes he observed under nearly matching conditions with the (unfocused) ruby laser beam. In this paper, however, we have chosen not to digress in this direction but to relate our discussion entirely to the formal theory and the approximations that can be derived from it appropriate for the far field.

Two papers have recently appeared dealing with certain aspects of SHG by focused beams. McMahon and Franklin[11] have given a theoretical formula for the second harmonic field produced by a focused laser beam. Their formula agrees exactly with out result (4.19) for the nominal matching case. This does not correspond to the condition for maximum power, and their criterion for the condition of maximum power disagrees violently with our Fig. 32. Although they give a general integral expression for the power (in the nominal matching case), they discuss this expression only in the near field limit.

---

[9] P. D. Maker, R. W. Terhune, M. Nisenoff, and C. M. Savage, Phys. Rev. Letters 8, 21 (1962).

[10] J. A. Giordmaine, Phys. Rev. Letters 8, 19 (1962).

[11] D. H. McMahon and A. R. Franklin, Appl. Phys. Letters 6, 14 (1965).

Their experimental results are also taken in the near field, and are entirely explained by the aperture effect discussed in BADK. The pattern of intensity in the far field, which is the central problem considered here, is not mentioned. Francois and Siegman[12] have discussed the intensity pattern in the SHG by a Gaussian beam using a Fourier representation of the beam. However, their Fourier representation describes what BADK call a "parallel beam," which is only valid for a crystal which is thin compared with the length of the near field. Therefore their theory does not apply to SHG by a localized focus in a large crystal, the situation considered here.

The reader primarily interested in the experimental results and their interpretation should read Sec. 2 and then proceed directly to Sec. 9, where theory is compared with experiment. In the theoretical development Secs. 3–8, equations of central importance, particularly those containing results that are compared with experiment in Sec. 9, are marked with an asterisk (*). As an aid in reading Sec. 9, especially for those who do not wish to read the theoretical sections carefully, a glossary of notation is provided at the beginning containing all the symbols from the theory that appear in the section. Separate summaries are provided at the ends of Secs. 5, 6, 7, and 8 which together summarize the theory. A brief over-all summary including the comparison with experiment is given at the end of Sec. 9.

2. EXPERIMENTAL TECHNIQUE AND DATA

2.1 Technique

The experimental technique used in this focused beam work is an extension of the gas laser technique described previously.[1,2] The fundamental wavelength chosen for these experiments was the 1.1526-μ line of the He-Ne laser. This creates a harmonic at 0.5763 μ which is readily detected photographically or with a photomultiplier.

Figure 1 shows schematically the basic experimental arrangement used for observing the harmonic output from focused beams. Fundamental power emerges from the laser at the flat mirror in the lowest order transverse mode (a Gaussian beam). For some experiments the simple front-surface mirror sketched in Fig. 1 was replaced by a Brewster prism-type flat mirror. This is essentially a prism-shaped back-surface mirror, the front surface of which makes the Brewster angle with the beam in the resonator. This dispersive type of flat mirror was introduced in order to discourage subsidiary oscillations such as 1.1614, 1.1767, and 1.1985 μ, which fall near the desired 1.1526-μ line, and which can oscillate with as much as 30% of the power at high discharge currents. One side effect, however, of the prism is that the output laser beam is elongated in the y direction (note coordinates in Fig. 1). The Gaussian beam radius in the y direction is increased by n, the index of the prism-type mirror at 1.1526 μ, whereas the Gaussian beam radius in the x direction remains the same as for a simple flat mirror. By adjusting the focal length L of the focusing lens and its distance a_2 from the nonlinear crystal we can focus the fundamental beam to the desired spot size w_0 and depth f in the nonlinear crystal. The angle between the fundamental beam and the crystal optic axis is adjusted for optimum second-harmonic power unless otherwise stated. The crystal is mounted on a rotatable stage described in BADK which can be motor driven. Figure 2 sketches the fundamental beam geometry and the fundamental and harmonic field distributions in qualitative fashion at the exit surface for a strongly focused beam where the near field of the fundamental is a small fraction of the crystal length l.

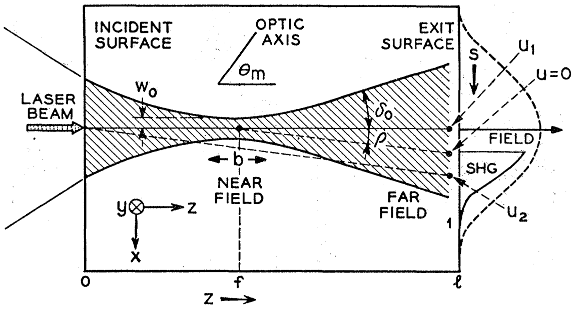

FIG. 2. Fundamental beam (shaded) focused at $z=f$ in a crystal which is much longer than the confocal parameter b of the focus. The spot size is w_0, the far field diffraction half-angle δ_0, and the double refraction angle is ρ. The fundamental field strength at the exit surface $z=l$ is shown dashed in the plot at the right. Also sketched is the second-harmonic field (labeled SHG) according to (5.28) and ρ lines through the focus and the incident point. The variable s is defined in (5.4) and the points $s=u_1$, $s=u_2$ in (5.6).

The Fig. 2 shows two dashed lines making the angle ρ with respect to the beam axis, where ρ is the double refraction angle. As in BADK we call these ρ lines. The one through the focus is particularly useful in visualizing the flow of harmonic power. By means of the imaging lens of Fig. 1, which images the exist surface on the plane of observation, we can measure the harmonic and fundamental intensity distributions suitably enlarged. For accurate measurement of the intensity distributions a combined slit and photomultiplier detector could be scanned across the harmonic or fundamental distributions in the plane of observation. A vertical slit parallel to the y direction was used in all the scanning measurements rather than a pinhole in order to improve the sensitivity. The y distribution of light is Gaussian and all the information of interest is in the x direction as shown in Fig. 2.

The output of the photomultiplier was amplified and fed into a phase-sensitive detector with a suitable time constant. The output of the phase-sensitive detector, which was proportional to the light intensity falling on

---

[12] G. E. Francois and A. E. Siegman, Phys. Rev. **139**, A4 (1965).

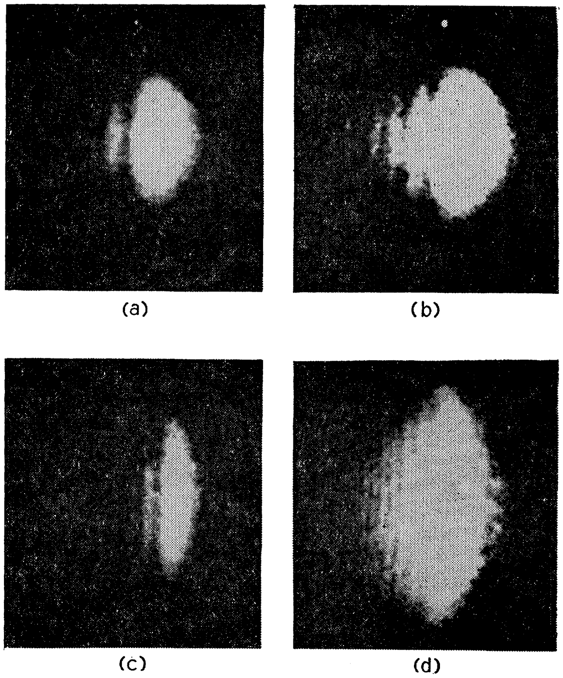

FIG. 3. Photographs showing the SHG by a focused beam in ADP in the intermediate field which show the gradual evolution of the edge from the nearly circular pattern of the near field. The pattern of (a), shown at greater exposure in (b), corresponds to $(l-f)\sim 1.5$b. That of (c), shown at greater exposure in (d), corresponds to $(l-f)\sim 3b$. The edge appears in the shorter exposures as a flattening on the left side. The longer exposures bring out a fine structure which is relatively strong at these intermediate distances, but which becomes very weak in the far field.

the slit, was fed to the y input of an x-y recorder while the x input was driven in synchronism with the movable slit and photomultiplier combination. Thus we obtained plots of the intensity variation in the x direction directly. For photographic detection the movable slit and photomultiplier shown in Fig. 1 were replaced by a photographic film (Polaroid 3000 or 10 000). In some experiments the imaging lens was removed and the fundamental and harmonic intensity distributions were observed after traversing a length of free space a_5. As will be seen this method of observation changes the harmonic intensity distribution in some of its details (fine structure) but not in gross shape.

2.2 Development of Far-Field Pattern

Before describing the far-field distributions in detail, it is instructive to note briefly with the aid of Figs. 3, 4 how the nearly circular harmonic energy distribution for the near field described by BADK transforms to the far-field distribution. Although these intermediate situations will not be studied quantitatively in this paper, the photographs show the gradual evolution of some of the characteristics which will occupy our attention in the far field. In Figs. 3(a) and 3(b) we see photographs taken with two different exposure times of the harmonic output at the exit surface from a fundamental beam of spot radius $w(\text{air})\sim 0.07$ with $L\sim 6$, $a_2\sim 3.5$, $f\sim 3.8$, and $l=5$, where all dimensions are given in centimeters. For these conditions $(l-f)\sim 1.5b$, where b is the confocal parameter (see BADK). Thus we are just entering into the far-field region. We see that the harmonic beam is far from circular. A flattening has developed on one side followed by a series of fringes which are more evident in the longer exposure of Fig. 3(b). We now make $f\sim 2.5$, which makes $(l-f)\sim 3b$ and we are deeper in the far field. The harmonic output is as shown in Figs. 3(c) and 3(d), taken at different exposures. The flattening is now more pronounced and the spacing of the fringes has decreased. The flattening that appears on the gross shape of the harmonic we call the "edge" of the harmonic pattern. This will be defined more precisely in the theoretical treatment. Figure 4 is a photograph displaying both fundamental and harmonic light distributions from an ammonium dihydrogen phosphate (ADP) crystal for a case where we were even further in the far field, $w(\text{air})\sim 0.07$, $L\sim 6$, $f\sim 2$, $l=10.4$, $a_5\sim 20$ (no imaging lens), and $(l-f)\sim 10b$. Since the film used was insensitive to the 1.15-μ fundamental beam used, a translucent phosphorescent card which glowed in the visible was placed in direct contact with the film during the exposure for the fundamental which produced the circular pattern. In addition to showing a more cleanly defined edge and a few even more closely spaced ripples, it shows that double refraction is playing a role inasmuch as the harmonic emerges displaced from the axis of the fundamental beam as sketched in Fig. 2.

2.3 Data

We now proceed to data taken well into the far field where we will look at many of the features observed above in greater detail. The data is given in Figs. 5–16, and the corresponding experimental conditions in the notation of Fig. 1 are specified in Table I. Of interest in Fig. 5 is the position of the harmonic intensity distribution relative to the fundamental beam distribution.

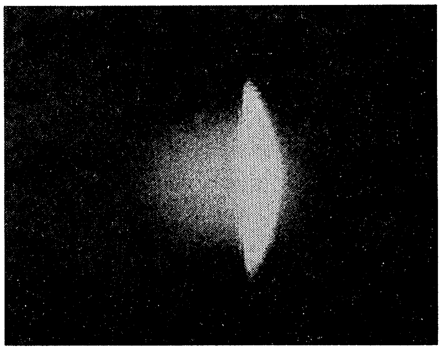

FIG. 4. Photograph showing both the fundamental (circular) and second-harmonic intensity patterns when $(l-f)\sim 10b$. Double refraction in the ADP crystal causes the edge to be displaced from the axis of the fundamental beam.

TABLE I. Experimental constants in the notation of Fig. 1 relevant to the experimental data given in Figs. 5–16. All dimensions are in centimeters.

Fig.	5	6	7	8, 9, 10	11, 12, 13	14, 15, 16
R Cm	5000	5000	5000	5000	5000	300
$d/2$	150	150	150	150	150	150
a_1	69	69	69	69	69	69
L	3.2	3.2	3.2	3.2	3.2	3.2
a_2	0.2	0.2	0.2	0.2	2.8	3.0
l	10.4	10.4	10.4	10.4	1.23	10.4
	ADP	ADP	ADP	ADP	KDP	ADP
a_3	···	6.8	2.8	2.8	···	···
a_4	···	11.0	13.0	18.0	···	···
a_5	0	···	···	···	18	15.8

ADP $n=1.5$, $\rho=0.030$ rad
KDP $n=1.5$, $\rho=0.028$

This is most directly measured by scanning across the distributions with a slit and photomultiplier directly outside the exit surface (no lens, $a_5=0$). For experimental reasons, however, it was necessary to guide the radiation transmitted through the slit to the photomultiplier with a light pipe. This technique gave the desired data in the most straightforward fashion, although it suffered somewhat from poor resolution associated with the small beam size at the exit surface and the high absorption of the Lucite light pipe at 1.15 μ. The sharp rise of harmonic output that occurs as one moves away from the fundamental beam axis is the edge. The beam axis was estimated from the approximately Gaussian fundamental. The ρ line through the focus shown in Fig. 5 was computed from the geometry as explained in Sec. 9. On the side of the harmonic intensity pattern that decays more gradually, which we denote as the bright side, there is a slight suggestion of a ripple at about the position of the ρ line.

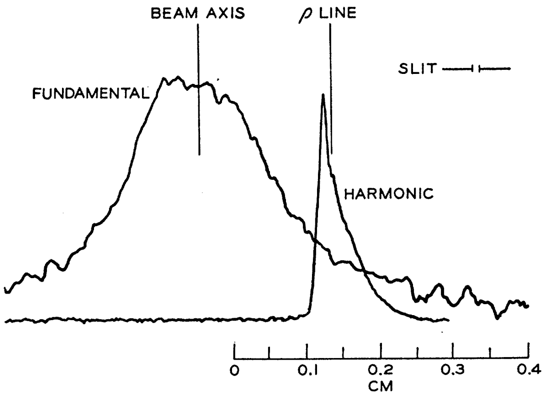

FIG. 5. Fundamental and harmonic intensity distributions measured with a traveling slit at the exit surface of the crystal. The beam axis was determined by estimating the center of the nearly Gaussian fundamental. The ρ line through the focus was determined from the geometry shown in Fig. 2 using the value $\rho=0.03$ appropriate (Ref. 2) for ADP. The intensity scale is linear here and throughout this paper. Constants for this experiment are given in Table I.

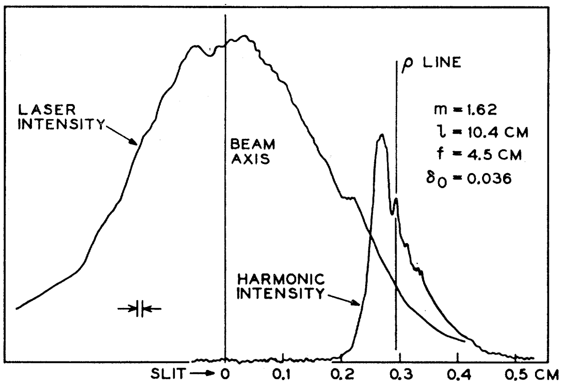

FIG. 6. Fundamental and harmonic intensity distributions of Fig. 5 measured with an imaging lens giving a magnification $m=1.62$. The ρ line, computed as explained in Fig. 5, just happens to fall on the second edge fringe in this experiment.

After having assured ourselves of the position of the ρ line directly, the harmonic and fundamental intensity distributions were studied with somewhat more resolution using the imaging lens with $a_3=6.8$ and $a_4=11.0$. The results of these scans are shown in Fig. 6. The magnification of the harmonic pattern in the visible was determined to be $m=11/6.8=1.62$ from the fact that the output face of the crystal was imaged in the plane of observation with ordinary room light. The position of the ρ line relative to the beam axis was computed from m. Since the magnification of the fundamental beam is likely to differ from the magnification in the visible, we took the precaution of passing the axis of the fundamental beam through the axis of the lens. This eliminates the need to know the infrared magnification at least as far as the beam axis location is concerned. We see that the position of the ρ line agrees with the result of Fig. 5. With the improved resolution we see the presence of bright side structure in the harmonic intensity with more certainty.

In order to study the bright-side structure and the shape of the harmonic intensity still more carefully, data were taken with $a_3=2.8$ and $a_4=13.0$ which gives a magnification $m=4.65$. This permits still higher resolution with results as shown by the solid curve of Fig. 7. The fringes are more pronounced and more numerous, decreasing in size and spacing down to the resolution of the slit width. This intensity data will be the basis of our comparison of the over-all shape of the distribution with theoretical calculations for the case which we shall call the well developed edge. For comparison with theory this and some of the subsequent figures contain theoretical scales, curves, and lines which will be fully explained in Sec. 9.

Since the bright-side fringes are a rather striking feature of the far-field harmonic distribution, further efforts were made to determine their spacing photographically. Figure 8 shows the results of placing photographic film at the plane of observation with $a_3=2.8$

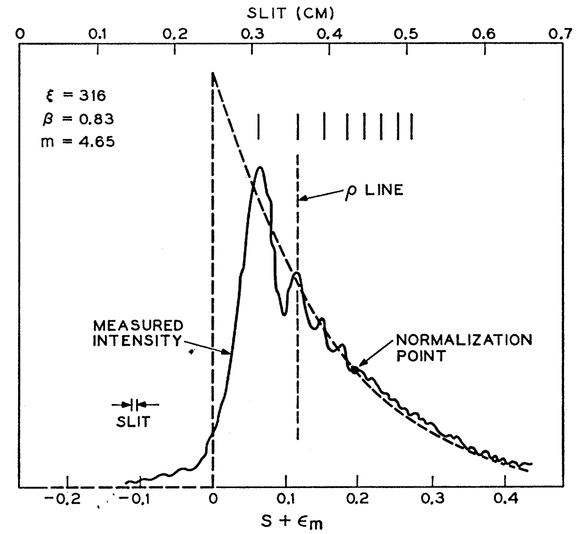

FIG. 7. Harmonic intensity (solid curve) at the exit surface as in Fig. 6 but measured with an optical magnification $m=4.65$. The slit position (arbitrary origin) is indicated by the scale at the top. The scale at the bottom, which is needed for comparison with theory, is laid out according to (9.8), (9.9), and (9.22). The calculated positions of eight edge fringes according to (9.7) are shown by lines. The dashed curve shows the dominant term (9.23) normalized to the data at one point as indicated. This is an example of well-developed edge structure, and may be compared with the calculated intensity of Fig. 20.

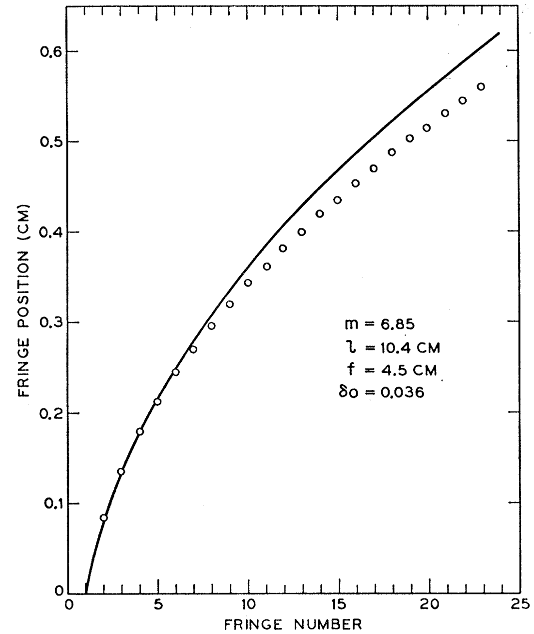

FIG. 9. Fringe positions measured on the photographs of Fig. 8 are shown by circles. Curve is calculated from (9.26) with no adjustable parameters.

and $a_4=18.0$ which gives $m=6.85$. In comparing the shapes observed here with previous photographs or with theory, it must be recalled that these pictures are expanded by a factor of $n=1.5$ in the y direction relative to the x direction (prism effect). By studying the pictures taken with various exposures the positions of as many as 23 fringes could be measured. More fringes with decreasing intensity and spacing were seen but their positions could not be accurately recorded.

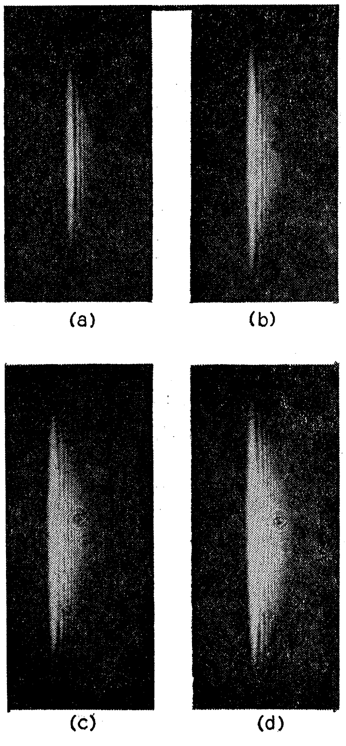
(a) (b)
(c) (d)

FIG. 8. Photographs of the harmonic beam scanned in Fig. 5 taken at the exit surface with an optical magnification $m=6.85$. The over-all magnification of the reproduction shown here is ~14×. Four exposures are shown to reveal the edge structure; longer exposures than (d) give a half-moon appearance like Fig. 4. This is well-developed edge structure.

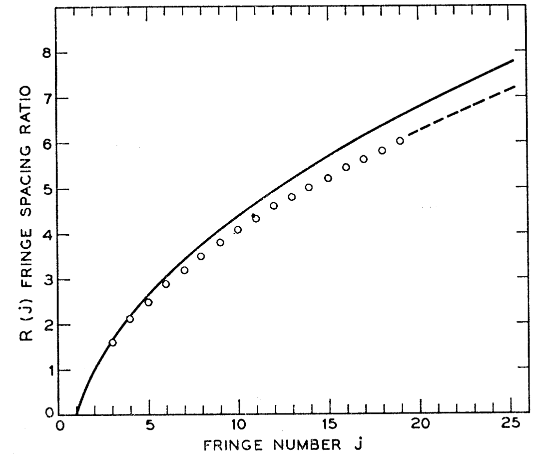

FIG. 10. Fringe spacing ratio (circles) defined in (9.25) for the data of Fig. 9. This ratio is independent of the magnification. Solid curve is the universal function (6.41) characteristic of well-developed edge structure. The same structure would be produced by a straight edge screen placed at the focus and illuminated with second-harmonic light. Dashed curve is the more accurate formula (6.42) which depends upon the specific parameters of the experiment. The dashed curve passes through the circles, but only its extension is shown to avoid confusing the figure.

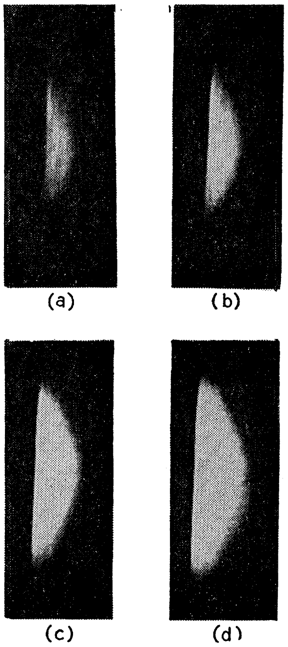

FIG. 11. Photographs of the harmonic taken by direct exposure without a lens at a distance $a_5=18$ cm from the crystal (KDP). The over-all magnification of the reproductions is $\sim 5\times$. Four exposures reveal the bright-side structure. This is partially developed edge structure.

The results of the fringe position measurements are shown by the circles in Fig. 9.

To remove any uncertainties regarding the magnification, it is convenient to measure the fringe spacing ratio $R(j)$. $R(j)$ gives the relative fringe spacings in normalized fashion and is defined as the ratio of the spacing between the jth maximum and the first maximum to the spacing between the second maximum and the first maximum. This is plotted (circles) in Fig. 10.

We now describe results obtained by removing the imaging lens and observing the harmonic after traversing an air space a_5. We call this case the partially developed edge. Figure 11 shows various exposures of the harmonic pattern taken with no prism in the laser. In many ways this is the easiest situation to observe experimentally. The patterns still show a pronounced edge and bright-side fringes, but the fringes are more diffuse and uniformly spaced. Although no prism was used, the tube current was reduced to keep the intensity of the extraneous lines low.

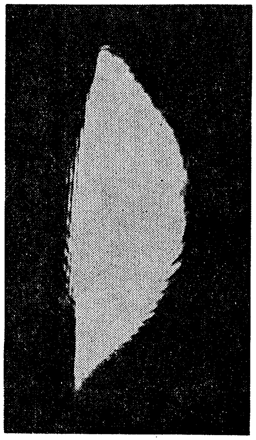

FIG. 12. Photograph as in Fig. 11(d) but with an effective exposure (taking into account film speed) about 1000 times longer. This reveals a series of uniformly spaced fringes on the dim side of the edge. In this photograph, chosen from many taken at different exposures, the first few dim-side fringes are overexposed.

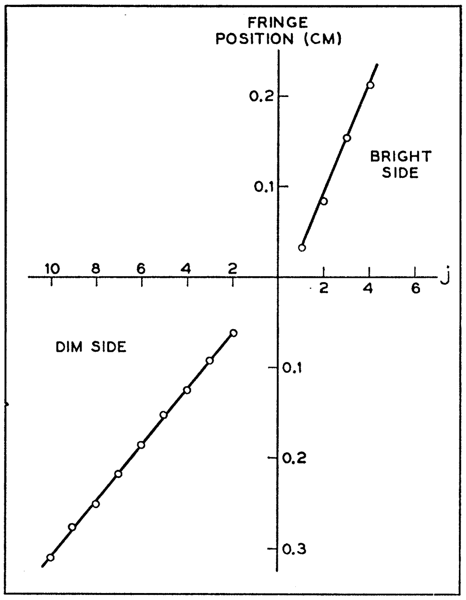

FIG. 13. Fringe positions measured on the photographs of Figs. 11 and 12 are shown by circles. The lines are calculated according to (9.31) and (9.32). The first dim-side fringe could not be resolved so it is not plotted. The second dim-side fringe and first bright-side fringe have been arbitrarily placed on the theoretical lines.

Since the theory predicts the presence of dim side fringes of much reduced intensity, long exposures with more sensitive film (Polaroid 10 000) were made. One of these is shown in Fig. 12 with an equivalent exposure time (accounting for film speed) roughly a thousand

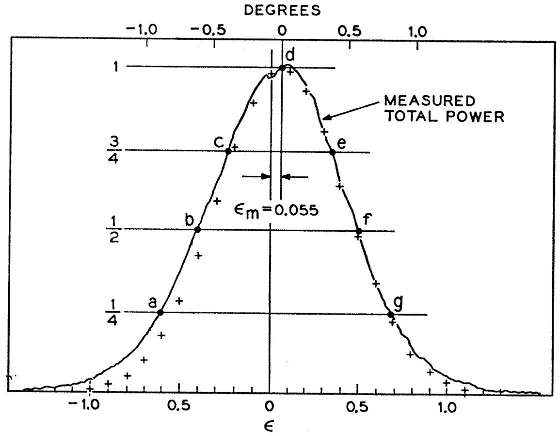

FIG. 14. Harmonic power (solid curve) recorded with no slit while the crystal (ADP) was rotated at a uniform rate on its motor driven stage. Crystal angle in degrees relative to the optimum orientation is given by scale at the top. The scale at the bottom, needed for comparison with theory, is laid out according to (9.19). Crosses are calculated values of $F(\epsilon)/F_m$ for $\beta=1.95$ according to (8.15).

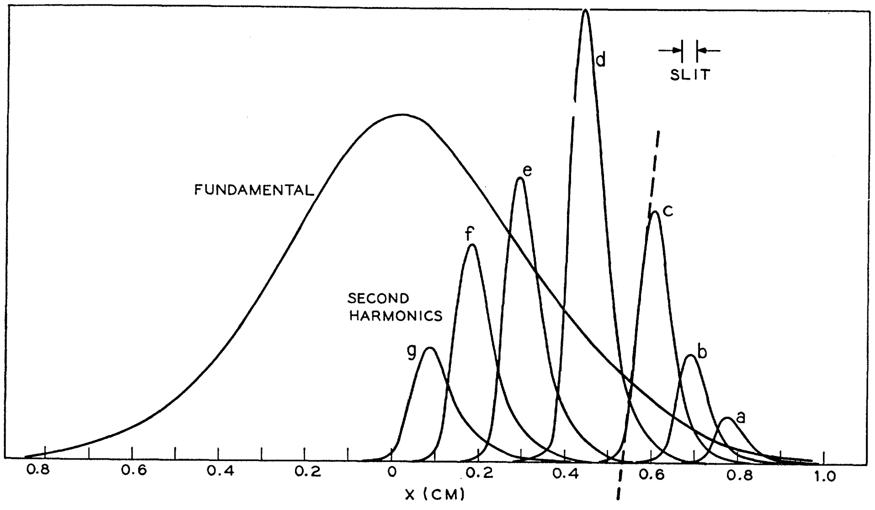

FIG. 15. Fundamental and harmonic intensity distributions for the crystal orientations $a, \cdots, g$ indicated in Fig. 14. The different harmonic curves are plotted to the same intensity scale. The dashed line shows how the position of the edge was defined by extrapolation to the base line.

times longer than Fig. 11(d). A series of uniformly spaced straight fringes is seen on the dim side of the pattern beyond the edge. On the bright side and overlapping on the dim-side fringes we see evidence of some swirling fringes. These have been traced to the presence of the focusing lens by watching the displacement of the swirling fringes as the focusing lens is moved relative to the fundamental beam.

The fringe positions from Figs. 11 and 12 are plotted (circles) in Fig. 13.

In the above measurements the nonlinear crystal was always adjusted for maximum harmonic power, which we call the optimum phase-matching condition. In the following we describe what happens to the harmonic power and the spatial distribution of the harmonic intensity as the crystal angle is varied about the optimum phase matching direction. In Fig. 14 we see a recorder tracing (solid curve) of the harmonic power as the crystal is rotated by the motor-driven stage. The optimum phase-matching angle is designated as 0 degrees. At each of the 7 points $(a,\cdots,g)$ indicated by solid dots on Fig. 14 the harmonic intensity distribution was measured. The crosses are theoretical points which will be explained in Sec. 9. The intensity distributions are shown in Fig. 15. Pronounced displacements of the harmonic relative to the fundamental are apparent. In Fig. 16 we plot the displacement of the harmonic edge from the beam axis as a function of the orientation of the crystal in degrees. The edge was estimated by extrapolating the steep portion of the edge back to the base line as shown in Fig. 15. The fundamental intensity distribution observed in this experiment was nearly Gaussian but slightly asymmetric. No prism was used in the laser.

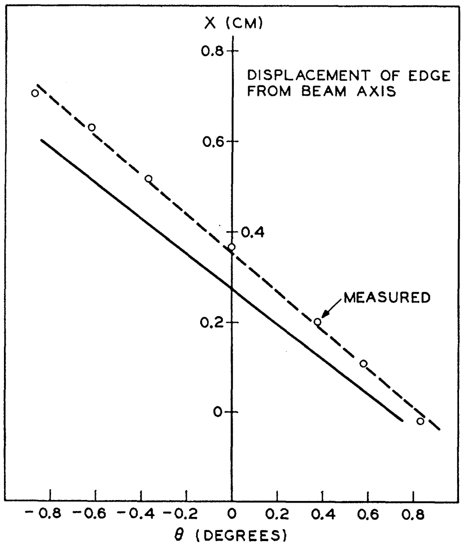

FIG. 16. Displacement (circles) of the edge from the beam axis as a function of crystal angle for the data of Fig. 15. Dashed line is a best linear fit to the data. Solid line is calculated from (9.20) with no adjustable parameters.

The data presented in this section will be reviewed again in Sec. 9 where the detailed comparison of theory and experiment will be made. The reader primarily interested in a survey of the various effects observed may now proceed immediately to Sec. 9.

3. GENERAL THEORY

3.1 Fourier Representation

The underlying ideas of the general theory will not be discussed here, since they have been developed in detail in BADK and in Ref. 3. As in BADK we shall consider the arrangement shown in Fig. 17. A laser beam is incident normally on the plane surface of a negative uniaxial crystal. We shall at first assume the crystal is arbitrarily long; later we shall consider the second-harmonic beam in the region beyond the exit surface of a finite crystal. Inside the crystal the laser beam is very nearly a plane wave (ordinary wave) $\exp(i\mathbf{k}_1\cdot\mathbf{r})$ with $\mathbf{k}_1$, the *nominal* wave vector of the beam, along the surface normal vector $\mathbf{N}$. We choose Cartesian coordinates such that z is measured along $\mathbf{N}$, the surface is the plane $z=0$, and the optic axis lies in the xz plane. The laser beam sets up a polarization wave which is very nearly a plane wave $\exp(2i\mathbf{k}_1\cdot\mathbf{r})$ at the second-harmonic frequency ω. More generally the polarization can be expanded in terms of its Fourier components in the form

$$\mathbf{P}(\mathbf{r})=e^{-\alpha_1 z}\int \mathbf{P}_K e^{i\mathbf{K}\cdot\mathbf{r}}d\mathbf{K}, \tag{3.1}$$

and we assume that $\mathbf{P}_K$ is nonvanishing only for $\mathbf{K}$ within a small neighborhood of $2\mathbf{k}_1$, the nominal wave vector of the polarization beam.

In addition to the waves $\exp(i\mathbf{K}\cdot\mathbf{r})$, we have to consider the free waves (light waves) in the crystal which have the form (extraordinary waves)

$$\mathbf{U}e^{i(\omega/c)n_2\mathbf{s}\cdot\mathbf{r}}, \tag{3.2}$$

with $\mathbf{U}$ a unit vector giving the allowed polarization of the wave, $\mathbf{s}$ a unit vector giving its phase propagation direction, and n_2 the refractive index for the extraordinary wave. It is convenient to define the vectors

$$\boldsymbol{\eta}=(c/\omega)\mathbf{K},\quad \boldsymbol{\eta}_1=(c/\omega)2\mathbf{k}_1,\quad \boldsymbol{\eta}_2=n_2\mathbf{s}. \tag{3.3}$$

The vectors $\boldsymbol{\eta}_2$ are constrained to lie on the index surface of the crystal. *Index matching* occurs when $\boldsymbol{\eta}=\boldsymbol{\eta}_2$. We shall first assume as in BADK that the nominal wave vector $2\mathbf{k}_1$ of the polarization beam is matched. Optimum matching for focused beams will be considered later in Sec. 8. In Fig. 17 we show the index surface for the extraordinary wave with $\boldsymbol{\eta}_1$ normal to the crystal surface and falling on the index surface. The *mismatch* of a general Fourier component of polarization is measured by φ' defined by the vector relation

$$\varphi'\mathbf{N}=\boldsymbol{\eta}-\boldsymbol{\eta}_2. \tag{3.4}$$

The *double refraction angle* ρ is the angle between $\boldsymbol{\eta}_1$ and the normal to the index surface. When absorption is present mismatch is measured by a complex mismatch function φ defined by

$$\varphi\mathbf{N}=\boldsymbol{\eta}-\boldsymbol{\eta}_2+i(c/\omega)\alpha\mathbf{N}, \tag{3.5}$$

where α is an effective absorption coefficient

$$\alpha=\alpha_1-\tfrac{1}{2}\alpha_2, \tag{3.6}$$

with α_1 and α_2 the absorption coefficients for the laser and second harmonic, respectively. The solution of (3.5) is

$$\varphi=\varphi'+i\varphi'', \tag{3.7}$$

where φ' is defined by (3.4) and

$$\varphi''=(c/\omega)\alpha. \tag{3.8}$$

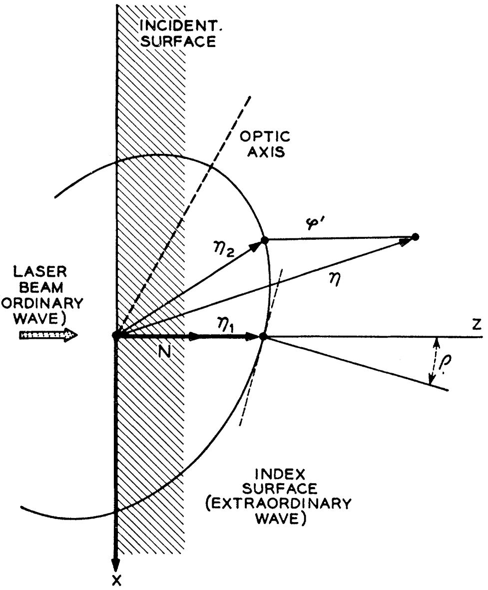

FIG. 17. Index surface and the vector mismatch relation (3.4) for the nominal matching case with the laser beam normal to the incident surface of the crystal.

It was shown in BADK that the second harmonic electric field $\mathbf{E}_2(\mathbf{r})$ is given by [see (5.38) of BADK]

$$\mathbf{E}_2(\mathbf{r})=ze^{-\alpha_1 z}\int \boldsymbol{\gamma}\cdot\mathbf{P}_K g(2i\psi_K)e^{i\mathbf{K}\cdot\mathbf{r}}d\mathbf{K}, \tag{3.9}$$

where

$$2\psi_K=(\omega/c)\varphi z=(\omega/c)\varphi' z+i\alpha z, \tag{3.10}$$

$$g(x)=(1-e^{-x})/x=\int_0^1 dp\, e^{-xp}, \tag{3.11}$$

and $\boldsymbol{\gamma}$ is the dyadic

$$\boldsymbol{\gamma}=2\pi i(\omega/cn)\mathbf{U}\mathbf{U}. \tag{3.12}$$

Here n is the matched index $n=n_1=(c/\omega)2k_1=n_2(\mathbf{N})$. To the second order in the components of $\mathbf{K}-2\mathbf{k}_1$ in the *nominal matching case*

$$2\psi_K=(K_z-2k_1+\rho K_x)z+\frac{K_x^2+K_y^2}{4k_1}z+i\alpha z. \tag{3.13}$$

For computational purposes it is often convenient to write (3.9) in the form

$$\mathbf{E}_2(\mathbf{r})=ze^{-\alpha_1 z}\int_0^1 dp\int \boldsymbol{\gamma}\cdot\mathbf{P}_K e^{-2ip\psi_K}e^{i\mathbf{K}\cdot\mathbf{r}}d\mathbf{K}. \tag{3.14}$$

In (3.9) and (3.14) it is assumed that $\mathbf{r}$ lies *inside the crystal.*

The Fourier components $\mathbf{P}_K$ of the polarization are obtained by inverting (3.1)

$$\mathbf{P}_K=(2\pi)^{-3}\int \mathbf{P}(\mathbf{r})_{\text{NA}}e^{-i\mathbf{K}\cdot\mathbf{r}}d\mathbf{r}, \tag{3.15}$$

where $\mathbf{P}(\mathbf{r})_{\mathrm{NA}}$ is the polarization with no absorption. We may obtain $\mathbf{P}_K$ in two equivalent ways. If the laser is operated in a definite mode the laser field with no absorption $\mathbf{E}_1(\mathbf{r})_{\mathrm{NA}}$ can be described by convenient analytical expressions given by Boyd and Gordon.[7] We then have

$$\mathbf{P}(\mathbf{r})_{\mathrm{NA}}=\mathbf{d}\cdot\mathbf{E}_1(\mathbf{r})_{\mathrm{NA}}\mathbf{E}_1(\mathbf{r})_{\mathrm{NA}}\,, \tag{3.16}$$

where $\mathbf{d}$ is the second order polarization tensor, and $\mathbf{P}_K$ is obtained from (3.15). Note that $\mathbf{d}$ relates the (time-independent) Fourier amplitudes and not the instantaneous values of the polarization and electric field. On the other hand, the laser beam might be specified by its Fourier components $\mathbf{E}_k$

$$\mathbf{E}_1(\mathbf{r})=e^{-\frac{1}{2}\alpha_1 z}\int\mathbf{E}_k e^{i\mathbf{k}\cdot\mathbf{r}}d\mathbf{k}\,. \tag{3.17}$$

It is then most convenient to obtain $\mathbf{P}_K$ from

$$\mathbf{P}_K=\int(\mathbf{d}\cdot\mathbf{E}_k\mathbf{E}_{K-k})d\mathbf{k}\,, \tag{3.18}$$

which explicitly exhibits the *mixing* property of the second-order polarization. Whether $\mathbf{P}_K$ is calculated by (3.15) or (3.18) it includes these mixing effects.

Having shown how ψ_K and $\mathbf{P}_K$ are determined as functions of $\mathbf{K}$, it only remains to carry out the integration over $\mathbf{K}$ in (3.9) or (3.14) to obtain the second harmonic field $\mathbf{E}_2(\mathbf{r})$. Although we deal explicitly with the case of a negative uniaxial crystal and a beam at normal incidence, it would not be difficult to generalize the treatment to an arbitrary biaxial crystal and an arbitrary beam direction. The necessary refinements could all be included in a more general expression for ψ_K than we have given in (3.13). For a more general discussion of the linear part of the mismatch function the reader may consult Ref. 3. From the physical point of view, our most important assumption is that all the Fourier components of $\mathbf{P}(\mathbf{r})$ are close to index matching conditions. This assumption enables us to use the simple formula (3.9) based on the *nearly matching approximation* of Ref. 3, to retain only one of the index surfaces of the medium, and to terminate the expansion of ψ_K at terms second order in $\mathbf{K}-2\mathbf{k}_1$. The theory may break down for very strongly focused beams having a diffraction angle $\delta_0>0.1$ rad.

3.2 Interior Green's Function

One aim of the general theory should be to relate the second harmonic field $\mathbf{E}_2(\mathbf{r})$ to its source $\mathbf{P}(\mathbf{r})$ as simply and directly as possible. This will be done by means of a *Green's function* formulation of the theory. A theory of this type has previously been described[3] for isotropic media in which $\mathbf{E}_2(\mathbf{r})$ is obtained in the form

$$\mathbf{E}_2(\mathbf{r})=(\omega^2/c^2)\int(\mathbf{I}-\mathbf{ss})\cdot\mathbf{P}(\mathbf{r}')\Phi(|\mathbf{r}-\mathbf{r}'|)d\mathbf{r}'\,, \tag{3.19}$$

where $\mathbf{s}$ is a unit vector in the direction of $\mathbf{r}-\mathbf{r}$ and

$$\Phi(|\mathbf{r}-\mathbf{r}'|)=|\mathbf{r}-\mathbf{r}'|^{-1}e^{i(\omega/c)n|r-r'|} \tag{3.20}$$

is the Green's function. The dyadic $(\mathbf{I}-\mathbf{ss})$ is a projection operator which selects the transverse part of $\mathbf{P}(\mathbf{r})$. Since the medium is assumed isotropic n is a constant and the two transverse components are equivalent. A small amount of anisotropy can be introduced into this theory in a natural way by treating the two transverse components separately (e.g., the ordinary and extraordinary waves in a uniaxial crystal) with an appropriate Green's function for each in which n depends on the direction $\mathbf{s}$. Such a theory would apply to SHG by focused beams under *nonmatching conditions*, where $\boldsymbol{\eta}_1$ of (3.3) and Fig. 17 does not fall on an index surface, and the Fourier components of $\mathbf{P}(\mathbf{r})$ have (normalized) wave vectors $\boldsymbol{\eta}$ falling about as close to one index surface as to the other. In this section we are concerned with SHG under *nominal matching conditions*, by which we mean that $\boldsymbol{\eta}_1$ falls on an index surface, and the Fourier components $\boldsymbol{\eta}$ all fall close to this (extraordinary) index surface and relatively far from the other (ordinary) index surface. It is then permissible to neglect the unmatched waves, so that only a single component of $\mathbf{P}(\mathbf{r})$ appears in our result.

If in (3.9) we substitute (3.15) and interchange the order of integration we obtain

$$\mathbf{E}_2(\mathbf{r})=\int\boldsymbol{\gamma}\cdot\mathbf{P}(\mathbf{r}')G(\mathbf{r},\mathbf{r}')d\mathbf{r}'\,, \tag{3.21}$$

where

$$G(\mathbf{r},\mathbf{r}')=ze^{\alpha_1(z'-z)}(2\pi)^{-3}\int g(2i\psi_K)e^{i\mathbf{K}\cdot(\mathbf{r}-\mathbf{r}')}d\mathbf{K} \tag{3.22}$$

is the *Green's function* for SHG under nominal matching conditions in an anisotropic medium. For a negative uniaxial crystal and normal incidence of the beam ψ_K is given by (3.13), and (3.22) can be written

$$G(\mathbf{r},\mathbf{r}')=ze^{\alpha_1(z'-z)}(2\pi)^{-3}\int_0^1 dp\; e^{p\alpha z}$$
$$\times\int d\mathbf{K}\; e^{-ipz(K_z-2k_1+\rho K_x)}$$
$$\times e^{-ipz(K_x{}^2+K_y{}^2)/4k_1}e^{i\mathbf{K}\cdot(\mathbf{r}-\mathbf{r}')}\,. \tag{3.23}$$

The integration over K_z gives the factor

$$2\pi\delta(z-z'-pz)\,, \tag{3.24}$$

which shows that $G(\mathbf{r},\mathbf{r}')$ vanishes unless z' lies in the region

$$0\leq z'\leq z\,. \tag{3.25}$$

We may regard (3.21) as an integration over *source points* $\mathbf{r}'$ to give the field at an *observer point* $\mathbf{r}$. Thus (3.25) says that the field at x, y, z is entirely due to sources lying between z and the crystal surface $z=0$. The condition $z'\geq 0$ is a consequence of using an approximation in which $E_2(x,y,0)=0$, which implies that $z=0$ is the incident surface. The condition $z'\leq z$ is a causal relation which couples the observer point only with source points which are "upstream." In this sense we may always regard the z surface as the exit surface of the crystal as far as SHG is concerned.

Carrying out the integration over p in (3.23) gives

$$G(\mathbf{r},\mathbf{r}')=e^{-\frac{1}{2}\alpha_2(z-z')}e^{2ik_1(z-z')}(2\pi)^{-2}$$
$$\times\int\int dK_x dK_y e^{iK_x(x-x')+iK_y(y-y')-i\rho K_x(z-z')}$$
$$\times e^{-i[(K_x{}^2+K_y{}^2)/4k_1](z-z')}. \quad (3.26)$$

This integral can be evaluated with the aid of the formula

$$\int_{-\infty}^{\infty} e^{-iax-ibx^2}dx=\left(\frac{\pi}{ib}\right)^{1/2} e^{ia^2/4b} \quad \mathrm{Im}(b)<0. \quad (3.27)$$

The result can be written

$$G(\mathbf{r},\mathbf{r}')=\left(\frac{\omega n}{2\pi ic}\right)\frac{1}{Z}e^{-\frac{1}{2}\alpha_2 Z}e^{2ik_1 Z+ik_1(X^2+Y^2)/Z}, \quad (3.28)^*$$

where

$$X=(x-\rho z)-(x'-\rho z'),$$
$$Y=y-y', \quad (3.29)$$
$$Z=z-z'\geq 0.$$

If we assume that the important region is

$$X^2+Y^2\ll Z^2 \quad (3.30)$$

in the spirit of the paraxial approximation we can write

$$Z^{-1}\simeq R^{-1}$$
$$2Z+(X^2+Y^2)/Z\simeq 2R, \quad (3.31)$$

where

$$R=(X^2+Y^2+Z^2)^{1/2}. \quad (3.32)$$

Then (3.28) becomes

$$G(\mathbf{r},\mathbf{r}')\simeq\left(\frac{\omega n}{2\pi ic}\right)e^{-\frac{1}{2}\alpha_2 Z}\Phi(R), \quad (3.33)$$

where $\Phi(R)$ is the Green's function (3.20) with $|\mathbf{r}-\mathbf{r}'|$ replaced by R. The validity of (3.30) depends upon $\mathbf{P}(\mathbf{r}')$ being nearly a plane wave in the vicinity of each point $\mathbf{r}'$, which is consistent with our previous assumption that the Fourier components of $\mathbf{P}(\mathbf{r})$ are confined to a small neighborhood of $\mathbf{K}$ space.

From (3.12) and (3.33) we have

$$\gamma G(\mathbf{r},\mathbf{r}')\simeq(\omega^2/c^2)e^{-\frac{1}{2}\alpha_2 Z}\Phi(R)\mathbf{UU}, \quad (3.34)$$

which is very similar to the quantity $(\omega^2/c^2)(\mathbf{I}-\mathbf{ss})\times\Phi(|r-r'|)$ in (3.19). The dyadic $\mathbf{UU}$ selects only one of the transverse components of $\mathbf{P}(\mathbf{r}')$ corresponding to our assumption that one of the transverse components is matched and the other can be neglected. As we would expect $G(\mathbf{r}-\mathbf{r}')$ depends on the absorption α_2 of the second harmonic but not on the absorption α_1 of the fundamental. The anisotropy of the medium enters R through ρ in the definition of X. Replacing $|\mathbf{r}-\mathbf{r}'|$ in the Green's function by R is equivalent to replacing the constant refractive index n in (3.20) by the correct direction dependent $n(\mathbf{s})$ for the medium with $\mathbf{s}$ in the direction of $\mathbf{r}-\mathbf{r}'$. Thus our detailed derivation shows that the straightforward generalization of (3.19) and (3.20) to absorbing anisotropic media does in fact give the correct result.

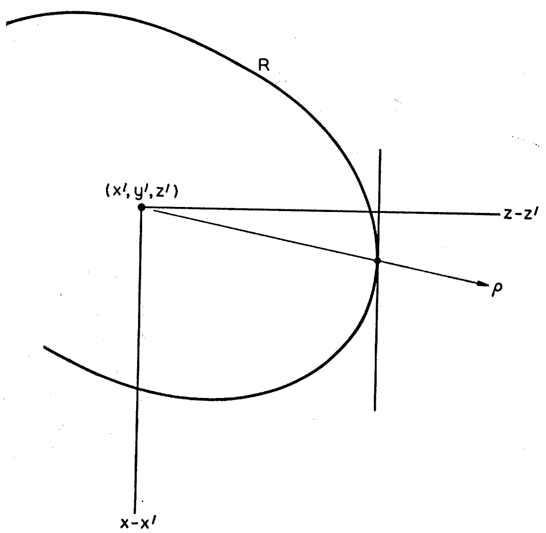

FIG. 18. Outgoing wavelet (3.35) is shown by curve labeled R, vertical tangent represents resultant wavefront from all sources on the plane z', and point of tangency locates the energy radiated from (x',y',z').

The physical interpretation of the Green's function may be explained in the same way as in isotropic media. Consider that the polarization at the point x', y', z' in Fig. 18 is the source of an outgoing wavelet

$$\frac{1}{R}e^{i(\omega/c)nR}, \quad (3.35)$$

where n is the matched refractive index defined by $2k_1=(\omega/c)n$. The surfaces of constant phase of the wavelet are specified by

$$R=\text{const}. \quad (3.36)$$

One of these is represented by the curve labeled R in Fig. 18. Thus the role played by the distance $|\mathbf{r}-\mathbf{r}'|$ in isotropic media is now taken over by R. Suppose $\mathbf{P}(x,y,z)$ is nearly a plane wave in the z direction, and consider the resultant radiation from all sources on the

z' plane. Evidently the wavelets will produce nearly a plane wave whose approximate planes of constant phase at any instant are envelopes of the wavelets and therefore tangent to the wavelets. The vertical tangent indicated in Fig. 18 represents the second harmonic wavefront. The points of tangency satisfy

$$x-x'=\rho(z-z'), \tag{3.37}$$

which is the equation of the ρ line through x', y', z'. All parts of the wavelet which are not very close to the point of tangency destructively interfere and produce no resultant field. Thus all the energy radiated at the source point x', y', z' flows along the ρ line. This explains why energy is transported at the angle ρ to the direction of phase propagation and compliments the completely formal proof given in the Appendix of BADK.

3.3 Exterior Green's Function

Up to this point we have regarded all points $z>0$ as lying in the nonlinear medium. In practice the crystal will have a *finite length* which we shall denote by l. Thus (3.9) and (3.21) apply to the region within the slab

$$0\leq z\leq l, \tag{3.38}$$

and in particular to the exit surface $z=l$ where $\mathbf{E}_2$ is accessible to measurement. Outside of the crystal $\mathbf{P}(\mathbf{r})$ vanishes identically, so that the region of integration in (3.21) is confined to the slab. At the exit surface the reflection and transmission coefficients for the second harmonic will be essentially the same as for an unbounded plane wave. If the medium beyond the exit surface is air (considered equivalent to vacuum) the field in the air at the exit surface is given by

$$\lim_{z\to l+} E_2(x,y,z)=\frac{2n}{n+1}\lim_{z\to l-} E_2(x,y,z), \tag{3.39}$$

where $l+$ signifies that $z\to l$ on the air side, $l-$ signifies $z\to l$ on the crystal side. The right side of (3.39) may be obtained from (3.9) or (3.21) with $z=l$; our problem is then to determine the field at an arbitrary point in the air beyond the exit surface. We shall neglect the second harmonic reflected at the surface and the polarization produced by the reflected laser beam.

From the field in air at the surface we can obtain the field at an arbitrary point by means of diffraction theory[13]

$$\mathbf{E}_2(x,y,z)=-\frac{\omega i}{2\pi c}\int\int \mathbf{E}_2(x'',y'',l)\frac{e^{i(\omega/c)\beta}}{\beta}dx''dy'', \tag{3.40}$$

where $E_2(x'',y'',l)$ is the field in air at the surface and β is here an abbreviation for the function

$$\beta=[(x-x'')^2+(y-y'')^2+(z-l)^2]^{1/2}. \tag{3.41}$$

We can write (3.40) in the form

$$\mathbf{E}_2(\mathbf{r})=\int \boldsymbol{\gamma}\cdot\mathbf{P}(\mathbf{r}')G_e(\mathbf{r},\mathbf{r}')d\mathbf{r}', \tag{3.42}$$

where $G_e(\mathbf{r},\mathbf{r}')$ is the *external Green's function* which replaces $G(\mathbf{r},\mathbf{r}')$ when $\mathbf{r}$ lies outside the crystal. From (3.21), (3.39), and (3.40)

$$G_e(\mathbf{r},\mathbf{r}')=\frac{2n}{n+1}\frac{\omega}{2\pi ic}\frac{1}{z-l}\times\int\int G(\mathbf{r}'',\mathbf{r}')e^{i(\omega/c)\beta}dx''dy'', \tag{3.43}$$

where we have taken β^{-1} outside the integral and set it equal to $(z-l)^{-1}$. In the exponent we write

$$2\beta\simeq 2(z-l)+\frac{(x-x'')^2}{z-l}+\frac{(y-y'')^2}{z-l}, \tag{3.44}$$

which is equivalent to (3.31). With the aid of formula (3.27) the integrations of (3.43) can be carried out to obtain

$$G_e(\mathbf{r},\mathbf{r}')=\frac{2n}{n+1}\left(\frac{\omega n}{2\pi ic}\right)\times\frac{1}{l-z'+n(z-l)}e^{-\frac{1}{2}\alpha_2(l-z')}e^{i(\omega/c)[n(l-z')+z-l]}\times\exp\left\{i\frac{\omega n}{2c}\frac{[(x-x'-\rho(l-z'))^2+(y-y')^2]}{l-z'+n(z-l)}\right\}. \tag*{(3.45)*}$$

The field in air $E_2(x,y,z)$ given by (3.40), or the intensity proportional to $|E_2|^2$, is in principle accessible to experimental measurement. In practice it is usually convenient to employ an optical system, which we shall call simply a *lens*, to form an image of the desired field distribution having a suitable size and location for measurement. Let us place a thin lens at distance L_1 from z in the plane $z+L_1$, and consider the field a distance L_2 from the lens in the plane $z+L_1+L_2$, where L_1 and L_2 satisfy the object-image equation of geometrical optics

$$1/L_1+1/L_2=1/L, \tag{3.46}$$

with L the focal length of the lens. By application of (3.40) we could obtain the field at $z+L_1$ in terms of the field $E_2(x,y,z)$. The effect of the lens is to introduce a phase factor $\exp[i(\omega/2cL)(x^2+y^2)]$, and we could then apply (3.40) again to obtain the field at $z+L_1+L_2$. This calculation has been carried out by Kogelnik,[14] who has shown that if L_1, L_2 satisfy (3.46)

$$E_{\text{lens}}(x,y,z+L_1+L_2)=m^{-1}E_2(m^{-1}x,m^{-1}y,z)\times e^{i(\omega/c)(L_1+L_2)}e^{i(\omega/2cLm)(x^2+y^2)}, \tag{3.47}$$

---

[13] M. Born and E. Wolf, *Principles of Optics* (Pergamon Press, London, 1959), Sec. 8.3.

[14] H. Kogelnik, Bell System Tech. J. **44**, 455 (1965).

where the *magnification* m is defined by

$$m=-L_2/L_1. \tag{3.48}$$

For a more general optical system (3.47) is still valid if L_1, L_2 are measured from the principal planes. We have written $E_{\mathrm{lens}}(x,y,z+L_1+L_2)$ in (3.47) to avoid confusing this field with $E_2(x,y,z+L_1+L_2)$, which would have been the field in the $z+L_1+L_2$ plane without a lens. It is inadvisable to attempt to apply (3.47) to a case where the object plane lies inside the crystal.

4. GAUSSIAN BEAMS

4.1 Fundamental Field

A Gaussian beam is an approximate solution of Maxwell's equations which is sharply concentrated along some axis of propagation and has a Gaussian distribution of field strength in the direction perpendicular to the axis at all points along the axis. As shown by Boyd and Gordon[7] the lowest or fundamental mode of a confocal resonator consists of Gaussian beams properly related in phase and propagating in opposite directions along the mirror axis. For the nonconfocal resonator, or the resonator employing one spherical and one plane mirror, it can be shown[7] that there always exists a hypothetical confocal resonator having the same modes. The spacing of the mirrors in this hypothetical equivalent confocal resonator is called the *confocal parameter b*. We shall assume the axis of the beam is the z axis and the position of the focus is $z=f$. At the focus the beam has its smallest spread measured by the parameter w_0 called the *minimum spot size.* According to theory

$$b=w_0^2k_1, \tag{4.1}$$

where $\mathbf{k}_1$ is the wave vector of the beam. Near the axis the beam behaves much like the plane wave $\exp(i\mathbf{k}_1\cdot\mathbf{r})$ as assumed in the previous section.

It is convenient to measure distances from the focus by the dimensionless coordinate

$$\xi=2(z-f)/b. \tag{4.2}$$

Here f may have either sign. We shall also write $\xi=(2/b)(l-f)$ later on, since $z=l$ is the surface of experimental interest. The electric field $E_1(x,y,z)$ of a Gaussian beam can be written

$$\mathbf{E}_1(x,y,z)=\mathbf{E}_0\frac{1}{1+i\xi}e^{ik_1z}\exp\left[-\frac{x^2+y^2}{w_0^2(1+i\xi)}\right]. \tag{4.3}$$

The nominal wave vector of the beam is $\mathbf{k}_1=k_1\mathbf{N}$. In the near field $\xi\ll1$, however, where the beam is confined to a narrow waist, the effective wave vector describing the propagation of phase along the axis is $k_1-(2/b)$ because of the factor $(1+i\xi)^{-1}$. This shows why the familiar index matching condition,[10] which gives the maximum SHG for plane waves, is not the optimum matching condition for focused beams. This problem will be fully treated in Sec. 8, but meanwhile it is convenient to assume the nominal matching condition. The spot size may be defined as the radial distance from the axis w at which the amplitude of the field falls to $1/e$ of its axial value. From (4.3) we have

$$w=w_0(1+\xi^2)^{1/2}. \tag{4.4}$$

At large distances from the focus, called the *far field*,

$$\xi\gg1 \tag{4.5}$$

we have

$$w\rightarrow\xi w_0=(2w_0/b)(z-f). \tag{4.6}$$

The quantity

$$\delta_0=2w_0/b=2/w_0k_1 \tag{4.7}$$

giving half the total angular spread of the beam is called the *diffraction angle*. Gaussian beams only exist in the paraxial approximation

$$\delta_0\ll1. \tag{4.8}$$

This is equivalent to our assumption in the previous section that the laser beam is nearly a plane wave.

Figure 2 shows a Gaussian beam entering the crystal at $z=0$, coming to a focus at f and diverging with the diffraction angle δ_0. The field strength according to (4.3) is shown dashed on the right at some depth z as a function of transverse position. The dashed lines at angle ρ and the variable s, and the points u_1, 0, u_2, will be explained in the next section. The SHG curve represents the second harmonic field strength neglecting fine structure according to (5.28).

4.2 Interior Harmonic Field

We imagine that the crystal is a slab extending from the incident surface $z=0$ to the exit surface $z=l$. The laser electric field with no absorption is given by (4.3) in the slab $0\leq z\leq l$, and the polarization beam with no absorption is given by

$$\mathbf{P}(\mathbf{r})_{\mathrm{NA}}=\mathbf{P}_0\frac{1}{(1+i\xi)^2}e^{2ik_1z}\exp\left[-\frac{2(x^2+y^2)}{w_0^2(1+i\xi)}\right]B(z), \tag{4.9}$$

where

$$\begin{aligned}B(z)&=1 \quad 0\leq z\leq l\\&=0 \quad z<0,\ z>l.\end{aligned} \tag{4.10}$$

In the presence of absorption the polarization beam is

$$\mathbf{P}(\mathbf{r})=e^{-\alpha_1z}\mathbf{P}(\mathbf{r})_{\mathrm{NA}}. \tag{4.11}$$

We first consider the field $\mathbf{E}_2(\mathbf{r})$ within the slab $0\leq z\leq l$. We have the choice of using either the Fourier method (3.14) or the Green's-function method (3.21), both of which will be briefly outlined.

If we substitute (4.9) into the definition (3.15) of the Fourier components $\mathbf{P}_K$, we find that the integrations over x and y can be carried out with the aid of the formula (3.27), but we are left with an integral over z

which cannot be expressed in a convenient closed form. This is no great disadvantage, however, since the integral expression for $\mathbf{P}_K$ can be substituted into (3.14), and the integrations over $\mathbf{K}$ can be carried out in closed form. A closed-form expression for $\mathbf{P}_K$ can be obtained if we omit the slab function $B(z)$ from (4.9). This will still lead to the same $\mathbf{E}_2(\mathbf{r})$ for points z within the slab. The reason for this has already been brought out in (3.25); it is permissible to alter $\mathbf{P}(\mathbf{r}')$ in the regions $z'<0$ and $z'>z$ since $\mathbf{E}_2(\mathbf{r})$ depends only on $\mathbf{P}(\mathbf{r}')$ within $0\leq z'\leq z$. If we omit $B(z)$ in (4.9), we obtain

$$\begin{aligned}\mathbf{P}_K&=\mathbf{P}_0\frac{w_0^2b}{16\pi}e^{i(2k_1-K_z)f}e^{-bk_1+(b/2)K_z} && K_z<K_c\\ &=0, && K_z>K_c \qquad (4.12)\end{aligned}$$

where the cutoff wave vector is

$$K_c=2k_1-\frac{K_x^2+K_y^2}{4k_1}. \tag{4.13}$$

We have displayed this explicit expression for $\mathbf{P}_K$ in order to make the discussion of the Fourier method more concrete. It should be emphasized again that (4.12) describes a beam which for SHG is equivalent to but not identical to the more precise description (4.9). It is now somewhat tedious but elementary to evaluate (3.14) and obtain $(0\leq z\leq l)$

$$\begin{aligned}\mathbf{E}_2(x,y,z)&=z\boldsymbol{\gamma}\cdot\mathbf{P}_0e^{-\alpha_1z}\\ &\times e^{2ik_1z}\frac{1}{1+i\xi}\int_0^1dp\frac{e^{p\alpha z}}{1-i(2f/b)+i(2z/b)(1-p)}\\ &\times\exp\left\{-\frac{2[(x-p\rho z)^2+y^2]}{w_0^2(1+i\xi)}\right\}. \qquad (4.14)\end{aligned}$$

We cannot carry out the final integration over p except in certain limiting cases. For the *near field*

$$\xi\ll1, \tag{4.15}$$

we consider the limit $b\rightarrow\infty$ in (4.14) and obtain

$$z\boldsymbol{\gamma}\cdot\mathbf{P}_0e^{-\alpha_1z}e^{2ik_1z}\int_0^1dp\ e^{p\alpha z}e^{-2[(x-p\rho z)^2+y^2]/w_0^2}, \tag{4.16}$$

which agrees with Eq. (5.55) of BADK for a parallel beam. The case of the far field will be considered in the next section. The case $\rho=0$ will be treated in Sec. 8.

Now let us substitute (4.9), (4.11), and the Green's function (3.28) into (3.21).

$$\begin{aligned}\mathbf{E}_2(\mathbf{r})&=\boldsymbol{\gamma}\cdot\mathbf{P}_0\frac{\omega n}{2\pi ic}e^{-\frac{1}{2}\alpha_2z}e^{2ik_1z}\iiint\frac{e^{-\alpha z'}B(z')}{Z(1+i\xi')^2}\\ &\times\exp\left\{ik_1\frac{X^2+Y^2}{Z}-\frac{2(x'^2+y'^2)}{w_0^2(1+i\xi')}\right\}dx'dy'dz', \qquad (4.17)\end{aligned}$$

where $\xi'=2(z'-f)/b$. We can integrate over x' and y' using the expansions

$$\begin{aligned}X^2&=x'^2-2x'(x-\rho Z)+(x-\rho Z)^2,\\ Y^2&=y'^2-2y'y+y^2,\end{aligned} \tag{4.18}$$

and formula (3.27) to obtain the field *within the crystal*

$$\begin{aligned}\mathbf{E}_2(\mathbf{r})&=\boldsymbol{\gamma}\cdot\mathbf{P}_0e^{-\frac{1}{2}\alpha_2z}e^{2ik_1z}\frac{1}{1+i\xi}\int_0^z\frac{e^{-\alpha z'}}{1+i\xi'}\\ &\times\exp\left\{-\frac{2[(x-\rho Z)^2+y^2]}{w_0^2(1+i\xi)}\right\}dz'. \qquad (4.19)^*\end{aligned}$$

This becomes identical with (4.14) if z' is replaced by the variable $p=Z/z=1-(z'/z)$. Thus we have shown the equivalence of the Green's function and Fourier methods in the case of a Gaussian beam. They are, of course, formally equivalent in general, although in some cases one method may be more convenient than the other.

4.3 Exterior Harmonic Field

We have obtained an expression (4.14) or (4.19) for the field $\mathbf{E}_2(\mathbf{r})$ valid at any point within the crystal. In particular the field in air at the exit surface $z=l$ is obtained by multiplying (4.19) by the transmission coefficient $2n/(n+1)$ and setting $z=l$. This field may be observed experimentally with the aid of an optical system focused on the exit surface. It is also useful to have an expression for the field $\mathbf{E}_2(\mathbf{r})$ in air beyond the exit surface. This can be obtained using the external Green's function (3.45). The integrals over x', y' can again be evaluated using (3.27) and the result for the field *outside the crystal* is

$$\begin{aligned}\mathbf{E}_2(\mathbf{r})&=\boldsymbol{\gamma}\cdot\mathbf{P}_0\left(\frac{2n}{n+1}\right)e^{-\frac{1}{2}\alpha_2l}\\ &\times e^{2ik_1[l+(z-l)n^{-1}]}\frac{1}{1+i\xi_e}\int_0^l\frac{e^{-\alpha z'}}{1+i\xi'}\\ &\times\exp\left\{-\frac{2[(x-\rho(l-z'))^2+y^2]}{w_0^2(1+i\xi_e)}\right\}dz', \qquad (4.20)^*\end{aligned}$$

where

$$\xi_e=\frac{2}{b}[l-f+n(z-l)] \tag{4.21}$$

now replaces the ξ of (4.19). In the limit $z\rightarrow l+$(4.20) reduces to (4.19) multiplied by the transmission coefficient $2n/(n+1)$ of the exit surface. We might have deduced (4.20) from (4.19) by the following elementary arguments: (a) the transmission coefficient converts (4.19) to a field in air; (b) $\exp(-\frac{1}{2}\alpha_2z)$ becomes $\exp(-\frac{1}{2}\alpha_2l)$ since there is no absorption in the air; (c) in the phase-propagation factor $\exp(2ik_1z)$ we replace z by the equivalent optical path in the medium $l+(z-l)n^{-1}$; (d) in the spreading factor $(1+i\xi)^{-1}$ we replace z by $l+n(z-l)$ which is the distance in the medium for an equivalent spreading; (e) the double-refraction angle ρ should be multiplied by $l-z'$ rather than $z-z'$ since there is no double refraction in air. Notice that two different replacements of z are required to convert (4.19) into (4.20), the more important of which is the equivalent spreading distance which takes into account the fact that the beam spreads more rapidly in air than it would have spread in the medium because of refraction at the exit surface.

Associated with a given axis, focus, and parameters k_1, b, and w_0 there exists a complete set of modes of the electromagnetic field. The simplest of these modes are the Gaussian beams considered in this section. Analytical expressions for the higher modes have been given by Boyd and Gordon.[7] Although the mathematics is more complicated, higher modes in the paraxial approximation (4.8) can be handled by the methods of this section, since they all have the form of Gaussians multiplited by polynomials in x and y.

5. FAR-FIELD INTENSITY DISTRIBUTION

5.1 Far-Field Approximation

We come now to our main purpose in this paper which is to discuss SHG in the limit of the *far field*,

$$\xi \gg 1, \tag{5.1}$$

where ξ is defined by (4.2). Our discussion will be limited to Gaussian beams, but similar methods can also be applied to higher order modes. For simplicity we shall first assume that the point of observation x, y, z is *inside the crystal* or on its surface (just inside), so that (4.19) applies without the modifications in (4.20) required to represent the field at a point outside the crystal. We also assume the focus f lies inside the crystal well removed from the incident surface

$$f \gg b. \tag{5.2}$$

Finally, we assume

$$\rho \neq 0. \tag{5.3}$$

The case $\rho=0$ will be treated in Sec. 8.

Since the laser beam diverges in the far field at a constant angle δ_0 given in (4.7) it is convenient to describe the second harmonic field in terms of angle variables relative to δ_0. In place of x, y we denote points in the beam by the variables

$$s=\frac{x-\rho(z-f)}{\delta_0(z-f)}, \quad t=\frac{y}{\delta_0(z-f)}. \tag{5.4}$$

In practice the plane z will ordinarily be the exit surface $z=l$. The double refraction angle will be specified by

$$\beta=\rho/\delta_0 \neq 0. \tag{5.5}$$

There should be no confusion with β in (3.41) for which we have no further use. The point $s=t=0$ specifies the ρ line through the focus, while the beam axis $x=y=0$ is specified by $s=-\beta$, $t=0$. We also define the constants

$$q=\beta/\xi, \quad u_1=-\beta, \quad u_2=\beta f/(z-f). \tag{5.6}$$

The point $s=u_1$, $t=0$ denotes the beam axis while $s=u_2$, $t=0$ is the ρ line through the origin $x=y=z=0$ as shown in Fig. 2.

By (4.2) and (4.7) we have

$$\frac{1}{w_0^2(1+i\xi)}=\frac{1}{\delta_0^2(z-f)^2}(1-i\xi+\cdots),$$

neglecting terms of order ξ^{-2} or smaller compared with unity. The factor $(1+i\xi)^{-1}$ outside the integral (4.19) can be replaced by $(i\xi)^{-1}$. With these approximations (4.19) becomes in the *far field*

$$\mathbf{E}_2(\mathbf{r})=\boldsymbol{\gamma}\cdot\mathbf{P}_0\frac{b}{2\xi}e^{-\alpha_1 f-\frac{1}{2}\alpha_2(z-f)}e^{2ik_1z}e^{-2t^2(1-i\xi)} \times\int_{u_1}^{u_2}\frac{du}{u+iq}e^{2i\xi(s-u)^2}e^{cu-2(s-u)^2}, \tag{5.7}$$

where

$$c=(\alpha b/2\beta)\xi=\alpha(\delta_0/\rho)(z-f) \tag{5.8}$$

and the new integration variable u is related to ξ' of (4.19) as follows

$$u=-(\beta/\xi)\xi'. \tag{5.9}$$

In the angle variables s, t the polarization beam (4.9) is described by $\exp[-2t^2-2(s-u_1)^2]$; therefore we interpret the Gaussian factor $\exp[-2(s-u)^2]$ in the integral of (5.7) as arising from the Gaussian shape of the polarization beam. The factor $\exp(cu)$ represents absorption. We interpret the pole function $(u+iq)^{-1}$ as representing the focus. The remaining factor in the integral.

$$e^{2i\xi(u-s)^2} \tag{5.10}$$

is a rapidly oscillating phase factor. In the far field limit (5.1) the absorption and Gaussian factors are slowly varying functions of u compared to the phase factor (5.10). It is this fact which enables us to deduce the nature of the field in the far-field limit.

Let us write the field *inside the crystal* (5.7) approximately in the form

$$\mathbf{E}_2(\mathbf{r})=\boldsymbol{\gamma}\cdot\mathbf{P}_0\frac{b}{2\xi}e^{-\alpha_1 f-\frac{1}{2}\alpha_2(z-f)} \times e^{2ik_1z}e^{2i\xi t^2}e^{-2(s^2+t^2)}I(s,\xi), \tag{5.11}$$

where $I(s,\xi)$ is the integral

$$I(s,\xi)=\int_{u_1}^{u_2}\frac{du}{u+iq}e^{2i\xi(u-s)^2} \tag{5.12}$$

containing the pole and rapidly oscillating factor of the integral in (5.7). A slightly more general form will be used in the next section which makes (5.11) identical with (5.7). The slowly varying factors in the integral have here been taken outside the integral and given values corresponding to $u=0$. The validity of this choice will be discussed later. The factor ξ^{-1} and the absorption factor in (5.11) have the form to be expected if the SHG occurs very near the focal point f. The effects of the spatial extent of the focus are contained in the integral $I(s,\xi)$. The *intensity* as a function of s, t can be written

$$\begin{aligned} S(s,t) &= (nc/8\pi)|\mathbf{E}_2(\mathbf{r})|^2 \\ &= |\boldsymbol{\gamma}\cdot\mathbf{P}_0|^2 \frac{b^2nc}{32\pi\xi^2} e^{-2\alpha_1 f-\alpha_2(z-f)} \\ &\qquad \times e^{-4s^2-4t^2}|I(s,\xi)|^2. \end{aligned} \tag{5.13}$$

For quantitative considerations it is useful to eliminate $|\boldsymbol{\gamma}\cdot\mathbf{P}_0|^2$ and express $S(s,t)$ in terms of the laser power P_1; the intensity *inside the crystal* may be written

$$S(s,t)=\frac{K}{\pi}\frac{P_1{}^2k_1{}^2}{\xi^2}e^{-2\alpha_1 f-\alpha_2(z-f)}e^{-4(s^2+t^2)}|I(s,\xi)|^2, \qquad (5.14)^*$$

where K is the constant defined in (3.29) of BADK; for ADP or KDP

$$K=\frac{32\pi^2\omega^2}{(nc)^3}d_{36}{}^2\sin^2\theta_m. \tag{5.15}$$

The value[2,11,15] in ADP is $K \simeq 1.5\times10^{-16}$ esu for the 1.15-μ laser. It is clear that for any uniaxial crystal a constant K in (5.14) could be defined in terms of the appropriate components of the second-order polarization tensor **d**.

The validity of treating $\exp(cu)$ as slowly varying compared to the phase factor $\exp[2i\xi(u-s)^2]$ at $u=0$ depends on the condition

$$c \ll \left|\frac{d}{du}2\xi(u-s)^2\right|_{u=0},$$

which reduces to

$$|s| \gg \alpha b/8\beta. \tag{5.16}$$

It is reasonable to assume that this condition holds outside of a neighborhood about $s=0$ which is small compared to the domain of principal interest $u_1<s<u_2$. We shall proceed to investigate the behavior of $I(s,\xi)$ as a function of s without regard to the restriction (5.16), but it should be kept in mind that absorption could obscure some of the structure in $I(s,\xi)$ near $s=0$ and render it unobservable experimentally. A more specific criterion will be given in (6.70) and it will be shown that in a typical case absorption can be neglected.

5.2 Dominant Term in the Interior Field

We now consider the far-field limit in which the focus moves far from the incident surface at the same time the point of observation moves far from the focus. Mathematically, the limit may be specified by

$$f\to\infty\,,\quad z-f\to\infty\,,\quad f/(z-f)\to\text{const}, \tag{5.17}$$

which implies an *infinite crystal*. This limit isolates the focus from both the incident surface $z=0$ and the surface of observation z (which might be considered the exit surface). Therefore we would not expect the surfaces to influence the SHG in the limit (5.17). Let us write (5.12) in the form

$$I(s,\xi)=e^{2i\xi s^2}\int_{\xi u_1}^{\xi u_2}\frac{dv}{v+i\beta}e^{-4isv+2i(v^2/\xi)}. \tag{5.18}$$

From (5.6) we have in this limit

$$\begin{aligned} \xi u_1 &= -\beta(2/b)(z-f) \underset{z-f\to\infty}{\longrightarrow} -\infty\,, \\ \xi u_2 &= \beta(2/b)f \underset{f\to\infty}{\longrightarrow} \infty\,, \end{aligned} \tag{5.19}$$

providing $\beta\neq0$, so that the integration limits of (5.18) become infinite. Much the same effect is achieved by allowing the confocal parameter b to approach zero in a *finite crystal* with f and z fixed

$$b\to0\,, \tag{5.20}$$

which corresponds to the use of lenses of shorter and shorter focal length to produce the focus. From (4.1) and (4.7)

$$\delta_0=2/(bk_1)^{1/2}. \tag{5.21}$$

Since the theory of Gaussian beams is only valid in the paraxial approximation it must be understood in (5.20) that b must not become so small that $\delta_0\to1$ in (5.21). From (5.6) and (5.21) we have in the limit (5.20)

$$\begin{aligned} \xi u_1 &= -(k_1/b)^{1/2}\rho(z-f) \underset{b\to0}{\longrightarrow} -\infty\,, \\ \xi u_2 &= (k_1/b)^{1/2}\rho f \underset{b\to0}{\longrightarrow} \infty\,, \end{aligned} \tag{5.22}$$

which is equivalent to (5.19). It should be emphasized that we are not considering the simple limit $z\to\infty$, which will be considered in Sec. 7.

In the limit $\xi\to\infty$ by (5.17) or (5.20) we can write (5.18)

$$I(s,\xi) \underset{\xi\to\infty}{\longrightarrow} I_d(s,\xi)\,, \tag{5.23}$$

where

$$I_d(s,\xi)=e^{2i\xi s^2}\int_{-\infty}^{\infty}\frac{dv}{v+i\beta}e^{-4isv}. \tag{5.24}$$

The integral can be evaluated by contour integration in the complex v plane. If $s<0$, the contour must be com-

---

[15] R. C. Miller, D. A. Kleinman, and A. Savage, Phys. Rev. Letters **11**, 146 (1963).

pleted in the upper half-plane where the integrand is analytic. If $s>0$, the contour can be completed in the lower half plane containing the pole $v=-i\beta$ and the integral has the value $-2\pi i\exp(-4\beta s)$. Thus we obtain

$$I_d(s,\xi)=-2\pi i e^{2i\xi s^2}e^{-4\beta s}\theta(s)\,, \qquad (5.25)^*$$

where $\theta(s)$ is the *step function*

$$\begin{aligned}\theta(s)&=1, & s&>0\\ &=\tfrac{1}{2}, & s&=0\\ &=0, & s&<0.\end{aligned} \qquad (5.26)$$

We return to the approximation (5.11) and the question of why the slowly varying factors taken outside the integral should be evaluated at $u=0$. This is because the main contribution to (5.24) comes from the part of the contour passing near the pole. Since the contour is closest to the pole at $u=0$ this is the appropriate value to use in evaluating the slowly varying factors. In the next section, however, we shall find it necessary to reopen this question and to modify (5.11) when we consider small contributions to (5.7) from other parts of the contour.

It is clear that the discontinuity in $I_d(s,\xi)$ is to be associated with the *sharp edge* observed experimentally in far field intensity patterns; the region $s<0$ may be called the *dim region* and the region $s>0$ the *bright region* as suggested by photographs of the beam. If, in (5.11), we make the approximation

$$I(s,\xi)\approx I_d(s,\xi)\,, \qquad (5.27)$$

we obtain

$$\mathbf{E}_2(\mathbf{r})\approx\boldsymbol{\gamma}\cdot\mathbf{P}_0\frac{\pi b}{i\xi}e^{-\alpha_1 f-\frac{1}{2}\alpha_2(z-f)}$$
$$\times e^{2ik_1z+2i\xi(s^2+t^2)}e^{-2[s^2+t^2+2\beta s]}\theta(s)\,. \qquad (5.28)$$

The field strength according to (5.28) is shown schematically on the right in Fig. 2 by the curve labelled SHG. The plot shows the sharp edge at $s=0$ on the ρ line through the focus. The corresponding intensity according to (5.14) is

$$S(s,t)\sim4\pi K\frac{P_1{}^2k_1{}^2}{\xi^2}e^{-2\alpha_1f-\alpha_2(z-f)}e^{-4[s^2+t^2+2\beta s]}\theta(s)\,. \qquad (5.29)^*$$

We shall regard $I_d(s,\xi)$ as the *dominant term* in $I(s,\xi)$ since it becomes exact in the limit (5.17) and predicts the dominant feature seen in photographs of the beam. Features which are neglected in the approximation (5.27) we shall call *fine structure.*

Figure 19 shows the contours of equal intensity for the nominal matching case as observed in the st plane looking down the beam axis. The origin $s=t=0$ indicated by the solid dot is the ρ line through the focus. The beam axis is indicated by the open circle. The contours of intensity according to (5.29) are arcs of circles drawn with their centers at the beam axis; all of the contours are closed by a segment of the line $s=0$ at which the intensity is (approximately) discontinuous. The shape of the SHG pattern observed photographically will depend upon exposure; relatively long exposures will show the more distant (weaker) contours which tend to approach a semicircular shape; short exposures will show the near (stronger) contours which are very much elongated along the line $s=0$. It should also be mentioned that long exposures tend to bring out the fine structure which is not given by (5.29).

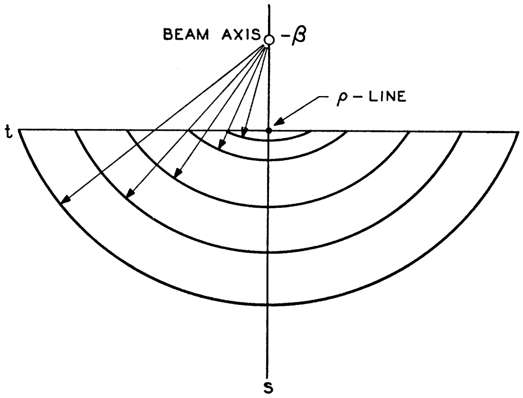

FIG. 19. Contours of intensity for the nominal matching case neglecting fine structure according to (5.29). The contours are arcs of circles centered on the beam axis $s=-\beta$, $t=0$ together with the line $s=0$. The ρ line through the focus shown in Fig. 2 intersects the s, t plane in the dot at $s=t=0$.

5.3 Exterior Field

We turn now to the case where the field is observed outside the crystal. The *external far field* condition is

$$\xi_e\gg1\,, \qquad (5.30)$$

where ξ_e has been defined in (4.21). We can write

$$\begin{aligned}\xi_e&=\frac{2}{b}(l-f)+\frac{2n}{b}(z-l)\\ &=\xi+\xi_{\rm air}\,,\end{aligned} \qquad (5.31)$$

where ξ here denotes the value of ξ defined in (4.2) at the crystal surface $z=l$. Two rather different cases are included in (5.30) depending on whether or not ξ satisfies the far field condition (5.1). We postpone until Sec. 7 the case in which (5.30) is satisfied by having $z\rightarrow\infty$. Here we consider the limit (5.20) which insures that $\xi\gg1$ as well as $\xi_e\gg1$. The field (4.20) can be cast into the form (5.7) providing somewhat more general definitions are given for the angle variables s, t and the parameters c, q, u_1, u_2. Retaining for convenience the same notation we define

$$s=\frac{x-\rho(l-f)}{\delta_0[l-f+n(z-l)]},\quad t=\frac{y}{\delta_0[l-f+n(z-l)]},\tag{5.32}$$

$$c=(\alpha b/2\beta)\xi_e,$$

$$q=\frac{\beta}{\xi_e},$$

$$u_1=-\beta\frac{l-f}{l-f+n(z-l)},\tag{5.33}$$

$$u_2=\beta\frac{f}{l-f+n(z-l)}.$$

Treating (4.20) exactly as we did (4.19) at the beginning of this section we obtain for the *external far field*

$$\mathbf{E}_2(\mathbf{r})=\boldsymbol{\gamma}\cdot\mathbf{P}_0\frac{b}{2\xi_e}\left(\frac{2n}{n+1}\right)e^{-\alpha_1 f-\frac{1}{2}\alpha_2(l-f)}$$
$$\times e^{2ik_1[l+(z-l)n^{-1}]}e^{-2t^2(1-i\xi_e)}$$
$$\times\int_{u_1}^{u_2}\frac{du}{u+iq}e^{2i\xi_e(s-u)^2}e^{cu-2(s-u)^2}.\tag{5.34}$$

Removing the slowly varying absorption and Gaussian factors as in (5.11) gives the field *outside the crystal*

$$\mathbf{E}_2(\mathbf{r})=\boldsymbol{\gamma}\cdot\mathbf{P}_0\frac{b}{2\xi_e}\frac{2n}{n+1}e^{-\alpha_1 f-\frac{1}{2}\alpha_2(l-f)}$$
$$\times e^{2ik_1[l+(z-l)n^{-1}]}e^{2i\xi_e t^2}e^{-2(s^2+t^2)}I(s,\xi_e),\tag{5.35}$$

where $I(s,\xi_e)$ is defined by (5.12). Later in (6.1) we shall define $I(s,\xi_e)$ more precisely so as to make (5.35) identical with (5.34).

The intensity *outside the crystal* may be written in the form (5.14)

$$S(s,t)=\frac{K}{\pi}\frac{P_1^2k_1^2}{\xi_e^2}\frac{4n}{(n+1)^2}e^{-2\alpha_1 f-\alpha_2(l-f)}$$
$$\times e^{-4(s^2+t^2)}|I(s,\xi_e)|^2,\tag{5.36*}$$

where $4n/(n+1)^2$ is the transmission coefficient of the exit surface of the crystal. In the limit (5.20) we have

$$I(s,\xi_e)\to I_d(s,\xi_e),\tag{5.37}$$

where $I_d(s,\xi_e)$ is given by (5.25). The intensity without fine structure outside the crystal is therefore

$$S(s,t)\approx 4\pi K\frac{P_1^2k_1^2}{\xi_e^2}\frac{4n}{(n+1)^2}e^{-2\alpha_1 f-\alpha_2(l-f)}$$
$$\times e^{-4(s^2+t^2+2\beta s)}\theta(s)\tag{5.38*}$$

in the nominal matching case.

The center of the arcs of constant intensity is again $s=-\beta$. In view of the new definition (5.35) for s, however, this no longer coincides with the beam axis $x=0$ located at

$$s_{\text{axis}}=-\beta\frac{l-f}{l-f+n(z-l)},\tag{5.39}$$

which satisfies

$$-\beta<s_{\text{axis}}<0$$
$$s_{\text{axis}}\underset{z\to\infty}{\longrightarrow}0\tag{5.40}$$
$$\underset{z\to l}{\longrightarrow}-\beta.$$

5.4 Summary

In this section we have obtained the limiting behavior of the second harmonic intensity distribution for a well localized focus in a crystal very long (or thick) compared to the confocal parameter, i.e., $l\gg b$. The limit may be taken either by allowing $l\to\infty$ while the focus remains near the center of the crystal and b is fixed, or by allowing $b\to 0$ with fixed l. The result is a very simple representation of the pattern which has a discontinuous edge at the ρ line through the focus ($s=0$) as shown in Fig. 2. On the bright side the intensity decays to zero like a Gaussian centered on the beam axis. This result represents the sharp edge and the gross intensity distribution of the pattern, mentioned in the Introduction as objectives (1) and (2) of the theory. Both the discontinuity and the absence of fine structure are the result of the limiting process. For simplicity in presentation we have restricted the discussion to the nominal matching case. It will be shown in Sec. 8. that the edge can be moved relative to the ρ line by a slight rotation of the crystal or any other procedure which mismatches the nominal wave vector of the laser beam. Thus in practice the edge will ordinarily not fall exactly at $s=0$.

6. WELL-DEVELOPED EDGE STRUCTURE

Although the dominant term (5.25) and the associated electric field (5.28) and intensity (5.29) describe the general nature of the SHG by nominally matched focused beams in the far field, the approximation (5.27) is unsatisfactory in three respects: (a) $I_d(s,\xi)$ is discontinuous at $s=0$, (b) $I_d(s,\xi)$ predicts zero field in the dim region, and (c) $I_d(s,\xi)$ contains no fine structure. In this section we shall obtain a continuous analytical approximation to $I(s,\xi)$ for the case in which the edge is very pronounced and the associated fine structure is primarily characteristic of a focus in an infinite medium and the specific effects of the surfaces of the crystal are very weak. We shall call this the case of *well-developed edge structure.* In the next section we shall consider *partially developed edge structure* which is important in many practical cases where the crystal is finite and we may have $\beta\ll 1$, or else the pattern is observed outside the crystal. The well-developed edge structure has a fine structure arising mainly from the term $2iv^2/\xi$ in the exponent of (5.18) [or $2i\xi u^2$ in (5.12)], whereas in the partially developed edge structure this term is negligible but there is a fine structure arising from the finite limits of integration. If $\beta\neq 0$ and if ξ can be increased indefinitely *within the medium*, then it is always possible to achieve a well developed edge structure, which is the subject of this section.

Since we are now interested in a higher approximation we must generalize the definition (5.12) of $I(s,\xi)$ so as to include the slowly varying terms. We shall assume that **r** lies *in the crystal* and continue to write $\mathbf{E}_2(\mathbf{r})$ as in (5.11) but (5.12) will be replaced by

$$I(s,\xi)=\int_{u_1}^{u_2}\frac{du}{u+iq}e^{2i\xi(u-s)^2}f(u,s), \qquad (6.1)^*$$

where

$$f(u,s)=e^{cu}e^{4us-2u^2} \qquad (6.2)$$

is the slowly varying factor and c is defined in (5.8). With $I(s,\xi)$ defined by (6.1) and (6.2) we see that (5.11) is identical with (5.7). We now decompose $I(s,\xi)$ as follows:

$$I(s,\xi)=I_\infty(s,\xi)+I_1(s,\xi)+I_2(s,\xi), \qquad (6.3)$$

where

$$I_\infty(s,\xi)=\int_{-\infty}^{\infty}\frac{du}{u+iq}e^{2i\xi(u-s)^2}f(u,s), \qquad (6.4)$$

$$I_1(s,\infty)=-\int_{-\infty}^{u_1}\frac{du}{u+iq}e^{2i\xi(u-s)^2}f(u,s), \qquad (6.5)$$

$$I_2(s,\infty)=-\int_{u_2}^{\infty}\frac{du}{u+iq}e^{2i\xi(u-s)^2}f(u,s). \qquad (6.6)$$

Note that $f(u,s)$ is well behaved as $u\rightarrow\pm\infty$. We shall find that $I_2(s,\xi)$ and $I_1(s,\xi)$ contribute fine structure associated with the incident and exit surfaces, respectively, while $I_\infty(s,\xi)$ contains fine structure associated with the sharp edge at $s=0$. It is clear from (5.24) that

$$I_\infty(s,\xi)\underset{\xi\rightarrow\infty}{\longrightarrow} I_d(s,\xi). \qquad (6.7)$$

We shall now develop the theory of $I(s,\xi)$ on the assumption that $I_\infty(s,\xi)$ is the most important term.

6.1 Edge Fine Structure

It follows readily from (6.4) that $I_\infty(s,\xi)$ satisfies the differential equation

$$\frac{dI_\infty}{ds}=4i\xi(s+iq)I_\infty-4i\xi\int_{-\infty}^{\infty}du e^{2i\xi(u-s)^2}f(u,s)+\int_{-\infty}^{\infty}\frac{du}{u+iq}\frac{\partial f}{\partial s}e^{2i\xi(u-s)^2}, \qquad (6.8)$$

considering $I_\infty(s,\xi)=I_\infty(s)$ as a function of s with ξ a parameter. The solution of (6.8) is made unique by requiring

$$I_\infty(-\infty)=0. \qquad (6.9)$$

From (6.2) we can write the last term of (6.8)

$$\int_{-\infty}^{\infty}du e^{2i\xi(u-s)^2}f(u,s)\frac{4u}{u+iq}. \qquad (6.10)$$

In the far field we have

$$|4u/(u+iq)|\leq 4\ll 4\xi, \qquad (6.11)$$

showing that the third term is negligible compared to the second term of (6.8). Thus we write

$$\frac{dI_\infty}{ds}=4i\xi(s+iq)I_\infty-4i\xi\int_{-\infty}^{\infty}du\, e^{2i\xi(u-s)^2}f(u,s). \qquad (6.12)$$

Since $f(u,s)$ is slowly varying compared to the phase factor, except in the region $u\sim s$, we may take $f(u,s)$ outside the integral

$$\frac{dI_\infty}{ds}=4i\xi(s+iq)I_\infty-4i\xi f(s,s)\int_{-\infty}^{\infty}du\, e^{2i\xi(u-s)^2}. \qquad (6.13)$$

By (3.27)

$$\int_{-\infty}^{\infty}du\, e^{2i\xi(u-s)^2}=\left(\frac{\pi}{2\xi}\right)^{1/2}e^{i\pi/4}, \qquad (6.14)$$

so that (6.13) becomes

$$\frac{dI_\infty}{ds}=4i\xi(s+iq)I_\infty-(8\pi\xi)^{1/2}e^{i3\pi/4}f(s,s). \qquad (6.15)$$

We first consider the relationship of $I_\infty(s,\xi)$ to $I_d(s,\xi)$. If $s\neq 0$ and $I_\infty\neq 0$, the leading term on the right of (6.15) is $4i\xi sI_\infty$. Let us neglect the second term completely and consider the approximate equation

$$\frac{dI_\infty}{ds}\approx 4i\xi(s+iq)I_\infty. \qquad (6.16)$$

For $s\neq 0$ the solutions of (6.16) are

$$\begin{aligned}&I_\infty(s,\xi)\approx 0,\\&I_\infty(s,\xi)\approx Ae^{2i\xi s^2}\cdot e^{-4\beta s},\end{aligned} \qquad (6.17)$$

where A is a constant. Neither of the solutions (6.17) is satisfactory by itself; the solutions must be joined discontinuously at a suitable point to make a physically interesting solution. Evidently the only point at which a discontinuity can be allowed is $s=0$ where (6.16) is not valid. Thus we are led to a solution of the form $I_d(s,\xi)$ given by (5.25), although these arguments do not determine the constant in (6.17). The inhomogeneous term in (6.15) determines the constant as well as the fine structure associated with the edge at $s=0$.

To solve (6.15) we transform it to the form

$$\frac{dJ}{ds}=-4\beta J-(8\pi\xi)^{1/2}e^{i3\pi/4}e^{-2i\xi s^2}f(s,s)\,, \qquad (6.18)$$

where

$$J(s,\xi)=e^{-2i\xi s^2}I_\infty(s,\xi)\,. \qquad (6.19)$$

The dominant term in $J(s,\xi)$ is

$$J_d(s,\xi)=-2\pi ie^{-4\beta s}\theta(s)\,. \qquad (6.20)$$

We obtain a good approximate solution of (6.18) by setting $J(s,\xi)=J_d(s,\xi)$ on the right side. For $s\leq 0$, we obtain

$$J(s,\xi)_{s\leq 0}=-(8\pi\xi)^{1/2}e^{i3\pi/4}\int_{-\infty}^{s} e^{-2i\xi s'^2}f(s',s')ds'\,, \qquad (6.21)$$

and for $s>0$,

$$J(s,\xi)_{s>0}=2\pi i(1-e^{-4\beta s})$$
$$-(8\pi\xi)^{1/2}e^{i3\pi/4}\int_{-\infty}^{s} e^{-2i\xi s'^2}f(s',s')ds'\,. \qquad (6.22)$$

We can take the slowly varying factor $f(s',s')$ outside the integral providing we evaluate it at the appropriate value of s' giving the main contribution to the integral. The main contribution comes from the region where the phase factor $e^{-2i\xi s'^2}$ is least rapidly oscillating; in the case of (6.21) this is $s'\sim s$. In the case of (6.22), we write

$$\int_{-\infty}^{s} e^{-2i\xi s'^2}f(s',s')ds'=\int_{-\infty}^{\infty} e^{-2i\xi s'^2}f(s',s')ds'$$
$$-\int_{s}^{\infty} e^{-2i\xi s'^2}f(s',s')ds'\,. \qquad (6.23)$$

In the first term the important region is $s'\sim 0$ while in the second it is $s'\sim s$. Thus, we can write (6.21) in the form

$$J(s,\xi)_{s\leq 0}=-(8\pi\xi)^{1/2}e^{i3\pi/4}f(s,s)\int_{-\infty}^{s} e^{-2i\xi s'^2}ds'\,, \qquad (6.24)$$

and (6.22) in the form

$$J(s,\xi)_{s>0}=-2\pi ie^{-4\beta s}$$
$$+(8\pi\xi)^{1/2}e^{i3\pi/4}f(s,s)\int_{s}^{\infty} e^{-2i\xi s'^2}ds'\,, \qquad (6.25)$$

where use has been made of (6.14) and the relation $f(0,0)=1$.

The integrals in (6.24) and (6.25) are related to the *Fresnel integrals* familiar in the theory of diffraction.[16] We define the complex Fresnel integral

$$F(z)=C(z)+iS(z)=\int_0^z e^{i(\pi/2)\tau^2}d\tau\,, \qquad (6.26)$$

where the usual Fresnel integrals are

$$\begin{aligned} C(z)&=\int_0^z \cos\frac{\pi}{2}\tau^2 d\tau\,,\\ S(z)&=\int_0^z \sin\frac{\pi}{2}\tau^2 d\tau\,. \end{aligned} \qquad (6.27)$$

The asymptotic behavior of these functions for large (positive or negative) real argument is given by

$$\begin{aligned} C(z)&=\frac{1}{2}\frac{z}{|z|}+\frac{1}{\pi z}\sin\frac{\pi}{2}z^2+\cdots\,,\\ S(z)&=\frac{1}{2}\frac{z}{|z|}-\frac{1}{\pi z}\cos\frac{\pi}{2}z^2+\cdots\,,\\ F(z)&=\frac{1+i}{2}\frac{z}{|z|}-\frac{i}{\pi z}e^{i(\pi/2)z^2}+\cdots\,. \end{aligned} \qquad (6.28)$$

The integrals in (6.24) and (6.25) can be written

$$\begin{aligned} \int_{-\infty}^{s} e^{-2i\xi s'^2}ds'&=\left(\frac{\pi}{4\xi}\right)^{1/2}\left[F^*\left(s\left(\frac{4\xi}{\pi}\right)^{1/2}\right)+\frac{1-i}{2}\right],\\ \int_{s}^{\infty} e^{-2i\xi s'^2}ds'&=\left(\frac{\pi}{4\xi}\right)^{1/2}\left[\frac{1-i}{2}-F^*\left(s\left(\frac{4\xi}{\pi}\right)^{1/2}\right)\right]. \end{aligned} \qquad (6.29)$$

It is convenient to combine (6.24) and (6.25) into a single equation

$$J(s,\xi)=J_d(s,\xi)+\pi i[\theta(s)-\theta(-s)]$$
$$\times\left[1-(1+i)F^*\left(|s|\left(\frac{4\xi}{\pi}\right)^{1/2}\right)\right], \qquad (6.30)$$

where $\theta(s)$ is defined in (5.26). The asymptotic form valid for $|s|>(\pi/4\xi)^{1/2}$ is

$$J(s,\xi)=J_d(s,\xi)+\left(\frac{\pi}{2\xi}\right)^{1/2}e^{i\pi/4}\frac{f(s,s)}{s}e^{-2i\xi s^2}+\cdots\,. \qquad (6.31)$$

Higher approximations to $J(s,\xi)$ could be obtained by an iteration procedure, the next step of which would be to substitute (6.30) into the right side of (6.18). When this is done the term $J_d(s,\xi)$ will lead again to (6.30) and the second term will give an additional correction whose asymptotic form is

$$\Delta J(s,\xi)\sim\left(\frac{\pi}{2\xi}\right)^{1/2}e^{i\pi/4}e^{-2i\xi s^2}\frac{f(s,s)}{s}\left(\frac{iq}{|s|}\right). \qquad (6.32)$$

---

[16] Reference 13, Sec. 8.7.

From (3.5) we see that q is of order ξ^{-1} so $\Delta J(s,\xi)$ is of order $\xi^{-3/2}$ and will be neglected compared to the second term of (6.31). For $s=0$ (6.32) is not valid, but then it is easy to show that $\Delta J(0,\xi)$ is of order $\xi^{-1/2}$ compared to $J(0,\xi)=-\pi i$. Furthermore, (6.32) cannot cause additional structure because it is identical with the second term of (6.31) multiplied by $(iq/|s|)$. This justifies the approximation (6.30), which we now write in the form

$$I_\infty(s,\xi)=I_d(s,\xi)+\pi i[\theta(s)-\theta(-s)]$$
$$\times\left[1-(1+i)F^*\left(|s|\left(\frac{4\xi}{\pi}\right)^{1/2}\right)\right]e^{2i\xi s^2}f(s,s). \quad (6.33)^*$$

The asymptotic form (6.31) valid for $|s|>(\pi/4\xi)^{1/2}$ becomes

$$I_\infty(s,\xi)=I_d(s,\xi)+\left(\frac{\pi}{2\xi}\right)^{1/2}e^{i\pi/4}\frac{f(s,s)}{s}+\cdots. \quad (6.34)^*$$

This approximation neglects terms of order $\xi^{-3/2}$ in the asymptotic form and of order $\xi^{-1/2}$ at $s=0$. The second term of (6.33) represents the *edge fine structure* associated with the sharp edge at $s=0$ in the dominant term $I_d(s,\xi)$.

We shall show later that $I_\infty(s,\xi)$ is principally responsible for the observed SHG by focused beams if ξ is sufficiently large. Therefore, we proceed immediately to consider the *intensity* ignoring for the present the terms $I_1(s,\xi)$ and $I_2(s,\xi)$ in (6.3). The intensity is given by (4.13) with $I(s,\xi)$ now defined by (6.1) and for the present approximated by $I_\infty(s,\xi)$. We are interested primarily in the dependence of $S(s,t)$ on s which is governed by the function $e^{-4s^2}|I(s,\xi)|^2$. From (6.33) and (6.26),

$$|I_\infty(s,\xi)|^2=4\pi^2\{\theta(s)e^{-8\beta s}-\theta(s)e^{-4\beta s}f(s,s)(1-C-S)$$
$$+\tfrac{1}{2}f(s,s)^2[(C-\tfrac{1}{2})^2+(S-\tfrac{1}{2})^2]\}, \quad (6.35)^*$$

where the argument of C, S is $|s|(4\xi/\pi)^{1/2}$. For the case of *no absorption* ($\alpha=0$) (6.2) gives

$$f(s,s)=e^{2s^2}, \quad (6.36)$$

and the s dependence of the intensity is given by

$$(2\pi)^{-2}e^{-4s^2}|I_\infty(s,\xi)|^2=\theta(s)e^{-2h}-\theta(s)e^{-h}(1-C-S)$$
$$+\tfrac{1}{2}[(C-\tfrac{1}{2})^2+(S-\tfrac{1}{2})^2], \quad (6.37)$$

where

$$h=2s^2+4\beta s. \quad (6.38)$$

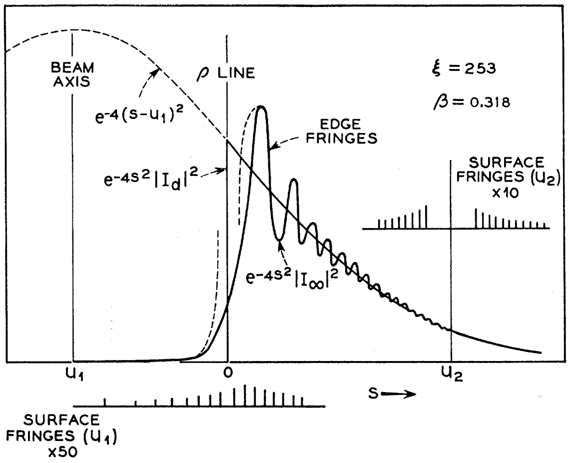

FIG. 20. Intensity distribution in a typical well-developed edge is shown by solid curve for the nominal matching case according to (6.37) and (6.44). Surface structure according to (6.69) is indicated by the positions of the fringes, but is too weak to show directly on the continuous curve. The dominant term in the intensity is shown lightly and its (imaginary) extension to form a Gaussian centered on the beam axis is shown dashed. The first two terms of (6.39) are shown dashed on the right of $s=0$ and the third term of (6.39) is shown dashed on the left of $s=0$ where these asymptotic approximations deviate from the true curve.

The first term of (6.35) is the dominant term squared $|I_d(s,\xi)|^2$, the second term is the interference between $I_d(s,\xi)$ and the edge fine structure, the third term is the square of the edge fine structure. This is the only term of (6.35) which gives intensity on the *dim side* $s<0$. As $s\to 0$, this term approaches the correct value π^2 for $|I_\infty(0,\xi)|^2$ while the first two terms of (6.35) cancel. On the *bright side*, $s>0$, the third term rapidly becomes negligible compared with the second term. The asymptotic form of (6.35) valid for $|s|>(\pi/4\xi)^{1/2}$ is

$$(2\pi)^{-2}I_\infty(s,\xi)^2=\theta(s)e^{-8\beta s}$$
$$+\theta(s)e^{-4\beta s}f(s,s)\frac{\sin(2\xi s^2-\pi/4)}{s(2\pi\xi)^{1/2}}$$
$$+\frac{1}{8\pi\xi s^2}f(s,s)^2+\cdots. \quad (6.39)^*$$

The second and third terms of (6.39) arise from the second and third terms of (6.35), respectively. We see in (6.39) that the second term is oscillatory and produces a series of maxima and minima of decreasing amplitude as s increases. We shall refer to the maxima as *edge fringes*. The locations of the edge fringes are correctly given by the asymptotic form (6.39) even for the first fringe; the locations relative to the edge are approximately

$$s^{(j)}=(2\xi)^{-1/2}[(3\pi/4)+2\pi(j-1)]^{1/2}$$
$$j=1,2,3,\cdots. \quad (6.40)^*$$

Here we are neglecting the effects of s^{-1} as well as the exponential factors e^{-4s^2}, $e^{-4\xi qs}$, and $f(s,s)$ on the edge fringes. For analyzing experimental data it is useful to work with the *fringe spacing ratio* defined by

$$R(j)\equiv\frac{s^{(j)}-s^{(1)}}{s^{(2)}-s^{(1)}}$$
$$=\frac{((j-1)+0.375)^{1/2}-(0.375)^{1/2}}{(1.375)^{1/2}-(0.375)^{1/2}}. \quad (6.41)^*$$

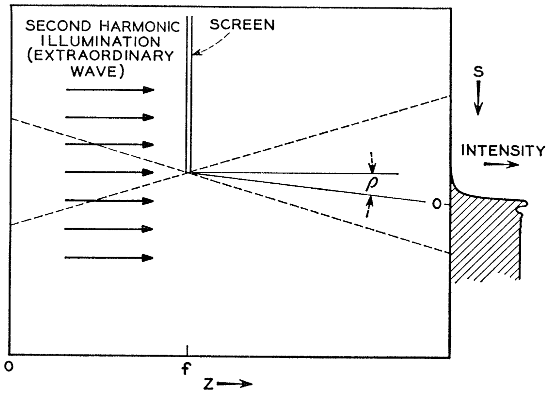

FIG. 21. Diffraction of second-harmonic light by a real straight-edged opaque screen to produce a pattern closely related to that produced in SHG by a laser beam focused at the position of the screen. The edge intensity pattern (6.48) is indicated on the right, and the imaginary laser beam is suggested by dashed lines crossing at the screen edge.

This is a universal function of the fringe number j. A less convenient but more accurate expression for $R(j)$ may be obtained by taking into account to lowest order the effects of the exponential factors; the result may be written

$$R(j)=\frac{((j-1)+0.375-\delta(j))^{1/2}-(0.375-\delta(1))^{1/2}}{(1.375-\delta(2))^{1/2}-(0.375-\delta(1))^{1/2}}, \qquad (6.42)^*$$

where

$$\delta(j)=(2\pi/\xi)^{1/2}(\beta+s^{(j)})\exp[-4\beta s^{(j)}-2s^{(j)2}] \qquad (6.43)$$

depends upon β and ξ as well as j.

Figure 20 shows the intensity as a function of the angle variable s defined in (5.4) for a well developed edge in the absence of absorption. The solid curve is calculated from (6.37) for the case

$$\begin{aligned}\beta&=0.318,\\ \xi&=253,\\ f/z&=10/17,\\ \alpha&=0.\end{aligned} \qquad (6.44)$$

These conditions, except for the complete absence of absorption, could be realized experimentally as follows:

Crystal: ADP ($\rho=0.03$ rad) oriented for the nominal matching case having length $l=1.7$ cm;
Beam: $\lambda_1=1.153\ \mu$, spot size $=0.17$ cm; (6.45)
Lens: focal length $L=1.2$ cm, placed so as to focus the beam at a depth $f=1.0$ cm in the crystal.

The focus would then have the parameters

$$\begin{aligned}w_0&=2.6\times10^{-4}\text{ cm},\\ b&=5.5\times10^{-3}\text{ cm},\\ \delta_0&=0.094\text{ rad}.\end{aligned} \qquad (6.46)$$

The pattern at the exit surface of the crystal $z=l$, $\xi=(2/b)(l-f)$ is then characterized by the parameters (6.44). It will be shown in the next section that the neglect of absorption in this example is completely justified. The dominant term $e^{-4s^2}|I_d|^2$ defined by (5.25) is shown as a light solid curve in Fig. 20, the extension of the dominant term to form the Gaussian profile of the polarization beam proportional to $\exp[-4(s-u_1)^2]$ is shown dashed, and the asymptotic forms from (6.39) where they depart seriously from the exact curve are also shown dashed. The curve extends only to u_1 on the dim side $s<0$, and the edge fringes extend only to u_2 on the bright side $s>0$ as required by (6.61) to be derived shortly. Structure in the intensity due to $I_1(s,\xi)$ and $I_2(s,\xi)$ is indicated by the lines called "u_1 surface fringes" and "u_2 surface fringes," respectively.

6.2 Diffraction by a Straight Edge

We now consider an interesting analogy between the edge fringes in SHG and the diffraction pattern produced by a *real straight edge.* Mathematically the analogy may be developed immediately from (6.35) by making the approximations

$$e^{-4s^2}\approx1,\quad e^{-8\beta s}\approx1,\quad e^{-4\beta s}\approx1,\quad f(s,s)\approx1. \qquad (6.47)$$

Then the intensity is proportional to

$$|I_\infty(s,\xi)|^2\approx2\pi\left\{\left[C\left(s\left(\frac{4\xi}{\pi}\right)^{1/2}\right)+\frac{1}{2}\right]^2+\left[S\left(s\left(\frac{4\xi}{\pi}\right)^{1/2}\right)+\frac{1}{2}\right]^2\right\}, \qquad (6.48)$$

where s in the argument can now have either sign. This function is familiar from the theory of Fresnel diffraction by a straight edge.[16] Figure 21 shows schematically the arrangement to produce the edge diffraction pattern (6.48) with a real straight edge. The laser beam of Fig. 2 is indicated by light dotted lines crossing at the focus f where the opaque screen is placed having a straight edge normal to the plane of the figure. The laser beam is only indicated for reference; the intensity pattern plotted on the right is produced by diffraction of the second harmonic plane extraordinary wave incident from the left in the z direction. This analogy completely justifies our referring to the maxima in $|I_\infty(s,\xi)|^2$ as edge fringes.

6.3 Surface Fine Structure

We must now consider the integrals $I_1(s,\xi)$ and $I_2(s,\xi)$ in (6.3) which have so far been neglected. We may expect that these integrals contain structure associated with the finite limits of integration in (6.1), which in turn are associated with the crystal surfaces. We have previously emphasized in the discussion of (3.25) that any surface z within the crystal is like an exit surface, since the region outside of z has no effect on the pattern at z and could be cut away. We see from Fig. 2 that the point u_1 corresponds to the z or exit surface, while the point $u=0$ is connected by a ρ line with the focus and therefore corresponds to the focus, and u_2 corresponds to the incident surface. The integrals $I_1(s,\xi)$ and $I_2(s,\xi)$, in addition to causing exit (u_1) and incident (u_2) *surface fine structure* respectively, also contribute in a very important way to the edge structure. We begin by writing (6.5) in the form

$$I_1(s,\xi)=-\int_{-\infty}^{u_1}\frac{du(u-s)}{s+iq}\left[\frac{1}{u-s}-\frac{1}{u+iq}\right]\times f(u,s)e^{2i\xi(u-s)^2}. \qquad (6.49)$$

Retaining the first term and integrating the second term by parts gives

$$I_1(s,\xi)=-\frac{1}{s+iq}\int_{-\infty}^{u_1}du f(u,s)e^{2i\xi(u-s)^2}+\frac{f(u_1,s)e^{2i\xi(u_1-s)^2}}{4i\xi(s+iq)(u_1+iq)}-\frac{1}{4i\xi(s+iq)}\times\int_{-\infty}^{u_1}du f'(u,s)e^{2i\xi(u-s)^2}, \qquad (6.50)$$

where

$$f'(u,s)=\frac{d}{du}\left(\frac{f(u,s)}{u+iq}\right). \qquad (6.51)$$

It will now be shown that the third term of (6.50) is not of interest. We may neglect iq in all the denominators and treat $f(u,s)$ and $f'(u,s)$ as slowly varying functions after the manner of (6.21) and (6.22).

Thus, (6.50) becomes

$$I_1(s,\xi)=-\frac{1}{s}\left(\frac{\pi}{2\xi}\right)^{1/2}e^{i\pi/4}\left[f(s,s)+\frac{f'(s,s)}{4i\xi}\right]\theta(u_1-s)+\frac{1}{s}\left(\frac{\pi}{4\xi}\right)^{1/2}\left[\frac{1+i}{2}-F\left(|u_1-s|\left(\frac{4\xi}{\pi}\right)^{1/2}\right)\right]\times\left[f(u_1,s)+\frac{f'(u_1,s)}{4i\xi}\right][\theta(u_1-s)-\theta(s-u_1)]+\frac{f(u_1,s)e^{2i\xi(u_1-s)^2}}{4i\xi u_1 s}. \qquad (6.52)$$

This expression is actually continuous at $s=u_1$ despite the presence of the step functions. We may write (5.51) in the approximate form

$$f'(u,s)=-f(u,s)/u^2. \qquad (6.53)$$

Therefore, $f'(s,s)$ may be neglected in the first term of (6.52) if

$$4\xi s^2\gg 1, \qquad (6.54)$$

which is essentially the condition for the validity of the asymptotic form (6.34) of $I_\infty(s,\xi)$. To determine the conditions for neglecting $f'(u_1,s)$ we write (6.52) in asymptotic form

$$I_1(s,\xi)=-\frac{1}{s}\left(\frac{\pi}{2\xi}\right)^{1/2}e^{i\pi/4}f(s,s)\theta(u_1-s)-\frac{f(u_1,s)e^{2i\xi(u_1-s)^2}}{4i\xi u_1(u_1-s)}-\frac{f'(u_1,s)}{4i\xi}\frac{e^{2i\xi(u_1-s)^2}}{4i\xi s(u_1-s)}, \qquad (6.55)$$

retaining $f'(u_1,s)$ but neglecting $f'(s,s)$, which is valid if (6.54) and also

$$4\xi(u_1-s)^2\gg 1 \qquad (6.56)$$

are satisfied. Again using (6.53) we see that $f'(u_1,s)$ may be neglected in (6.55) if

$$|4\xi u_1 s|\gg 1. \qquad (6.57)$$

A completely similar treatment of $I_2(s,\xi)$ gives

$$I_2(s,\xi)=-\frac{1}{s}\left(\frac{\pi}{2\xi}\right)^{1/2}e^{i\pi/4}f(s,s)\theta(s-u_2)+\frac{f(u_2,s)e^{2i\xi(u_2-s)^2}}{4i\xi u_2(u_2-s)}+\frac{f'(u_2,s)e^{2i\xi(u_2-s)^2}}{4i\xi s(u_2-s)} \qquad (6.58)$$

valid if (6.54) and also

$$4\xi(u_2-s)^2\gg 1 \qquad (6.59)$$

are satisfied. Here $f'(u_2,s)$ may be neglected if

$$|4\xi u_2 s|\gg 1. \qquad (6.60)$$

6.4 Conditions for a Well-Developed Edge

The contributions of $I_1(s,\xi)$ and $I_2(s,\xi)$ to the edge structure are given by the first terms of (6.55) and (6.58), respectively. These terms exactly cancel the edge term in the asymptotic approximation (6.34). It follows that there exists a definite *edge-structure region*

$$u_1<s<u_2. \qquad (6.61)^*$$

The second terms of (6.55) and (6.58) give the exit (u_1) and incident (u_2) surface fine structure, respectively. The third terms of these expressions will be neglected, which means that we are completely neglecting the third term of (6.50). As we have shown, this is an asymptotic approximation requiring for its validity the conditions (6.54), (6.57), and (6.60). It should not be inferred from this that anything mysterious happens to the surface fine structure near $s=0$. In the next section we shall investigate it more thoroughly under conditions in which it is the dominant structure. In the spirit of the far-field limit (5.17) it is of interest to consider the order of magnitude with regard to ξ of the terms retained and neglected in (6.55). We retain the edge and surface terms of (6.55) which are of order $\xi^{-1/2}$ and ξ^{-1}, respectively. We have neglected a term of order $\xi^{-3/2}$ when we neglected iq in the edge term and another term of order $\xi^{-3/2}$ when we neglected $f'(s,s)$. Terms of order ξ^{-2} are neglected when we neglect iq in the surface term and $f'(u_1,s)$. Thus we have consistently retained terms in $I(s,\xi)$ of order $\xi^{-1/2}$ and ξ^{-1}. This shows that as the limit (5.17) is taken for any given $s\neq 0$ our approximations will ultimately become valid and constitute the logical next approximation to the dominant term (5.25). In this sense the edge structure is of a larger order of magnitude ($\xi^{-1/2}$) than the surface structure (ξ^{-1}). Adding (6.34), (6.55), and (6.58) [neglecting $f'(u,s)$] gives our *final asymptotic expression* for $I(s,\xi)$ according to (6.3)

$$I(s,\xi)=I_d(s,\xi)+[\theta(s-u_1)-\theta(s-u_2)]$$
$$\times\frac{f(s,s)}{s}\left(\frac{\pi}{2\xi}\right)^{1/2}e^{i\pi/4}-\frac{f(u_1,s)}{4i\xi u_1(u_1-s)}e^{2i\xi(u_1-s)^2}$$
$$+\frac{f(u_2,s)}{4i\xi u_2(u_2-s)}e^{2i\xi(u_2-s)^2}+\cdots. \qquad (6.62)^*$$

The *conditions for validity* of this expression we now bring together and write in the form

$$|s|>(\pi/4\xi)^{1/2},\quad |u_1-s|>(\pi/4\xi)^{1/2},$$
$$|u_2-s|>(\pi/4\xi)^{1/2} \qquad (6.63)$$

$$|4\xi u_1 s|>\pi,\quad |4\xi u_2 s|>\pi. \qquad (6.64)$$

The three conditions (6.63), which are more explicit forms of (6.54), (6.56), and (6.59), insure the validity of of using asymptotic forms for the Fresnel integrals. The two conditions (6.64) are more explicit forms of (6.57) and (6.60); we shall see in the next section that these conditions are related to the use of asymptotic forms for sine and cosine integral functions.

In this section we are concerned not only with the validity of the expression (6.62), but also with the conditions for well developed edge structure. The basic condition can be stated very simply: The characteristic scale of the edge structure, which we see from (6.48) may be taken to be $(\pi/4\xi)^{1/2}$, must be much smaller than the edge structure region

$$u_1<\pm(\pi/4\xi)^{1/2}<u_2. \qquad (6.65)$$

This is actually two conditions which may be written

$$\begin{aligned}&\beta\xi^{1/2}>1,\\ &\beta\xi^{1/2}>(z-f)/f,\end{aligned} \qquad (6.66)$$

since $(\pi/4)^{1/2}\approx 1$. If the far field limit is taken by (5.17) the left side increases indefinitely and well developed edge structure must ultimately be obtained. This limit, however, requires an infinite crystal, and it may not be possible to satisfy (6.66) in a given crystal. According to (5.21) the condition can be written in the alternative form

$$\begin{aligned}&\rho(k_1(z-f)/2)^{1/2}>1\\ &\rho(k_1f/2)^{1/2}>((z-f)/f)^{1/2},\end{aligned} \qquad (6.67)$$

which does not contain b. Therefore the limit (5.20) does not insure that a well-developed edge will be obtained in a given crystal. From (6.67) we can deduce a convenient criterion for the *possibility* of observing well-developed edge structure in a given crystal at a given laser frequency

$$\rho>(2/k_1l)^{1/2}, \qquad (6.68)$$

where l is the crystal thickness. This is a more explicit form of our previous assumption (5.3).

We now compute the *intensity including fine structure* proportional to $e^{-4s^2}|I(s,\xi)|^2$ according to (5.14). In squaring (6.62) we shall retain only the leading fine-structure terms; on the bright side $s>0$ we neglect products of surface terms and products of the edge term with surface terms; on the dim side $s<0$ we neglect products of surface terms. Thus we obtain

$$|I(s,\xi)|^2=4\pi^2e^{-8\beta s}\theta(s)+[\theta(s)-\theta(s-u_2)]4\pi\left(\frac{\pi}{2\xi}\right)^{1/2}\frac{f(s,s)}{s}e^{-4\beta s}\sin(2\xi s^2-\pi/4)$$
$$+[\theta(s-u_1)-\theta(s-u_2)]\left(\frac{\pi}{2\xi}\right)\frac{f(s,s)^2}{s^2}+\theta(s)\frac{f(u_1,s)}{u_1(s-u_1)}\frac{\pi}{\xi}e^{-4\beta s}\cos(2\xi u_1^2-4\xi s u_1)$$
$$+\theta(s)\frac{f(u_2,s)}{u_2(u_2-s)}\frac{\pi}{\xi}e^{-4\beta s}\cos(2\xi u_2^2-4\xi u_2 s)+[\theta(s-u_1)-\theta(s)]\left(\frac{\pi}{2\xi}\right)^{1/2}\frac{f(s,s)f(u_1,s)}{2\xi u_1(s-u_1)s}\sin[2\xi(u_1-s)^2-\pi/4]$$
$$+[\theta(s-u_1)-\theta(s)]\left(\frac{\pi}{2\xi}\right)^{1/2}\frac{f(s,s)f(u_2,s)}{2\xi u_2(u_2-s)s}\sin[2\xi(u_2-s)^2-\pi/4]+\cdots. \qquad (6.69)^*$$

This relation contains the principal results of this section. The first three terms of (6.69) give the *edge pattern.* The fourth and fifth terms give the *surface fringes* on the bright side, while the sixth and seventh terms give the *surface fringes* on the dim side. The terms retained give no intensity for $s<u_1$, as shown in Fig. 20 by the termination of the curve. In locating the surface fringes near u_1 or u_2 the rule should be followed that there are *no* u_2 *fringes closer than* $(\pi/4\xi)^{1/2}$ to u_2, and similarly no u_1 fringes lie closer than $(\pi/4\xi)^{1/2}$ to u_1. In Fig. 20 are shown the u_2 fringes near u_2 and the u_1 fringes extending from u_1 past $s=0$. The fringe which violates (6.64) has been omitted. Both surface fringe systems are too weak to plot directly in the continuous curve representing the intensity. According to (6.69) the spacing of the surface fringes is constant on the bright side $s>0$ but variable on the dim sides $s<0$. Notice also the gap in the u_2 fringes at $s=u_2$; within this gap the edge fringes die out and are invisible on the far side $s>u_2$.

We have treated absorption in this section in an approximate way by including it in the slowly varying factor $f(u,s)$. The criterion (5.16) for the validity of this procedure can now be made more explicit by replacing $|s|$ on the left with $(\pi/4\xi)^{1/2}$

$$(\pi/4\xi)^{1/2}>\alpha b/8\beta. \tag{6.70}$$

This can be written in a form which is independent of the focal parameters w_0, b, δ_0

$$[(z-f)\lambda_1]^{1/2}(\alpha/2\pi\rho n^{1/2})<1, \tag{6.71}$$

where λ_1 is the laser wavelength in air. For ADP the values $\alpha=0.139$ cm^{-1}, $\rho=0.03$ rad, $n=1.5$ may be obtained from BADK, we may take $\lambda_1=1.153\times10^{-4}$ cm and $z-f=5$ cm as typical values, and then the left side of (6.71) becomes $=0.1$. It follows that (6.71) can readily be satisfied in ADP when the criterion (6.66) for the well developed edge is also satisfied. The value of the constant c in (6.2) for the conditions (6.45) is $c=0.3$, which justifies the complete neglect of absorption in Fig. 20. The greatest affect of absorption would be on the strength of the surface fine structure. It is easy to see physically, or from (6.69), that $\alpha>0$ favors the incident surface (u_2) structure while $\alpha<0$ favors the exit surface (u_1) structure. These effects will be clearly discussed in the next section where surface structure becomes very prominent.

We turn now to the pattern *outside the crystal.* The field is given by (5.35), which is in the same form as (5.11) except that ξ_e replaces ξ and the variables and parameters are defined by (5.32) and (5.33). We write $I(s,\xi_e)$ in the form (6.1) for consideration of the fine structure. Our principal result (6.69) still holds in the new variables with ξ_e replacing ξ. The criterion for the well developed edge structure, in addition to (5.30), is that the limits u_1, u_2 now given by (5.33) must be large compared to the characteristic scale $(\pi/4\xi_e)^{1/2}$ of the edge structure. This requirement may be written

$$\begin{aligned}\beta\xi_e^{1/2}&>(b/2f)\xi_e\\&>[b/2(l-f)]\xi_e,\end{aligned} \tag{6.72}$$

which differs from (6.66), and cannot be satisfied for arbitrarily large ξ_e. As ξ_e increases a well-developed edge eventually changes into a *partially developed edge* to be described in the next section.

6.5 Position of Pattern

As will be shown in Sec. 9 the edge structure derived in this section is in agreement with experiment. In practice, however, it is not possible to set up with any degree of certainty the nominal matching case we have assumed, and the position of the edge is sensitive to extremely small deviations of the crystal orientation from nominal matching. Fortunately the edge structure and surface structure are essentially independent of the position of the edge. It will be shown in Sec. 8 that the necessary generalization of the theory is to replace (6.1) by

$$I(s,\xi,\epsilon)=\int_{u_1}^{u_2}\frac{du}{u+iq}e^{2i\xi(u-s)^2}e^{-4i\xi\epsilon u}f(u,s), \tag{6.73}$$

where ϵ specifies the matching conditions and $\epsilon=0$ corresponds to nominal matching. This can be written

$$I(s,\xi,\epsilon)=e^{-2i\xi\epsilon^2-4i\xi\epsilon s}$$

$$\times\int_{u_1}^{u_2}\frac{du}{u+iq}e^{2i\xi(u-s-\epsilon)^2}f(u,\, s+\epsilon)e^{-4\epsilon u}, \tag{6.74}$$

which is very similar to $I(s+\epsilon,\, \xi)$, the difference consisting of a phase factor of magnitude unity and a slightly different slowly varying factor inside the integral. A simple prescription suffices to generalize our principal result (6.69) to the case of arbitrary ϵ:

The second argument s in $f(u,s)$ remains simply s, while every other s is replaced by

$$s\rightarrow s+\epsilon. \tag{6.75}$$

The Gaussian factor e^{-4s^2} in the intensity remains unchanged.

The effect of ϵ upon the intensity pattern can be appreciated quite simply from the dominant term in the intensity, (5.29) modified according to (6.75), which is proportional to

$$e^{-4s^2-8\beta s-8\beta\epsilon}\theta(s+\epsilon). \tag{6.76}$$

This function is shown in Fig. 22 for $\beta=0.318$ and $\epsilon=0.6$, 0.25, 0, and -0.4. The curve for $\epsilon=0$ is identical with the dominant term shown in Fig. 20. By consulting Fig. 20 we can imagine how the edge structure might appear for each case shown in Fig. 22. The dotted curve is the locus of edge heights $\exp(-4s^2)$. It will be seen that the heights and widths vary considerably as

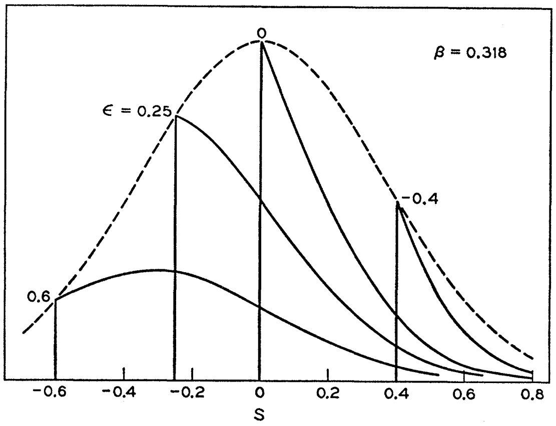

FIG. 22. The dominant term in the intensity according to (6.76) for four phase matching conditions specified by $\epsilon=0.6$, $\epsilon=0.25$, $\epsilon=0$ the nominal matching case, and $\epsilon=-0.4$. For the definition of ϵ see (8.9).

the pattern moves. The case $\epsilon=0.25$ corresponds to the maximum power to be discussed in Sec. 8.

6.6 Summary

In this section we have obtained corrections to the limiting result of Sec. 5 which give two additional terms in the field which we have called edge fine structure and surface fine structure. Inclusion of the edge fine structure gives a continuous intensity which is very steep at $s=0$ and has maxima and minima on the bright side $s>0$. The surface fine structure causes additional very weak intensity modulations. The edge structure is very closely related to the diffraction pattern of a physical straight-edged screen. This edge pattern is limited to a definite region. The general criterion for well developed edge structure is that this region must be large enough to contain fringes. It is shown that absorption will ordinarily have no effect on edge structure but may affect surface structure. It is shown that well-developed edge structure can be observed outside the crystal, but not in the limit of infinite distance from the crystal.

7. PARTIALLY DEVELOPED EDGE STRUCTURE

7.1 External Region

We shall now discuss the SHG pattern in a limit which is very accessible experimentally and much simpler mathematically than the limits (5.17) or (5.20) which lead to the well-developed edge structure. Let us suppose we have a finite crystal of length l and a given laser beam focused at f with confocal parameter b; we then ask for the field $E_2(x,y,z)$ *outside the crystal* in the limit

$$z\to\infty \quad b,\, f,\, l \text{ fixed}. \tag{7.1}$$

We have already observed in (6.72) that the criterion for a well developed edge ceases to be satisfied in this limit. The theory of the pattern in this limit is quite simple regardless of the length of the crystal. A pattern is obtained which is independent of z when expressed in the angle variables s, t of (5.32). The pattern may be regarded as the *Fraunhofer diffraction* pattern produced by the field pattern on the exit surface of the crystal. The well developed edge structure, on the other hand, corresponds to *Fresnel diffraction.* We shall call the pattern in the limit (7.1) the *partially developed* edge structure, since the edge remains very distinct separating the pattern into bright and dim regions, but the structure characteristic of Fresnel diffraction by an edge disappears, and its place is taken by greatly enhanced surface structure. Actually the theory applies to a wide gamut of conditions giving patterns which range from extremely sharp edges to extremely small asymmetry about $s=0$. The parameters which determine the pattern are β of (5.5), κ of (7.32), and

$$\xi=\frac{2}{b}(l-f), \quad \zeta=\frac{2}{b}f. \tag{7.2}$$

This is not really a new definition of ξ but merely the maximum value, and the most relevant value, which (4.2) assumes within the crystal.

The field outside the crystal is given by (5.35) and the intensity by (5.36) with $I(s,\xi_e)$ defined by (6.1). In $I(s,\xi_e)$ we may omit the phase factor $\exp(2i\xi_e s^2)$ and write

$$I(s,\xi_e)=\int_{u_1}^{u_2}\frac{du}{u+iq}e^{2i\xi_e u^2-4i\xi_e su}f(u,s), \tag{7.3}$$

where

$$f(u,s)=e^{cu}e^{4us-2u^2}, \tag{7.4}$$

and ξ_e is defined by (4.21) and c, q, u_1, u_2 by (5.33). From (4.21) and (5.33) it follows

$$\xi_e u_1=-\beta\xi, \quad \xi_e u_2=\beta\zeta. \tag{7.5}$$

Notice that (7.5) is constant and unaffected by the limit (7.1). This sets the present case apart from that treated previously which satsified (5.19) or (5.22) as limits were taken according respectively to (5.17) or (5.20). The limit (7.1) does not cause $I(s,\xi_e)$ to approach arbitrarily closely to the discontinuous dominant term $I_d(s,\xi_e)$ as in (5.37). The sharpness of the edge is determined by (7.5) and is independent of z. We shall see, however, that if a well developed edge is produced at l and a partially developed edge at z, the partially developed edge is always *sharper* in the angle variable s than the well developed edge. From (7.5) we have

$$\begin{aligned} 2\xi_e u_1^2 &= 2\beta^2\xi^2/\xi_e \xrightarrow[z\to\infty]{} 0, \\ 2\xi_e u_2^2 &= 2\beta^2\zeta^2/\xi_e \to 0. \end{aligned} \tag{7.6}$$

This gives us the essential approximation of the theory of this section, which is to neglect $2i\xi_e u^2$ in the exponent of (7.3). Clearly in the external far field (5.30) $2u^2$ is even smaller than $2\xi_e u^2$, and can therefore be neglected in (7.4). Also $4us$ can be neglected, since $|u|\ll 1$ according to (7.5) and (5.30), and s is effectively limited to the region $|s|<1$ by the factor $\exp(-4s^2)$ in (5.36). Thus (7.3) becomes, finally,

$$I(s,\xi_e)=\int_{u_1}^{u_2}\frac{du}{u+iq}e^{cu-4i\xi_e su}. \tag{7.7}$$

Notice that this does not actually depend upon ξ_e. With no absorption we would set $c=0$ according to (5.33). With c retained in (7.7) absorption is treated exactly for all s unlike the theory of the preceding section where absorption was included in the slowly varying factor $f(u,s)$ and treated approximately.

A convenient criterion for the validity of (7.7) is

$$\xi_e>2\beta^2\xi^2,\quad \xi_e>2\beta^2\zeta^2. \tag{7.8}$$

It is illuminating to interpret this as a sweeping away of the edge structure. It is clear that the Fresnel edge structure vanishes when $2i\xi_e u^2$ is neglected. According to (6.61), the edge structure is limited to the domain $u_1<s<u_2$. Thus as ξ_e increases, $|u_1|$ and u_2 decrease eventually sweeping the edge structure away. The criterion for this to happen is approximately

$$s^{(1)}>|u_1|,\quad s^{(1)}>u_2, \tag{7.9}$$

where $s^{(1)}$ is the first edge peak given by (6.40) with ξ_e for ξ. This criterion can be written

$$\xi_e>\frac{8}{3\pi}\beta^2\xi^2,\quad \xi_e>\frac{8}{3\pi}\beta^2\zeta^2, \tag{7.10}$$

which is essentially equivalent to (7.8). In addition we also require the external far field condition (5.30). There is no requirement on ξ or ζ or the absorption parameter c. Thus we can discuss the cases of thin crystals and highly absorbing crystals with the SHG viewed from the external far field. For use in designing experiments it is convenient to write (7.8) in the form of a single condition on $z-l$

$$z-l>(\beta^2/n)(l^2/b)-l/2n \tag{7.11}$$

obtained by setting $\xi=\zeta$.

Let us write (7.7) in the form

$$I(s,\xi_e)=-2\pi i H(4\beta s,\tfrac{1}{2}\alpha b,\zeta,\xi), \tag{7.12}$$

where the function

$$H(\sigma,\kappa,\zeta,\xi)=\frac{1}{2\pi}\int_{-\zeta}^{\xi}\frac{d\tau}{1+i\tau}e^{-\kappa\tau+i\sigma\tau} \tag*{(7.13)*}$$

is in a convenient form for numerical computation. By the contour integration methods applied to (5.24) we can obtain the limiting form

$$\lim_{\xi\to\infty}H(\sigma,0,\xi,\xi)=e^{-\sigma}\theta(\sigma)\equiv H_d(\sigma), \tag{7.14}$$

which is equivalent to (5.25). This result is the basis for the appearance of an *edge*. It follows that we expect a definite edge when

$$\kappa=0,\quad \xi\gg 1,\quad \zeta\gg 1. \tag{7.15}$$

As in (6.3) we write (7.13) as the sum of an edge term and fine structure terms (when $\kappa=0$)

$$H=H_d+H_\xi+H_\zeta, \tag{7.16}$$

where

$$\begin{aligned}H_\xi&=-\frac{1}{2\pi}\int_{\xi}^{\infty}\frac{d\tau}{1+i\tau}e^{i\sigma\tau},\\ H_\zeta&=-\frac{1}{2\pi}\int_{-\infty}^{-\zeta}\frac{d\tau}{1+i\tau}e^{i\sigma\tau}.\end{aligned} \tag{7.17}$$

In view of (7.15) we can write (7.17) in the approximate form

$$\begin{aligned}H_\xi&=-\frac{1}{2\pi}\int_{\xi}^{\infty}\frac{d\tau}{i\tau}e^{i\sigma\tau},\\ H_\zeta&=-\frac{1}{2\pi}\int_{-\infty}^{-\zeta}\frac{d\tau}{i\tau}e^{i\sigma\tau},\end{aligned} \tag{7.18}$$

which can readily be expressed in terms of the *sine integral* and *cosine integral* functions[17] (z real)

$$\begin{aligned}\mathrm{Si}(z)&=\int_0^z\frac{\sin\tau}{\tau}d\tau=\frac{\pi}{2}-\int_z^\infty\frac{\sin\tau}{\tau}d\tau\\ &=\frac{\pi}{2}\frac{z}{|z|}-\frac{\cos z}{z}+\cdots,\\ \mathrm{Ci}(z)&=-\int_z^\infty\frac{\cos\tau}{\tau}d\tau=-\int_0^z\frac{(1-\cos\tau)}{\tau}d\tau\\ &\qquad+\ln z+0.5772\cdots\\ &=\frac{\sin z}{z}+i\pi\theta(-z)+\cdots.\end{aligned} \tag{7.19}$$

Thus we obtain the *approximate* analytic representation, valid for the case (7.15),

$$\begin{aligned}H(\sigma,0,\zeta,\xi)&=e^{-\sigma}\theta(\sigma)-\tfrac{1}{2}[\theta(\sigma)-\theta(-\sigma)]\\ &\quad+\frac{1}{2\pi}[\mathrm{Si}(\sigma\zeta)+i\,\mathrm{Ci}(\sigma\zeta)+\mathrm{Si}(\sigma\xi)-i\,\mathrm{Ci}(\sigma\xi)],\end{aligned} \tag{7.20}$$

---

[17] E. Jahnke and F. Emde, *Tables of Functions* (Dover Publications, Inc., New York, 1945), Sec. I.

which, despite the step functions $\theta(\sigma)$ and $\theta(-\sigma)$, is actually continuous at $\sigma=0$. The asymptotic form of (7.20) is

$$H(\sigma,0,\zeta,\xi)=e^{-\sigma}\theta(\sigma)-\frac{\cos\sigma\xi+i\sin\sigma\xi}{2\pi\sigma\xi}-\frac{\cos\sigma\zeta-i\sin\sigma\zeta}{2\pi\sigma\zeta}+\cdots. \quad (7.21)$$

The result of greatest interest is the asymptotic form of $|H|^2$

$$|H(\sigma,0,\zeta,\xi)|^2=e^{-2\sigma}\theta(\sigma)+\frac{1}{4\pi^2\sigma^2}\left(\frac{1}{\zeta^2}+\frac{1}{\xi^2}\right)-e^{-\sigma}\theta(\sigma)\frac{\cos\sigma\xi}{\pi\sigma\xi}-e^{-\sigma}\theta(\sigma)\frac{\cos\sigma\zeta}{\pi\sigma\zeta}+\frac{\cos\sigma(\xi+\zeta)}{2\pi^2\sigma^2\zeta\xi}+\cdots. \quad (7.22)^*$$

The third and fourth terms represent *surface fine structure* associated with the exit and incident surfaces, respectively, like the fourth and fifth terms of (6.69). The last term gives a structure visible on the dim side $\sigma<0$ which depends on the crystal thickness l but not on the focal position f. We may expect the structure on the bright side $\sigma>0$ to be rather complex except in the symmetric case $\xi=\zeta$.

The conditions for the validity of (7.22) are, in addition to (7.15),

$$|\sigma\xi|>\pi, \quad |\sigma\zeta|>\pi, \quad (7.23)$$

which are equivalent to (6.64). When (7.23) is not satisfied near $\sigma=0$ the pattern can be obtained by squaring (7.20).

In the presence of absorption the method based on (7.16) and (7.17) cannot be applied. Let us assume

$$|\kappa|\ll1, \quad |\kappa\zeta|\gg1, \quad |\kappa\xi|\gg1 \quad (7.24)$$

and write (7.13) in three parts

$$\int_{-\zeta}^{\xi}=\int_{-\zeta}^{-\zeta'}+\int_{-\zeta'}^{\xi'}+\int_{\xi'}^{\xi}, \quad (7.25)$$

where ζ', ξ' are as yet unspecified and will drop out of our final result. We only require that

$$\begin{gathered}\xi'\gg1, \quad \zeta'\gg1\\ |\kappa\zeta'|<1, \quad |\kappa\xi'|<1.\end{gathered} \quad (7.26)$$

It is then appropriate to replace the second term of (7.25) with $H_d(\sigma)$ defined in (7.14). We can completely neglect the first term of (7.25) if $\kappa<0$ or the third term if $\kappa>0$. We suppose $\kappa>0$ and write approximately

$$\int_{-\zeta}^{-\zeta'}\frac{d\tau}{1+i\tau}e^{-\kappa\tau+i\sigma\tau}\approx\frac{e^{\kappa\zeta-i\sigma\zeta}}{i\zeta(-\kappa+i\sigma)}. \quad (7.27)$$

TABLE II. Parameters used in the calculation of Figs. 23–29. Last row gives the relative peak intensities of Figs. 23–26 if they were to be plotted on the same intensity scale.

Fig.	23	24	25	26	27	28	29
β	0.318	0.318	0.318	0.318	0.318	0.318	0.0197
ξ	253	253	253	253	614	9.5	253
ζ	361	361	361	361	0	9.5	253
κ	0	0.004	−0.01	−0.02	0	0	0
relative intensity	1	0.3	0.015	0.0017			

It then follows that for $\kappa>0$ and (7.24) valid

$$|H(\sigma,\kappa,\zeta,\xi)|^2=e^{-2\sigma}\theta(\sigma)+\frac{1}{4\pi^2(\sigma^2+\kappa^2)\zeta^2}e^{2\kappa\zeta}+e^{-\sigma}\theta(\sigma)e^{\kappa\zeta}\frac{\kappa\sin\sigma\zeta-\sigma\cos\sigma\zeta}{\pi\zeta(\sigma^2+\kappa^2)}+\cdots. \quad (7.28)$$

Similarly for $\kappa<0$ and (7.24) valid

$$|H(\sigma,\kappa,\zeta,\xi)|^2=e^{-2\sigma}\theta(\sigma)+\frac{1}{4\pi^2(\sigma^2+\kappa^2)\xi^2}e^{-2\kappa\xi}-e^{-\sigma}\theta(\sigma)e^{-\kappa\xi}\frac{\kappa\sin\sigma\xi+\sigma\cos\sigma\xi}{\pi\xi(\sigma^2+\kappa^2)}+\cdots. \quad (7.29)$$

We see that absorption tends to accentuate the structure associated with one or the other of the surfaces on the bright side and suppress the structure on the dim side. Further details on $H(\sigma,\kappa,\zeta,\xi)$ are given in the Appendix. We shall frequently use the parameters

$$\sigma=4\beta s, \quad \kappa=\tfrac{1}{2}\alpha b \quad (7.30)$$

as well as those of (7.2) in discussing the intensity pattern.

According to (5.36) and (7.12) the *intensity* in the external far field (7.8) is given by

$$S(s,t)=4\pi K\frac{P_1{}^2k_1{}^2}{\xi_e{}^2}\frac{4n}{(n+1)^2}e^{-2\alpha_1f-\alpha_2(l-f)}\times e^{-4(s^2+t^2)}|H(4\beta s,\tfrac{1}{2}\alpha b,\zeta,\xi)|^2. \quad (7.31)^*$$

In the remainder of this section we shall illustrate partially developed edge structure by means of numerically computed curves of the intensity as a function of s in Figs. 23–29. The curves were computed by the methods explained in the Appendix except for Fig. 29 which was computed from (7.20). For each calculation the parameters β, ξ, ζ, κ are specified in Table II. The dimensionless variable s is related to the transverse distance x from the beam axis and the distance $z-l$ of the observer from the crystal surface by (5.32).

We take as our first example the experimental arrangement (6.45) which gives rise at the exit surface of the crystal to the well-developed edge shown in Fig. 20. If we observe the pattern at a distance $z-l>48$ cm the criterion (7.8) for a partially developed edge pattern will be satisfied. In Fig. 23 the solid curve is the intensity function $e^{-4s^2}|H|^2$. In order to show the structure near the edge the figure had to be restricted to a small range in s. For comparison with Fig. 20 the first edge fringe is shown to the proper scale by the dotted curve. Also shown is the discontinuous first term of (7.22). To show the dim-side structure ($s<0$) due to the last term of (7.22) a magnified ($\times 100$) curve has been included. The theoretical peak positions corresponding to the maxima of $\cos\sigma(\xi+\zeta)$ are indicated by vertical lines. The structure on the bright side $s>0$ arising from the third and fourth terms of (7.22) is complicated because $\xi\neq\zeta$. Notice that the partially developed edge is much sharper in the angle variable s than the associated well developed edge.

Absorption is specified by the parameter

$$\kappa=\tfrac{1}{2}b\alpha=\tfrac{1}{2}b(\alpha_1-\tfrac{1}{2}\alpha_2)\,, \tag{7.32}$$

which may have either sign. Calculation shows that the value $\kappa=4\times 10^{-4}$ appropriate to (6.45) is too small to have any noticable effect on Fig. 23. To show the effects of absorption we consider several larger values in Figs. 24, 25, and 26. In Fig. 24 we see that the bright-side structure is simpler in form and greater in amplitude than in Fig. 23. This agrees with (7.28) which predicts that the structure is governed by $-\cos\sigma\zeta$; the maxima of $-\cos\sigma\zeta$ are indicated by vertical lines in Fig. 24. The dim-side structure is much weaker, and the intensity level relative to the peak intensity is higher than in Fig. 23. In Fig. 25 we illustrate the effects of changing the sign as well as increasing the magnitude of κ. The bright-side structure now has a very large amplitude and is governed by $-\cos\sigma\xi$, the maxima of which are indicated by lines. The dim-side structure has vanished and the intensity level relative to the peak is higher than in Fig. 24. At still higher absorption in Fig. 26 we see the amplitude of the bright-side structure beginning to decline as a large central peak of width $|\kappa|$ emerges corresponding to the second term of (7.29). Figures 23, 24, 25, and 26 have been normalized to the same peak height for convenience in presentation; on an absolute basis the corresponding peak intensities would be approximately in the ratio 1, 0.3, 0.015, and 0.0017 taking into account the absorption factor in (7.31) as well as $|H|^2$. Figure 26 corresponds to an absorption

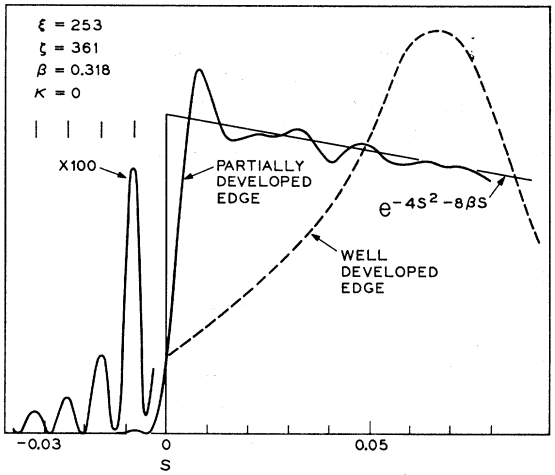

FIG. 23. Intensity distribution in a typical partially developed edge is shown by the solid curve according to (7.31). Assuming the experimental arrangement (6.45), the pattern of Fig. 20 would change into that shown above at distances from the exit surface $z-l>48$ cm. For comparison the first edge fringe of Fig. 20 is shown dashed. A magnified curve ($\times 100$) shows the dim-side structure. Theoretical peak positions according to (7.22) are indicated by lines. Also shown is the dominant term identical with that of Fig. 20. Curve was computed on an IBM 7094 computer by the methods described in the Appendix.

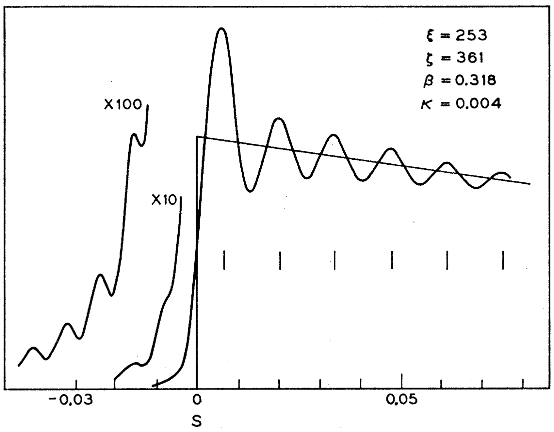

FIG. 24. Partially developed edge with absorption of the laser beam about 10 times that of ADP, other parameters same as Fig. 23. Bright-side structure is due to the incident surface as predicted by (7.28) and the dominant term appears smaller than in Fig. 23.

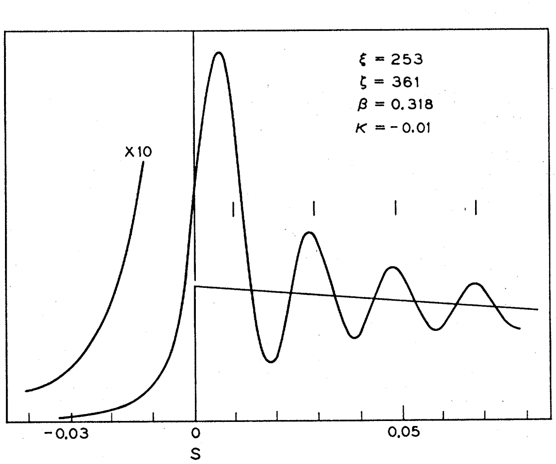

FIG. 25. Partially developed edge with strong absorption of the second harmonic. Bright-side structure is due to the exit surface as predicted by (7.29), and the dominant term appears smaller than in Fig. 24. Dim-side structure has disappeared.

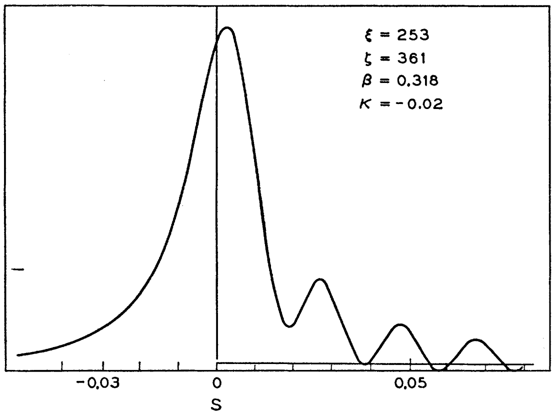

FIG. 26. Partially developed edge with strong absorption of the second harmonic. At this level of absorption the width of the central maximum is determined by $|\kappa|$, and the dominant term is insignificant.

coefficient for the second harmonic $\alpha_2 \sim 14.6$ cm^{-1} if α_1 may be neglected.

The partially developed edge structure depends upon the position of the focus in the crystal. If the focus were adjusted exactly in the center of the crystal (again neglecting absorption) the bright-side structure would become regular and the minima of the dim-side structure would go to zero in Fig. 23. Another interesting case is that in which the focus lies at the incident surface as in Fig. 27. Lines indicate the positions of the dim-side peaks of Fig. 23. We see that the dim-side structure is still detectable, although very weak, and is approximately reflected on the bright side. The asymmetry of the pattern has nearly disappeared. The same pattern is obtained by focusing on the exit surface.

The appearance of a pronounced edge requires

$$4\beta\xi > 2\pi\,, \quad 4\beta\zeta > 2\pi \tag{7.33}$$

as well as

$$\xi \gg 1\,, \quad \zeta \gg 1\,, \tag{7.34}$$

although the theory remains valid even when these conditions are not satisfied. As an illustration of the pattern produced by smaller values of ξ, ζ we present Fig. 28. We imagine the crystal of (6.45) to be replaced by a much thinner one having $l = 0.052$ cm, and the focus is adjusted to the center of the crystal. The pattern has the usual dim side structure shown by the magnified ($\times 100$) curve. The structure on the bright side consists of very slight oscillations above and below the curve $e^{-4s^2-8\beta s}$ representing the dominant term. The pattern is nearly symmetrical in appearance but the peak is shifted toward the bright side. The line indicates the maximum of $-\cos\sigma\xi$. The criterion for the partially developed edge structure (7.8) is satisfied in this case very close to the exit surface

$$z - l > 0.016 \text{ cm}\,. \tag{7.35}$$

In this case there is no well-developed edge associated with the partially developed edge.

7.2 Internal Region

As the preceding example shows it may not always be necessary to go to the external far field to satisfy the conditions for a partially developed edge. Under certain conditions the partially developed edge can be observed right on the *exit surface* of the crystal. Let us consider the far field (5.1) inside the crystal where the field is given by (5.11), the intensity by (5.14), and $I(s,\xi)$ by (6.1). No assumption need be made, as in (5.2), about the position f of the focus. From our discussion of (7.3) it is clear that the partially developed edge in the interior of the crystal corresponds to neglecting $2i\xi u^2$ in the exponent of (6.1), which is valid if

$$2\xi u_1{}^2 \ll 1\,, \quad 2\xi u_2{}^2 \ll 1\,. \tag{7.36}$$

This condition is essentially the opposite of (6.66). In the external far field the corresponding conditions (7.6) are automatically satisfied, as we have seen, regardless of ξ and β in the limit (7.1). In the *interior* in the far field (7.36) will not be satisfied unless

$$\beta^2 \ll 1\,. \tag{7.37}$$

Even then (7.36) will ultimately break down in the far field limit (5.18), (6.66) will become valid, and the well developed edge will be obtained. For a given crystal, however, the far field limit must be taken by (5.20) which has no effect on either (6.66) or (7.36). Let us suppose that ρ is so small that (6.68) breaks down

$$0 < \rho < (2/k_1 l)^{1/2}\,. \tag{7.38}$$

It follows that at least one of the conditions (6.66) breaks down so we assume at least one of the conditions (7.36) is satisfied, regardless of what lens is used or where the focus is located. This condition was nearly achieved in the example of Fig. 28 ($l = 0.052$ cm) for

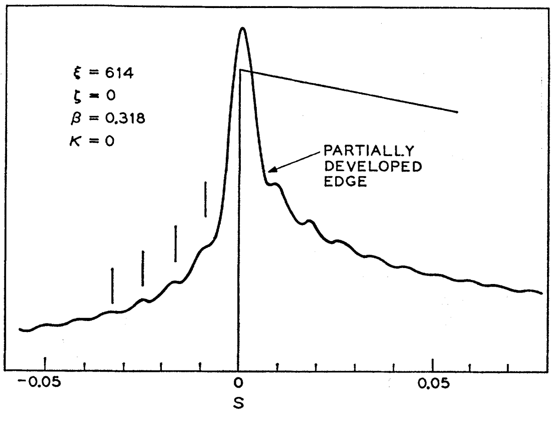

FIG. 27. Partially developed edge with no absorption and the focus at the incident surface.

which (7.38) becomes $\rho<0.027$ rad; for the crystal of (6.45) ($l=1.7$ cm) it becomes $\rho<0.0048$ rad$=0.26°$. Recently it has been shown by Miller, Boyd, and Savage[18] that by suitable choice of laser wavelength and crystal-temperature index-matching conditions can be achieved in LiNbO$_3$ with $\rho=0$. By adjusting the temperature any value of ρ can be selected over a range of the order $0\leq\rho<0.03$ rad. It follows that the partially developed edge structure could readily be obtained at the exit surface of a crystal of LiNbO$_3$.

Let us first assume that both conditions (7.36) are satisfied as well as (5.1); it follows that

$$|u_1|\ll 1,\quad |u_2|\ll 1, \tag{7.39}$$

and (6.2) can be written

$$f(u,s)=e^{cu}, \tag{7.40}$$

where now c is given by (5.8). We now write (6.1) in the form [dropping $\exp(2i\xi s^2)$]

$$I(s,\xi)=\int_{u_1}^{u_2}\frac{du}{u+iq}e^{cu-4i\xi su} = -2\pi i H(4\beta s,\tfrac{1}{2}\alpha b,\zeta,\xi). \qquad (7.41)^*$$

This formally resembles the external case (7.12), but it should be noted that (7.41) depends explicitly on ξ whereas (7.12) is independent of ξ_e.

An example of internal partially developed edge structure is shown in Fig. 29. The value of ξ is the same as in Fig. 20 to facilitate comparison with the well developed edge, but we have chosen the symmetric case $\xi=\zeta$ to give a simple and recognizable bright-side structure. Lines indicate the maxima of $-\cos\sigma\xi$ on the bright side ($s>0$) and the maxima of $\cos2\sigma\xi$ on the dim side, which are the approximate theoretical peak positions according to (7.22). Actually the bright-side peaks, except the first, are obscured by the rapidly decaying Gaussian factor e^{-4s^2} and only appear as shoulders. The edge fringe region (6.61), due to the small value of β, is too small to contain any edge structure. The first two edge fringes of Fig. 20 are shown to the proper scale by the dotted curve.

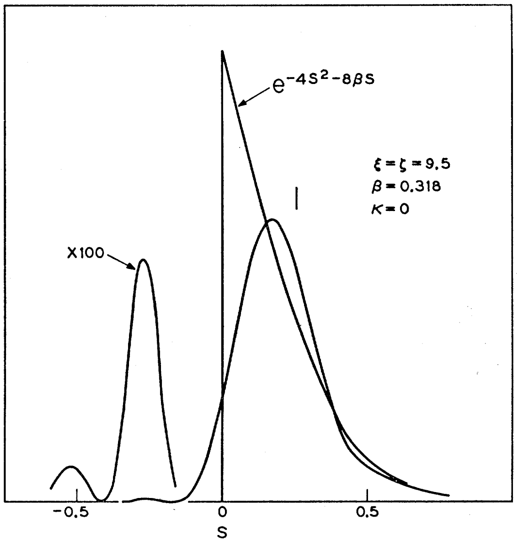

FIG. 28. Partially developed edge for a relatively thin crystal.

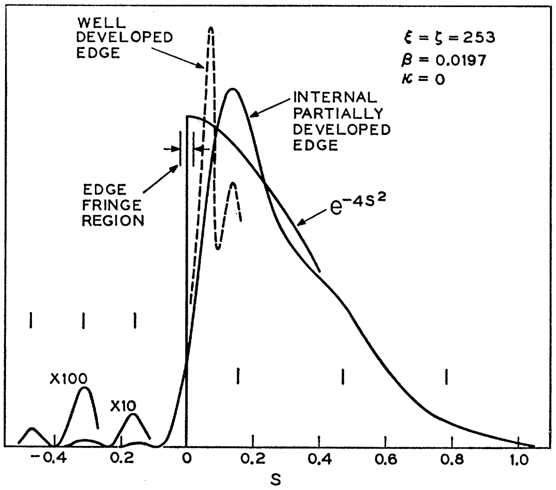

FIG. 29. Internal partially developed edge observed at the exit surface of the crystal. The well-developed edge structure for $\xi=253$ shown by the dashed curve is not seen because it falls outside the edge fringe region (6.61).

7.3 Mixed Structure

There is another kind of partially developed edge structure which can occur either inside our outside the crystal when only one of the conditions (7.36) or (7.8) respectively is satisfied. Let us consider the interior of the crystal and place the focus relatively near the incident surface so that (7.15) holds but we have

$$f\ll l-f. \tag{7.42}$$

We can then have the mixed condition

$$2\xi u_1^2\gg 1,\quad 2\xi u_2^2\ll 1. \tag{7.43}$$

It is reasonable to call the pattern in this case partially developed even though it exhibits some properties of the well developed edge. The bright side $s>0$ cannot have edge fringes because the edge fringe region (6.61) is cut off by the small value of u_2; this is the significance of the second condition (7.43). On the other hand the large value of $|u_1|$ means that the dim side $s<0$ may be considered to lie entirely in the edge-structure region. Therefore the dim-side surface fringes characteristic of partially developed edge structure will not be seen. Thus the pattern is in a sense partially developed on the

---

[18] R. C. Miller, G. D. Boyd, and A. Savage, Appl. Phys. Letters 6, 77 (1965).

bright side and well developed on the dim side. The pattern may be deduced from (6.62) which is valid in the domains specified by (6.63) and (6.64). We may ignore the region $|s|<(\pi/4\xi)^{1/2}$ which includes u_2 since we know it contains at most only a very weak u_1 structure. For simplicity we neglect the insignificant u_1 term and write (6.62) in the form

$$\begin{aligned} I(s,\xi) &\underset{(s>u_2)}{=} -2\pi i e^{2i\xi s^2-4\beta s}-\frac{e^{2i\xi(u_2-s)^2}}{4i\xi u_2 s}+\cdots \\ &\underset{(s<0)}{=} \frac{f(s,s)}{s}\left(\frac{\pi}{2\xi}\right)^{1/2} e^{i\pi/4}-\frac{e^{2i\xi(u_2-s)^2}}{4i\xi u_2 s}+\cdots. \end{aligned} \tag{7.44}$$

We have put $f(u_2,s)=1$ but retained $f(s,s)$, and put $u_2-s=-s$ in the denominator of the u_2 term. It now follows immediately that the bright-side structure is given by (except for the factor e^{-4s^2})

$$(2\pi)^{-2}|I(s,\xi)|^2 \underset{(s>0)}{=} e^{-2\sigma}-e^{-\sigma}\frac{\cos\sigma\zeta}{\pi\sigma\zeta}+\cdots, \tag{7.45}$$

where $\sigma=4\beta s$. This is identical with the partially developed edge structure (7.22) in the approximation $\xi\rightarrow\infty$, which corresponds to our dropping the u_1 term in (6.62). On the dim side the structure is due to interference between the edge term and the u_2 term which leads again to the seventh term of (6.69) just as in well developed edge structure; in the present case, however, the u_2 term is larger than the edge term so we cannot neglect its square as was done in (6.69). Thus we obtain

$$\begin{aligned} (2\pi)^{-2}|I(s,\xi)|^2 &\underset{(s<0)}{=} \frac{1}{4\pi^2\sigma^2\zeta^2} \\ &-\left(\frac{2\pi}{\xi}\right)^{1/2}\frac{f(s,s)}{\sigma\zeta}\sin\left[\frac{\sigma^2\xi}{2\beta^2}-\sigma\zeta-\frac{\pi}{4}\right]+\cdots. \end{aligned} \tag{7.46}$$

The first term appears also in (7.22), and shows that the average intensity level on the dim side is characteristic of partially developed edge structure, but the second term giving the location of peaks appears in (6.69) and is characteristic of well-developed edge structure. For the external region there is a condition completely analogous to (7.43) which does not require a separate discussion.

We can also have the other mixed condition

$$2\xi u_1^2\ll 1,\quad 2\xi u_2^2\gg 1 \tag{7.47}$$

if

$$f\gg l-f. \tag{7.48}$$

We continue to assume (7.15). There is now plenty of room for edge fringes on the bright side, but it is no longer true that the edge term (order $\xi^{-1/2}$) in (6.62) is larger than the u_1 term (order ξ^{-1}). The edge term may be neglected if, as we now assume,

$$(8\pi\xi u_1^2)^{1/2}\ll 1, \tag{7.49}$$

which is consistent with (7.47) but somewhat stronger. Thus (6.62) reduces to

$$\begin{aligned} I(s,\xi) &\underset{(s>0)}{=} -2\pi i e^{2i\xi s^2-4\beta s}+\frac{e^{2i\xi(u_1-s)^2}}{4i\xi u_1 s}+\cdots \\ &\underset{(s<u_1)}{=} \frac{e^{2i\xi(u_1-s)^2}}{4i\xi u_1 s}-\frac{e^{2i\xi(u_2-s)^2}}{4i\xi u_2 s}+\cdots. \end{aligned} \tag{7.50}$$

We have neglected the weak u_2 term on the bright side but retained it on the dim side since the first two terms of (6.62) vanish. Finally we have on the bright side

$$(2\pi)^{-2}|I(s,\xi)|^2 \underset{(s>0)}{=} e^{-2\sigma}-e^{\sigma}\frac{\cos\sigma\xi}{\pi\sigma\xi}, \tag{7.51}$$

which agrees with (7.22) in the limit $\zeta\rightarrow\infty$. The dim side also agrees with (7.22) in as much as we have retained the two surface terms in (7.50). Actually there would be a weak edge structure superposed on the bright-side surface structure, but the first few fringes would be missing because of the proximity of the cut off u_1 which takes effect over a range of order $(\pi/4\xi)^{1/2}$. We have not included a term to describe these fringes in (7.51) because it is difficult to treat the effect of the cut off within the frame work of our asymptotic approximations. Obviously there is a condition for the external region analogous to (7.47).

7.4 Summary

In this section we have described four kinds of partially developed edge structure associated with the conditions (7.8), (7.36), (7.43), and (7.47). Of these the third and fourth are actually mixed types in which the pattern retains some features of well-developed edge structure. We have found that partially developed edge structure is always observed outside the crystal at a sufficient distance specified by (7.11). It may also be observed inside the crystal or at the exit surface if the double-refraction angle ρ measured by $\beta=\rho/\delta_0$ is sufficiently small. Partially developed edge structure is surface fine structure; the absence of edge fine structure may be ascribed to the shrinkage of the edge-structure region (6.61) until it cannot contain any edge fringes. We have presented a detailed study of the effects of absorption on the pattern. This completes our discussion of fine structure, which is objective (3) mentioned in the introduction.

8. POWER AND OPTIMUM INDEX MATCHING

8.1 Generalization of Theory

We have so far assumed that the laser beam is *nominally* index matched, which means that the index vector $\boldsymbol{\eta}_1$ defined in (3.3) and representing the nominal wave vector $2\mathbf{k}_1$ of the polarization beam falls on the index surface as shown in Fig. 17. More generally let us define

$$2\mathbf{k}_N=(\omega/c)\mathbf{N}n_2(\mathbf{N}), \tag{8.1}$$

where $n_2(\mathbf{N})$ is the index in the direction $\mathbf{N}$. By definition $2\mathbf{k}_N$ is matched. We can rewrite (3.13) using k_N instead of k_1

$$2\psi_K=(K_z-2k_N+\rho K_x)z+\frac{K_x^2+K_y^2}{4k_N}z+i\alpha z. \tag{8.2}$$

We shall call

$$\Delta\mathbf{k}=2\mathbf{k}_1-2\mathbf{k}_N \tag{8.3}$$

the *adjustment*. Since we limit ourselves to beams normal to the surface the adjustment is always in the normal direction and is measured by a scalar quantity Δk. We write (8.2) in the form

$$2\psi_K=(K_z-2k_1+\rho K_x)z+\frac{K_x^2+K_y^2}{4k_1}z+i\alpha z+\Delta kz, \tag{8.4}$$

where we have replaced k_N by k_1 in the quadratic term on the assumption that $\Delta k\ll 2k_1$. We see that the adjustment can be included formally in our previous theory based upon (3.13) simply by defining α to be complex

$$\alpha\rightarrow\alpha-i\Delta k. \tag{8.5}$$

This substitution in the Green's function (3.23) gives

$$G(\mathbf{r},\mathbf{r}')=\left(\frac{\omega n}{2\pi ic}\right)\frac{1}{Z}e^{-\frac{1}{2}\alpha_2 Z}e^{2ik_N Z+ik_1(X^2+Y^2)/Z}. \tag{8.6}$$

The second harmonic field inside the crystal (4.19) becomes

$$\mathbf{E}_2(\mathbf{r})=\frac{\boldsymbol{\gamma}\cdot\mathbf{P}_0e^{-\frac{1}{2}\alpha_2 z}e^{2ik_1 z}}{1+i\xi}\int_0^z dz'\frac{e^{-\alpha z'+i\Delta kz'}}{1+i\xi'}\times\exp\left\{-\frac{2[(x-\rho Z)^2+y^2]}{w_0^2(1+i\xi)}\right\}. \tag*{(8.7)*}$$

The far-field approximation (5.11) is still valid providing $I(s,\xi)$ given previously by (5.12) and then (6.1) is further generalized to include the adjustment

$$I(s,\xi,\epsilon)=\int_{u_1}^{u_2}\frac{du}{u+iq}e^{-4i\xi\epsilon u}e^{2i\xi(u-s)^2}f(u,s), \tag*{(8.8)*}$$

where

$$\epsilon=b\Delta k/8\beta=w_0\Delta k/4\rho \tag{8.9}$$

measures the adjustment and $f(u,s)$ is still given by (6.2) with the ordinary real α. The dominant term is obtained by dropping $2i\xi u^2$ and replacing u_1, u_2 with infinite limits as explained in (5.17) to (5.25)

$$I_d(s,\xi,\epsilon)=-2\pi ie^{2i\xi s^2}e^{-4\beta(s+\epsilon)}\theta(s+\epsilon). \tag*{(8.10)*}$$

We have already discussed the implications of (8.8) in regard to the pattern. In (6.74) we have shown that the edge and the fine structure are shifted along the s axis a distance $-\epsilon$. The affects of this on the pattern can be appreciated from Fig. 22 showing the dominant term in the intensity $e^{-4s^2}|I_d(s,\xi,\epsilon)|^2$ for several values of ϵ.

8.2 Power when $\varrho\neq 0$

There is a very practical connection between the adjustment and the power. We shall show that the power

$$P_2=\int\int dxdyS(s,t,\epsilon)=\delta_0^2(z-f)^2\int\int dsdtS(s,t,\epsilon) \tag{8.11}$$

as a function of ϵ assumes its maximum value for some value of $\epsilon>0$. The physical reason for this has been pointed out following (4.3). In practice there is usually no way of knowing ϵ due to the fact that it depends very sensitively on the orientation of the crystal. However, ϵ can be fixed by adjusting the crystal orientation for *maximum power*, a logical procedure that an experimenter would want to do anyway. The value of ϵ can then be deduced from (8.11). We shall call this the *optimum adjustment* and the corresponding value of ϵ will be written ϵ_m. In this section we shall discuss $P_2(\epsilon)$ for the case in which the SHG pattern has a pronounced edge. For consideration of the power the fine structure can then be ignored and $I(s,\xi,\epsilon)$ approximated by (8.10). In this approximation there is no distinction between a well developed and a partially developed edge. It is sufficient to consider the intensity at the exit surface of the crystal which according to (5.14) and (8.10) is given by ($\beta\neq 0$)

$$S(s,t,\epsilon)\simeq 4\pi K\frac{P_1^2k_1^2}{\xi^2}e^{-2\alpha_1 f-\alpha_2(l-f)}\times e^{-4(s^2+t^2+2\beta s)}e^{-8\beta\epsilon}\theta(s+\epsilon), \tag*{(8.12)*}$$

with ξ defined by (7.2). The conditions required to produce a *sharp edge* may be deduced from (6.66), (7.33), (7.43), and (7.47); they may be presented compactly as follows:

$$\text{either}\quad \xi\beta^2\gg 1\quad\text{or}\quad 4\beta\xi\gg 2\pi$$

and

$$\text{either}\quad \xi\beta^2\gg\frac{l-f}{f}\quad\text{or}\quad 4\beta\zeta\gg 2\pi. \tag{8.13}$$

This includes the well-developed edge and the three types of partially developed edge which can occur within the crystal. The power relation $P_2(\epsilon)$ which we shall obtain is that which an experimenter would observe by adjusting the orientation of his crystal. Our results are not adequate to discuss the optimization of power in a crystal of given length with respect to choice of lens or position of focus, which will be discussed elsewhere.

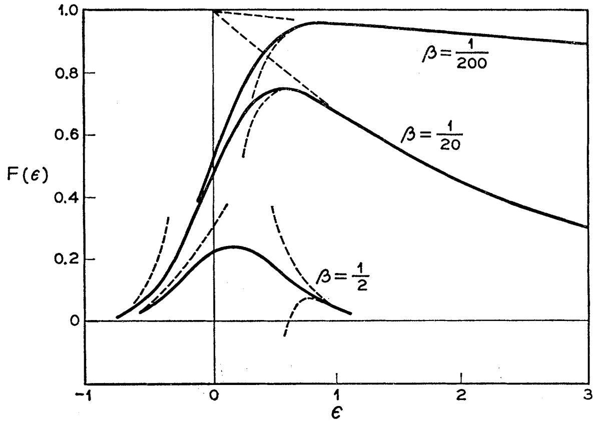

FIG. 30. Function $F(\epsilon)$ defined by (8.15) for three values of β. The dashed curves on the left show the asymptotic approximation (8.18). Dashed curves on the right show the exponential first term of (8.17) as well as the whole expression. Note how $F(\epsilon)$ for $\beta \ll 1$ has the appearance of a "rounded off" step function with exponential tail.

From (5.21), (8.11), and (8.12) the power can be written ($\beta \neq 0$)

$$P_2 = KP_1^2 e^{-2\alpha_1 f - \alpha_2(l-f)} \frac{4\pi^2}{\delta_0^2} \cdot F(\epsilon,\beta). \qquad (8.14)^*$$

The dependence on ϵ is contained in the function

$$F(\epsilon,\beta) = \tfrac{1}{2}[1 - \operatorname{erf}(2\beta - 2\epsilon)] e^{4\beta^2 - 8\beta\epsilon}, \qquad (8.15)$$

with

$$\operatorname{erf}(x) = \frac{2}{\sqrt{\pi}} \int_0^x e^{-\tau^2} d\tau = \frac{x}{|x|}\left(1 - \frac{e^{-x^2}}{|x|\sqrt{\pi}} + \cdots\right). \qquad (8.16)$$

The asymptotic behavior of $F(\epsilon,\beta)$ is given by

$$F(\epsilon,\beta) \approx e^{4\beta^2 - 8\beta\epsilon} - \frac{e^{-4\epsilon^2}}{4\pi^{1/2}(\epsilon-\beta)} \qquad \epsilon - \beta > \tfrac{1}{2}, \qquad (8.17)$$

$$F(\epsilon,\beta) \approx \frac{e^{-4\epsilon^2}}{4\pi^{1/2}(\beta-\epsilon)} \qquad \beta - \epsilon > \tfrac{1}{2}. \qquad (8.18)$$

We have indicated ($\beta \neq 0$) in (8.14) since $\beta = 0$ would violate the essential conditions (8.13) for an edge. We shall later consider the case $\beta = 0$ separately to show that as far as power is concerned it joins on satisfactorily to (8.14).

Figure 30 shows $F(\epsilon)$ for three values of β, $\beta = 0.5$, 0.05, 0.005. The dotted curves on the left show the asymptotic form (8.18) where it deviates from the true curves. On the right are shown both the exponential first term of (8.17) and the sum of the two terms. It will be seen that $F(\epsilon)$ has a single maximum which serves to define an *optimum adjustment* for the production of maximum total power. It is evident that for $\beta \ll 1$ this optimum adjustment is very important and gives approximately twice the power of the *nominal adjustment* $\epsilon = 0$. For $\beta > \frac{1}{2}$ the optimum adjustment is far less significant. We see that the peak value of $F(\epsilon)$ decreases monotonically with increasing β. For $\beta \ll 1$ (8.17) is valid in the vicinity of the peak but for $\beta \geq \frac{1}{2}$ it is definitely not valid. The peak always occurs for $\epsilon > 0$. The complete absence of structure in (8.15) and in Fig. 30 is due to the dominant-term approximation (8.12).

The maximum $F_m = F(\epsilon_m)$ at the position ϵ_m satisfies

$$F_m(\beta) = \frac{e^{-4\epsilon_m^2}}{4\pi^{1/2}\beta}. \qquad (8.19)$$

For $\beta > 1$ we may expect $\epsilon_m \ll 1$ so we obtain

$$F_m(\beta) \approx \frac{1}{4\pi^{1/2}\beta} \quad (\beta > 1). \qquad (8.20)$$

For $\beta > 1$ we may expect (8.18) to become valid in the vicinity of the peak. The maximum of (8.18) falls approximately at

$$\epsilon_m \approx \frac{1}{8\beta} \quad (\beta > 1), \qquad (8.21)$$

which justifies the assumption in (8.20) that $\epsilon_m \ll 1$. A special solution of (8.19) is

$$\begin{aligned} \epsilon_m = \beta &= \frac{1}{2\sqrt{\pi}} = 0.282, \\ F_m &= \tfrac{1}{2} e^{-1/\pi} = 0.364. \end{aligned} \qquad (8.22)$$

It follows that

$$\begin{aligned} F_m > 0.364, &\quad \epsilon_m > \beta \; (\beta < 0.282) \\ F_m < 0.364, &\quad \epsilon_m < \beta \; (\beta > 0.282). \end{aligned} \qquad (8.23)$$

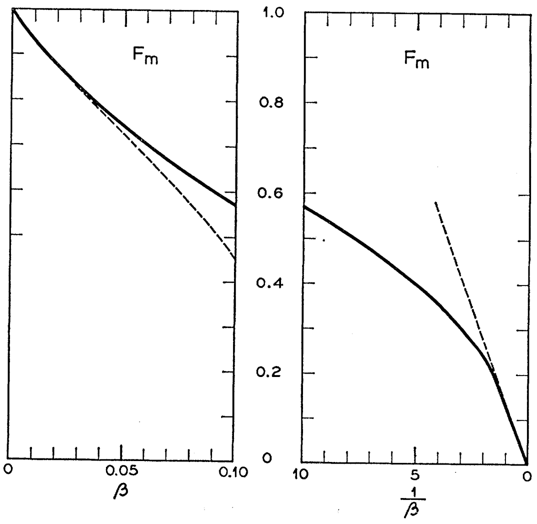

FIG. 31. Maximum value of $F(\epsilon)$ as a function of β. Dashed curve on left is (8.27), that on right is (8.20).

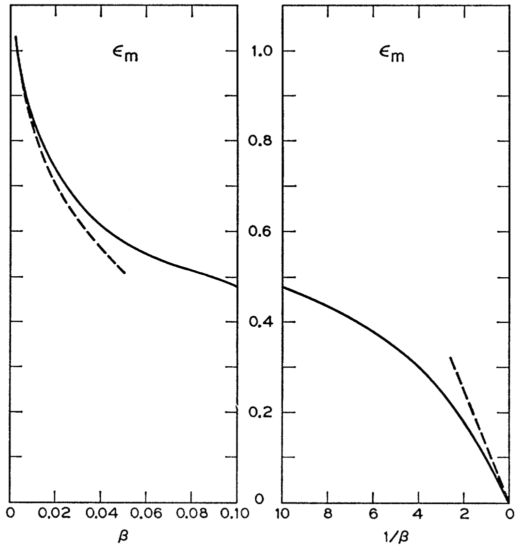

FIG. 32. Optimum adjustment as a function of β, defining the optimum matching case. For definition of ϵ see (8.9).

For $\beta\ll1$ we may write (8.17) in the form

$$F(\epsilon,\beta)\approx e^{-8\beta\epsilon}\frac{e^{-4\epsilon^2}}{4\pi^{1/2}\epsilon}\quad(\beta\ll1,\ \ \epsilon>\tfrac{1}{2}).\tag{8.24}$$

Figure 30 shows that the peak F_m lies very close to the curve $e^{-8\beta\epsilon}$ for $\beta<1/20$. From (8.19) it then follows that

$$e^{-8\beta\epsilon_m}\approx e^{-4\epsilon_m^2+4a},\tag{8.25}$$

where a is defined by

$$e^{4a}=\frac{1}{4\beta\sqrt{\pi}}.$$

It follows that $4\epsilon_m^2-8\beta\epsilon_m-4a\approx0$, which gives

$$\epsilon_m\approx a^{1/2}\quad(\beta<1/20).\tag{8.26}$$

Now F_m may be obtained from (8.24)

$$F_m(\beta)\approx\exp(-8\beta a^{1/2})-\beta a^{-1/2}\quad(\beta<1/20).\tag{8.27}$$

Although ϵ_m defined by (8.26) diverges as $\beta\rightarrow0$

$$\epsilon_m\xrightarrow[\beta\rightarrow0]{}\infty\tag{8.28}$$

for all practical purposes one may take

$$\epsilon_m\approx1\quad(\beta<1/200)\tag{8.29}$$

since $F(\epsilon)$ can increase at the most only 0.23% by making $\epsilon>1$. We see that

$$\begin{gathered}F_m\xrightarrow[\beta\rightarrow0]{}1,\\ F_m\xrightarrow[\beta\rightarrow\infty]{}0,\\ 0\leq F_m\leq1.\end{gathered}\tag{8.30}$$

Figure 31 shows the optimized power represented by F_m as a function of β from $0\leq\beta\leq0.1$ and of $1/\beta$ from $10\leq1/\beta\leq0$. Dotted curves indicate asymptotic formulas (8.27) on the left and (8.20) on the right. Figure 32 shows the optimum adjustment ϵ_m as a function of β with asymptotic formulas (8.25) and (8.21) on the left and right, respectively.

8.3 Large Double Refraction $\rho\gg\delta_0$

The case $\beta\gg1$ makes contact with the work reported in BADK, where unfocused laser beams were used and β ranged from 91 to 213. This case applies to the typical experimental situation. We see from Fig. 30 that for such large values of β the distinction between nominal and optimum matching, which was not discussed in BADK, becomes immaterial. We found in BADK that double refraction reduces the power for parallel beams of finite aperture, especially when

$$l_a<l,\tag{8.31}$$

where the *aperture length* is defined by

$$l_a=(\pi)^{1/2}(w_0/\rho).\tag{8.32}$$

In the case of focused beams with $b\ll l$ we may expect that (8.31) should be replaced by

$$l_a<b.\tag{8.33}$$

It follows from (4.7) and (8.32) that (5.5) and (8.9) can be written in terms of l_a

$$\begin{gathered}\beta=\frac{\rho}{\delta_0}=\frac{\sqrt{\pi}}{2}\frac{b}{l_a},\\ \epsilon=\frac{l_a}{4\sqrt{\pi}}\Delta k.\end{gathered}\tag{8.34}$$

Thus when (8.33) is satisfied F_m is given by (8.20) which can be written

$$F_m\approx\frac{l_a}{2\pi b}.\tag{8.35}$$

The complete expression for the power (8.14) neglecting absorption can be written

$$P_2=KP_1^2\frac{l_fl_a}{w_0^2}\quad(l_a<l_f),\tag{8.36}$$

where we define

$$l_f=\pi b/2.\tag{8.37}$$

This relation has a very simple interpretation in the light of Eqs. (3.32) and (3.39) of BADK which in the aperture effect limit $l_a\ll l$ reduce to

$$P_2=KP_1^2\frac{ll_a}{w_0^2}.\tag{8.38}$$

Thus (8.36) is the power that would be generated by a parallel beam of spot size w_0 in a crystal of length l_f providing $l_f \gg l_a$. We may regard l_f as the *effective length* of the focus. Although the concept of an equivalent parallel beam acting over an effective length reasonably accounts for the power, it does not predict the correct pattern for a focused beam.

8.4 No Double Refraction $\rho=0$

The case $\beta \ll 1$ is of great interest because the power proportional to F_m monotonically increases with $1/\beta$ according to Fig. 31. Here we are regarding the beam, and hence δ_0, as fixed while ρ is reduced to zero

$$\rho \rightarrow 0. \qquad (8.39)$$

This process can actually be carried out in $LiNbO_3$ by changing the temperature.[18] The maximum power according to (8.14) obtained in the limit (neglecting absorption) is

$$\begin{aligned}\max P_2 = \lim_{\substack{\rho\to 0\\ \alpha_1=\alpha_2=0}} P_2 &= KP_1^2(4\pi^2/\delta_0^2)\\ &= KP_1^2(4l_f^2/w_0^2). \qquad (8.40)\end{aligned}$$

There may be some question regarding the validity of this result, however, because in the limit (8.39) the criterion (8.13) for the validity of (8.14) breaks down. We must, therefore, consider separately the case $\beta=0$. In (8.7) we set $\rho=0$ and obtain

$$\begin{aligned}\mathbf{E}_2(\mathbf{r}) = \boldsymbol{\gamma}\cdot\mathbf{P}_0 e^{-\alpha_1 f-\frac{1}{2}\alpha_2(l-f)} e^{2ik_1 l}\\ \times\frac{\pi b}{1+i\xi}\exp\left[-\frac{2(x^2+y^2)}{w_0^2(1+i\xi)}\right]\cdot H(\sigma,\tfrac{1}{2}\alpha b,\zeta,\xi), \qquad (8.41)^*\end{aligned}$$

where H is the function defined by (7.12) and now

$$\sigma=\tfrac{1}{2}b\Delta k=4\beta\epsilon \qquad (8.42)$$

measures the adjustment. There should be no confusion with our previous use of σ in (7.30). We see that by means of the H function the case $\rho=0$ can be evaluated for arbitrary ζ, ξ without the need for a far field or near field approximation. In the far field (8.42) takes the form (5.11) with the substitution

$$I(s,\xi,\epsilon) \rightarrow -2\pi i e^{2i\xi s^2} H(\sigma,\tfrac{1}{2}\alpha b,\zeta,\xi). \qquad (8.43)$$

The power according to (5.14), (8.11), and (8.43) can now be written

$$P_2=KP_1^2 e^{-2\alpha_1 f-\alpha_2(l-f)}\frac{4\pi^2}{\delta_0^2}\cdot|H|^2, \qquad (8.44)^*$$

which agrees in form with (8.14) except that the Δk dependence is now contained in $|H|^2$ instead of $F(\epsilon)$. This same result can be obtained directly from (8.41) without the far field approximation, and therefore is valid also in the near field.

We see from (7.21) that H contains structure associated with the finite values of ζ, ξ. If we let $\zeta=\xi\rightarrow\infty$ this structure can be neglected and H can be written simply $H_a(\sigma)$ defined by (7.14). Thus in (8.44) we may put

$$|H|^2 \rightarrow e^{-2\sigma}[\theta(\sigma)]^2. \qquad (8.45)$$

We now make contact with $F(\epsilon)$ by noting that $F(\epsilon)$ has the appearance of a "rounded off" step function with exponential tail when $\beta \ll 1$. The rounding occurs over a region $|\epsilon|<1$, which in the parameter $\sigma=4\beta\epsilon$ becomes vanishingly small in the limit $\beta\rightarrow 0$. Thus (8.17) and (8.18) become

$$F(\epsilon)=F(\sigma/4\beta)\xrightarrow[\beta\to 0]{} e^{-2\sigma}\theta(\sigma). \qquad (8.46)$$

It may easily be verified that (8.45) and (8.46) give the correct values for the nominal matching case $\sigma=0$

$$\begin{aligned}\lim_{\beta\to 0} F(0)&=\tfrac{1}{2},\\ |H(0)|^2&=\tfrac{1}{4}.\end{aligned} \qquad (8.47)$$

This shows that a consideration of the power limited to the case $\sigma=0$, aside from being experimentally meaningless, does not behave properly in the limit $\beta\rightarrow 0$. When we consider the case of optimum matching, however, the maxima of (8.45) and (8.46) are equal

$$\lim_{\beta\to 0} F_m=|H|_m^2=1 \qquad (8.48)$$

which assures the validity of (8.40).

8.5 Summary

In this section we have generalized our previous results to remove the assumption of nominal matching conditions. The phase matching is specified by Δk called the adjustment, or by dimensionless quantities $\epsilon=b\Delta k/8\beta$ and $\sigma=\frac{1}{2}b\Delta k$. It is shown that the power $P_2(\epsilon)$ is a function of ϵ having a single maximum which serves to define the optimum adjustment ϵ_m. The optimum power is then proportional to $F_m(\beta)$ shown in Fig. 31. It is shown that the case $\beta\gg 1$ makes contact with the case studied by BADK. The behavior of $F_m(\beta)$ in this case is governed by the double-refraction (aperture) effect for parallel beams, and the SHG takes place over an effective length of the focus which replaces the crystal length in the theory of BADK. The case $\beta\ll 1$ gives the maximum power. Special consideration is given to the case $\beta=0$. A general expression is obtained for the intensity valid at any distance from the focus. In the far field with fine structure neglected this expression agrees with the general theory ($\beta\neq 0$) except at exact nominal matching $\Delta k=0$. For the optimum power the general theory in the limit $\beta\rightarrow 0$ agrees with the theory for $\beta=0$. The optimum adjustment ϵ_m is the phase matching condition obtained experimentally when the crystal orientation is adjusted for maximum power. It is shown that the distinction between nominal matching $\epsilon=0$ and optimum matching $\epsilon=\epsilon_m$ is immaterial for the case considered by BADK.

9. COMPARISON OF THEORY AND EXPERIMENT

The nature of the experimental results has already been reviewed qualitatively and the data has been presented in Sec. 2. In this section we shall present a quantitative comparison of theory and experiment. As an aid in understanding the results which we shall draw from the theory we give a glossary of all the theoretical symbols that will appear in this section.

x,z	coordinates of the observer, see Fig. 17;
l,f	crystal length (l) and distance of focus (f) from incident surface;
w_0	spot size (radius) of laser beam at focus;
b	confocal parameter, see (4.1);
δ_0	far-field diffraction (half) angle in the crystal, see (4.7) and (5.21);
ξ,ζ	see (7.2);
ρ	double-refraction angle, see Fig. 17;
$\beta=\rho/\delta_0$;	
u_1,u_2	see (5.33);
ξ_e	see (4.21);
n	refractive index;
ω	second-harmonic angular frequency;
Δk	measures departure from nominal matching see (8.3);
$\epsilon=b\Delta k/8\beta$;	
ϵ_m	optimum value of ϵ for maximum power;
s	a dimensionless coordinate used to describe the SHG pattern in the x direction, see (5.32);
j	an ordinal number 1, 2, 3, $\cdots$ used to designate fringes;
$s^{(j)}$	the s coordinate of the edge fringes, see (6.40);
$R(j)$	fringe-spacing ratio, see (6.41);
L	focal length of a lens, see (3.46);
m	magnification, see (3.48).

9.1 Position of Edge

We begin with the position of the edge relative to the ρ line through the focus under optimum matching conditions. The experimental arrangement is shown in Fig. 1, the experimental constants are given in Table I, and we consider Fig. 6. The unfocused laser beam is described by the parameters[1]

$$\begin{aligned}&\lambda_1(\text{air})=1.153\times10^{-4}\ \text{wavelength},\\&\delta(\text{air})=2.08\times10^{-4}\ \text{(diffraction angle)},\\&w(\text{air})=0.177\text{(spot radius)},\\&b(\text{air})=1706\text{(confocal parameter)},\\&\qquad\text{(all lengths in cm)}.\end{aligned}\tag{9.1}$$

Since $\delta(\text{air})$ is extremely small it can be neglected in determining the effect of the focusing lens; the lens focuses the beam at its focal point a distance $L=3.2$ from its second principal plane. The lens used was quite thin and it can be assumed that both principal planes coincide with the lens rim. Before reaching the focal point of the lens the beam enters the crystal after traveling a distance $a_2=0.2$. The position of the focus in the crystal relative to the incident surface and exit surface is given by

$$\begin{aligned}f&=n(L-a_2)=4.5,\\l-f&=10.4-4.5=5.9.\end{aligned}\tag{9.2}$$

The parameters of the focus in the crystal are

$$\begin{aligned}\delta_0&=w(\text{air})/(nL)=0.0362\ \text{rad},\\w_0&=\lambda_1(\text{air})/(n\delta_0\pi)=6.75\times10^{-4},\\b&=2w_0/\delta_0=0.0373.\end{aligned}\tag{9.3}$$

Note that w_0 is the same in the crystal or in air. With no slit and no imaging lens the second harmonic power P_2 could be measured. The crystal orientation was adjusted for maximum P_2, thereby establishing *optimum matching conditions*. With the imaging lens in place, the exit surface of the crystal is imaged onto the plane of the traveling slit with a magnification

$$|m|=11\div6.8=1.62,\quad\text{(Fig. 6)}.\tag{9.4}$$

The laser and second harmonic intensity distributions as measured with the traveling slit are shown in Fig. 6. Two edge fringes are well resolved in the SHG pattern. The beam axis can be located in Fig. 6 by estimating the center of the laser intensity distribution. The ρ line can be located by measuring from the beam axis the distance

$$\text{(beam axis)}-(\rho\ \text{line})=|m|\rho(l-f)=0.29.\tag{9.5}$$

It so happens that the ρ line falls on the *second edge fringe* for the particular conditions of this experiment.

This result was checked by another experiment (Fig. 5) in which the imaging lens was removed and the slit placed as close as possible to the exit surface. The light passing through the slit was collected and conducted to the detector by a Lucite light pipe. The second edge fringe could just barely be resolved. Although it gave lower resolution this experiment had the advantage of avoiding any dependence on the optical magnification (9.4) in calculating the position of the ρ line. The results, however, were in agreement with those obtained with the lens.

We compare this result with theory by computing the position of the second edge fringe relative to the edge, and the position of the edge relative to the ρ line. For this purpose we need

$$\begin{aligned}\xi&=(2/b)(l-f)=316,\\\beta&=\rho/\delta_0=0.83.\end{aligned}\tag{9.6}$$

Evidently the condition (6.66) is strongly satisfied. It now follows from (6.40) that the jth edge fringe is located relative to the edge at

$$s^{(j)}=0.1[(j-1)+0.375]^{1/2} \tag{9.7}$$

and in particular

$$s^{(2)}=0.12. \tag{9.8}$$

In the same variable s the edge relative to the ρ line ($s=0$) is located at

$$s(\text{edge})=-\epsilon_m(\beta) \tag{9.9}$$

according to (8.12) for optimum matching conditions $\epsilon=\epsilon_m(\beta)$. From Fig. 32

$$\epsilon_m(\beta)=\epsilon_m(0.83)=0.12. \tag{9.10}$$

We have extracted (9.7) from the theory of well developed edge structure in Sec. 6 and (9.9) from the theory of optimum matching in Sec. 8. Combining these theories leads to the prediction that the ρ line should fall on the second edge fringe in agreement with experiment.

9.2 Movement of the Edge

The edge can be moved relative to the beam axis by very small rotations of the crystal on the rotatable stage. This effect is shown in Fig. 15. The patterns labelled $(a\cdots g)$ correspond to the crystal orientations so labeled in Fig. 14. In these experiments the power P_2 could be measured by removing the slit, and crystal orientations were selected giving $\frac{1}{4}$, $\frac{1}{2}$, $\frac{3}{4}$, 1, $\frac{3}{4}$, $\frac{1}{2}$, and $\frac{1}{4}$ times the maximum power. The focus was located close to the incident surface and the pattern was measured with a traveling slit in the air beyond the exit surface; the relevant dimensions are

$$\begin{aligned} f&=0.3,\\ l-f&=10.1,\\ z-l&=15.8, \end{aligned} \tag{9.11}$$

and the parameters of the focus are

$$\begin{aligned} \delta_0&=0.0150\text{ rad},\\ w_0&=16\times10^{-4},\\ b&=0.21. \end{aligned} \tag{9.12}$$

The parameters in the theory of partially developed edge structure outside the crystal are

$$\begin{aligned} \xi_e&=327,\\ \xi&=96,\\ \zeta&=2.9,\\ \beta&=1.95,\\ u_1&=-0.58,\\ u_2&=0.017. \end{aligned} \tag{9.13}$$

Thus we have

$$\begin{aligned} 2\xi_e u_1^2&=220\gg1,\\ 2\xi_e u_2^2&=0.19\ll1, \end{aligned} \tag{9.14}$$

which satisfies the conditions (7.43) for a particular kind of partially developed edge structure. A consideration of the criteria for a pronounced edge (7.33) and (7.34)

$$\begin{aligned} 4\beta\zeta&=23>2\pi\\ \zeta&=2.9>1 \end{aligned} \tag{9.15}$$

leads us to expect a recognizable edge in the pattern but not an extremely abrupt edge. The beam axis can be located from the laser pattern, and the edges can be located by extrapolating the steep sides of the SHG patterns to the abscissa. The displacement x of the edge from the beam axis is plotted as a function of crystal angle θ in Fig. 16. The angle $\theta=0$ is the optimum matching case which gives maximum P_2. The dashed line is the best linear fit to the data.

To compare these results with theory, we deduce the relationship between the adjustment Δk and a rotation $\Delta\theta$ of the crystal; from Fig. 17 it follows that

$$\Delta k=(\omega/c)\rho\Delta\theta+\text{const}. \tag{9.16}$$

If we measure θ from the optimum matching condition, (8.9) becomes

$$\epsilon=(\omega/c)(b/8\beta)\rho\theta+\epsilon_m. \tag{9.17}$$

From Fig. 32

$$\epsilon_m(\beta)=\epsilon_m(1.95)=0.055, \tag{9.18}$$

so that (9.17) becomes

$$\epsilon=0.76\theta^\circ+0.055,\quad\text{(Fig. 14)}, \tag{9.19}$$

where θ° is in degrees. It now follows from (5.32) and (9.9) that the x coordinate of the edge is given by

$$\begin{aligned} x&=\rho(l-f)-\epsilon\delta_0[l-f+n(z-l)]\\ &=0.30-0.52\epsilon\\ &=0.27-0.39\theta^\circ\quad\text{(Fig. 16)}. \end{aligned} \tag{9.20}$$

The last relation is the solid line of Fig. 16. We see that the slope of the theoretical line is in excellent agreement with experiment. In the absolute position of the theoretical line there is a discrepancy with the data of about 0.08 cm. In view of the agreement between theory and experiment in Fig. 6 for the position of the edge, we attribute the discrepancy in absolute position in Fig. 16 to low resolution and the lack of an abrupt edge in the pattern.

9.3 Well-Developed Edge Structure

We now consider Fig. 7. In order to obtain better resolution than in Fig. 6 the exit surface of the crystal was focused onto the plane of the slit with a magnification

$$|m|=a_4/a_3=13/2.8=4.65\quad\text{(Fig. 7)}. \tag{9.21}$$

The other conditions (9.1), (9.2), and (9.3) still apply. The crystal was adjusted for optimum matching conditions. The relation between slit motion ΔX and Δs is

$$\Delta X = |m|\delta_0(l-f)\Delta s = \Delta s. \tag{9.22}$$

The intensity measured with the traveling slit is shown in Fig. 7 plotted on an s scale according to (9.22), (9.9), and (9.10). Except for improved magnification and resolution the pattern is the same as the one in Fig. 6. We have already seen that the second edge fringe falls on the ρ line. The positions of the first eight edge fringes according to (9.7) are indicated by vertical lines. We see that the six fringes which are resolved in the measured curve are in good agreement with the calculated positions. We shall study the fringe positions much more carefully later with the aid of photographs of the SHG. In addition to the fringe positions the general appearance of the pattern is in very good agreement with the expected shape for well developed edge structure shown in Fig. 20.

We now consider the gross intensity distribution in the pattern of Fig. 7. In the theory this is represented by the dominant term in the intensity first derived in (5.29) and generalized to include the adjustment in (8.12). In the theory of well developed edge structure, Sec. 6, the dominant term is the first term of (6.69) and all other terms represent fine structure. Similarly in the theory of partially developed edge structure, Sec. 7, the dominant term is the first term of (7.22). In view of the central role which we have given the dominant term in the theory, it is important that we determine how well it fits the measured pattern. We write (8.12) in the form

$$\mathrm{const} \times e^{-4s^2-8\beta s-8\beta\epsilon}\theta(s+\epsilon) \tag{9.23}$$

and determine the constant by fitting (9.23) to the measured curve in the neighborhood of $s+\epsilon=0.2$ as shown in Fig. 7. The result is shown by the dashed curve. We see that it fits the measured curve very well, in much the same way as the dominant term fits the calculated curve of Fig. 20.

We now consider in much greater detail the fringe positions in the well developed edge pattern. Photographs were taken of the SHG by replacing the slit of Fig. 1 with a photographic film. Again (9.1), (9.2), (9.3) apply, but the magnification was

$$|m| = 6.85 \quad (\text{Figs. } 8, 9). \tag{9.24}$$

The photographic pattern is shown in Fig. 8. At least 22 fringes can be seen in the original film. According to the theory of well developed edge structure the fringe spacing ratio $R(j)$ should obey a universal relation which is independent of m or the parameters (9.6). Therefore we define an experimental $R(j)$ analogous to (6.41)

$$R(j) \equiv \frac{X(j)-X(1)}{X(2)-X(1)}, \tag{9.25}$$

where $X(j)$ is the measured position of the jth fringe on the film. The measured $R(j)$ is shown by the circles in Fig. 10 and the universal function (6.41) is shown by the solid curve. The agreement is quite satisfactory and insures that we are dealing with well developed edge structure. Nevertheless there is a systematic discrepancy outside of experimental error. To explain this, we turn to the more accurate formula for $R(j)$ (6.42) which depends upon the parameters (9.6). The result is indicated by the dashed curve, which actually passes through the circles, but to avoid confusing the figure only its extension has been drawn.

The fringe positions $X(j)$ relative to the first fringe are shown by the circles in Fig. 9. The theoretical fringe positions are given by

$$\begin{aligned} X(j)-X(1)& \\ &= m\delta_0(l-f)(s^{(j)}-s^{(1)}) \\ &= 1.46(s^{(j)}-s^{(1)}) \quad (\text{Fig. } 9) \\ &= 0.146\{[(j-1)+0.375]^{1/2}-(0.375)^{1/2}\} \qquad (9.26) \end{aligned}$$

according to (9.2), (9.3), (9.7), and (9.24). This is plotted as the solid curve of Fig. 9. The agreement between theory and experiment is satisfactory. The systematic discrepancy is of the same kind already found and explained in Fig. 10.

9.4 Partially Developed Edge Structure

Photographs of the harmonic beam taken far from the crystal by direct exposure without an imaging lens are shown in Figs. 11, 12. The focused laser beam is again described by (9.3), and the important theoretical dimensions of the experiment are

$$\begin{aligned} f&=0.61, \\ l-f&=0.61, \\ z-l&=18. \end{aligned} \tag{9.27}$$

The focus was placed in the center of the crystal in order to give a simple structure on the bright side as discussed following (7.22). The bright-side structure is shown in the photograph Fig. 11. Because of the great difference of intensity between the bright and dim sides, it was not possible to observe both bright- and dim-side fringes in the same photograph. The dim-side structure is shown in the photograph Fig. 12. By studying a number of photographs of different exposure it was deduced that the dim-side fringes that could be resolved were the second through the tenth. The first dim-side fringe could not be resolved from the edge in any of the photographs taken. The positions of the fringes are shown by the points in Fig. 13. On the dim side the second fringe was placed arbitrarily on the figure, and the other fringes were then plotted relative to the second fringe. On the bright side the fringes are plotted relative to the first fringe. We see that the fringes fall to an excellent approximation on straight lines, which shows that we are dealing with partially developed edge structure. The criterion (7.11) is "barely" but not strongly satisfied, since

$$(\beta^2/n)(l^2/b)-l/2n=16\,, \tag{9.28}$$

which is near the value of $z-l$. Increasing $z-l$ to satisfy the criterion more strongly proved unnecessary and would have had the disadvantage of reducing the intensity at the film.

We now compare the fringe positions with theory. According to (7.22) the bright-side fringes occur approximately at the maxima of $-\cos\sigma\xi=-\cos4\beta\xi s$. The parameters governing the pattern are

$$\begin{aligned}\beta&=0.775\,,\\ \xi&=33\,,\\ \zeta&=\xi\,.\end{aligned} \tag{9.29}$$

The relation between Δx measured on the film and Δs is

$$\Delta x=\delta_0[l-f+n(z-l)]\Delta s=\Delta s\,. \tag{9.30}$$

Thus relative to the edge the bright-side fringes are located on the film at

$$\begin{aligned}x(j)&=(\pi/4\beta\xi)[1+2(j-1)] \quad \text{(Fig. 13)}\\ &=(0.031)[1+2(j-1)] \quad j=1,2,\cdots\,.\end{aligned} \tag{9.31}$$

Similarly, the dim-side fringes are approximately at the maxima of $\cos2\sigma\xi=\cos8\beta\xi s$. Denoting the bright side by $x>0$ and $j=1,2,\cdots$ and the dim side by $x<0$ and $j=-1,-2,\cdots$, we have for the dim side (Fig. 13)

$$x(j)=(0.031)j \quad j=-1,-2,\cdots\,. \tag{9.32}$$

The linear relations (9.31) and (9.32) are shown by the lines in Fig. 13. The first bright-side fringe and the second dim-side fringe have been placed on the lines arbitrarily. That the other fringes also fall on the lines indicates excellent agreement between theory and experiment.

9.5 Power and Crystal Orientation

The power as a function of crystal angle is shown as a continuous recorder tracing of the photomultiplier output (no slit) in Fig. 14. Horizontal lines indicate the levels $\frac{1}{4}$, $\frac{1}{2}$, $\frac{3}{4}$ and 1 times the maximum power, and heavy dots denote the angles used to observe the patterns of Fig. 15. The angle scale at the top and the ϵ scale at the bottom are constructed according to (9.19). According to (8.14) P_2 is proportional to the function $F(\epsilon,\beta)$ defined in (8.15). We have calculated $F(\epsilon)$ for $\beta=1.95$ as given in (9.13) and plotted $F(\epsilon)/F_m$ in Fig. 14 by means of crosses. The agreement with the measured curve is satisfactory, especially for $\epsilon>0$. There is a noticeable discrepancy for $\epsilon<0$. We attribute this discrepancy, like that in Fig. 16, to the lack of an abrupt edge in the pattern which has been assumed in the theory.

9.6 Conclusions

The over-all agreement between theory and experiment we consider very satisfactory. We have observed both well developed and partially developed edge structure under conditions in which each would be expected. The position of the edge and the spacings of the fringes have been observed in agreement with theory, as well as the gross intensity distribution. The dependence of power upon crystal angle is also in agreement with theory. The pattern has been observed both on the exit surface of the crystal and in the air far from the crystal, in each case with the expected results. It seems fair to conclude that SHG by focused beams in the presence of double refraction is quite well understood. The experiments have not revealed any significant disagreements with theory. Nevertheless, there are several points in the theory which have not been tested by the experiments reported here: (a) the existence of the edge-fringe region (6.61), (b) the presence of surface fine structure in a well-developed edge, (c) the effect of absorption on partially developed edge structure, (d) internal partially developed edge structure arising from small ρ, (e) partially developed edge structure arising from placing the focus near one crystal surface, and (f) SHG in the absence of double refraction. These points are primarily of academic interest except for (f), which will be treated in another paper dealing with the second-harmonic power and its optimization. From a purely theoretical standpoint, and apart from any comparison with experiment, the formal theory seems to be in a satisfactory state. The far-field approximations giving the edge, the gross intensity distribution, and the fine structure follow in a straightforward way from the rigorous integral representations for the second-harmonic field. From the experimental standpoint the results given here constitute a rather comprehensive survey of SHG by focused beams in the presence of double refraction.

ACKNOWLEDGMENTS

We are pleased to acknowledge the competent technical assistance of J. M. Dziedzic in these experiments. We have also had the benefit of stimulating discussions with J. P. Gordon. Especially helpful was information provided to us prior to publication by R. C. Miller concerning experiments in which the optimum matching case can be clearly distinguished from the nominal matching case. This information led to the emphasis in the present paper on the important role played by the matching conditions.

APPENDIX

To evaluate the function $H(\sigma,\kappa,\zeta,\xi)$ defined in (7.13) the real and imaginary parts must be evaluated separately. Let

$$2\pi H=R+iI\,. \tag{A1}$$

Then

$$\begin{aligned} R(\sigma,\kappa,\zeta,\xi)&=\int_{-\zeta}^{\xi}\frac{d\tau}{1+\tau^2}(\cos\sigma\tau+\tau\,\sin\sigma\tau)e^{-\kappa\tau}, \\ I(\sigma,\kappa,\zeta,\xi)&=\int_{-\zeta}^{\xi}\frac{d\tau}{1+\tau^2}(\sin\sigma\tau-\tau\,\cos\sigma\tau)e^{-\kappa\tau}. \end{aligned} \tag{A2}$$

The best way to plot R, I as functions of one of the variables is to integrate the appropriate differential equations in that variable with other variables as fixed parameters. It follows from (A2) that

$$\begin{aligned} \frac{\partial R}{\partial\sigma}+R&=\frac{e^{\kappa\zeta}}{\sigma^2+\kappa^2}(\kappa\,\cos\sigma\zeta+\tau\,\sin\sigma\zeta) \\ &\quad+\frac{e^{-\kappa\xi}}{\sigma^2+\kappa^2}(\sigma\,\sin\sigma\xi-\kappa\,\cos\sigma\xi), \\ \frac{\partial I}{\partial\sigma}+I&=\frac{e^{\kappa\zeta}}{\sigma^2+\kappa^2}(\sigma\,\cos\sigma\zeta-\kappa\,\sin\sigma\zeta) \\ &\quad-\frac{e^{-\kappa\xi}}{\sigma^2+\kappa^2}(\sigma\,\cos\sigma\xi+\kappa\,\sin\sigma\xi). \end{aligned} \tag{A3}$$

Similar equations in the variable κ may be obtained from the Cauchy-Riemann equations

$$\frac{\partial R}{\partial\kappa}=-\frac{\partial I}{\partial\sigma},\quad \frac{\partial I}{\partial\kappa}=\frac{\partial R}{\partial\sigma}, \tag{A4}$$

for $2\pi H$ as a function of the complex variable $\sigma+i\kappa$. Equations in ζ and ξ follow immediately from (A2) and will not be given here. For $\sigma=\kappa=0$ (A2) can be integrated in closed form

$$\begin{aligned} R(0,0,\zeta,\xi)&=\tan^{-1}\xi+\tan^{-1}\zeta \\ I(0,0,\zeta,\xi)&=\tfrac{1}{2}\ln\left(\frac{1+\zeta^2}{1+\xi^2}\right). \end{aligned} \tag{A5}$$

All integrations will ordinarily start from (A5). The numerical integration can be checked by comparing two or more paths of integration from $\sigma=0$, $\kappa=0$, ζ_0, ξ_0 to the desired σ, κ, ζ, ξ. The system (A3) is stable when integrating in the positive σ direction. Our program based on Hamming's predictor corrector method[19] gives agreement to three or four significant figures for different paths of integration, and can be operated in the negative σ direction in the range $0\geq\sigma>-3$. The range in the positive σ direction is unlimited.

---

[19] R. W. Hamming, J. Assoc. Computing Machinery **6**, 37 (1959).

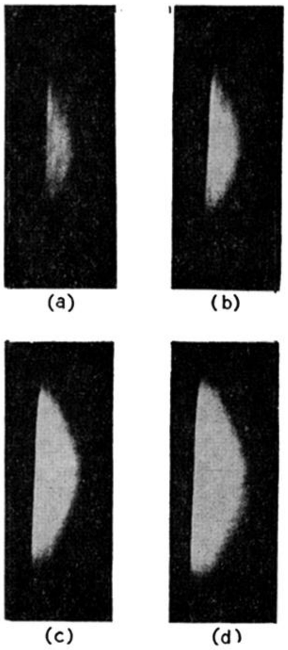
(a) (b) (c) (d)

FIG. 11. Photographs of the harmonic taken by direct exposure without a lens at a distance $a_5 = 18$ cm from the crystal (KDP). The over-all magnification of the reproductions is $\sim 5\times$. Four exposures reveal the bright-side structure. This is partially developed edge structure.

FIG. 12. Photograph as in Fig. 11(d) but with an effective exposure (taking into account film speed) about 1000 times longer. This reveals a series of uniformly spaced fringes on the dim side of the edge. In this photograph, chosen from many taken at different exposures, the first few dim-side fringes are overexposed.

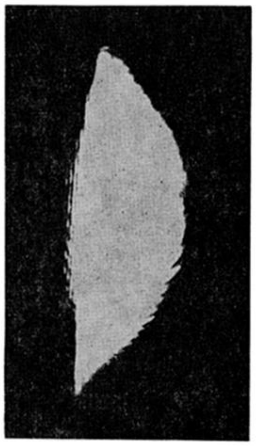

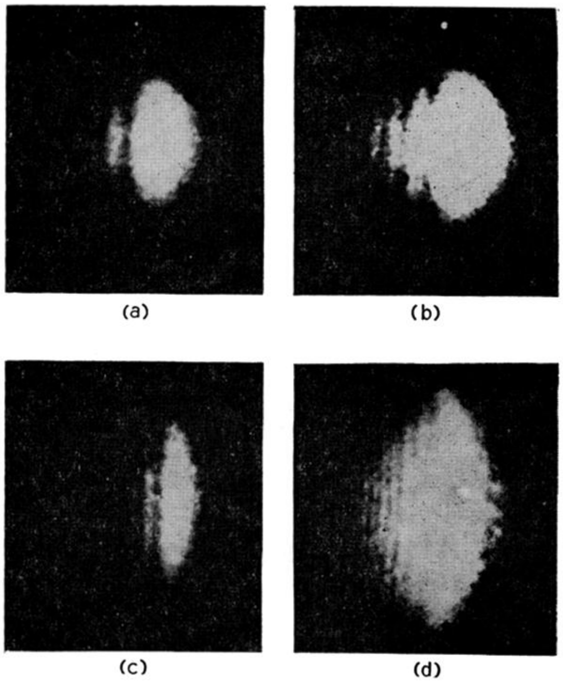

(a) (b)

(c) (d)

FIG. 3. Photographs showing the SHG by a focused beam in ADP in the intermediate field which show the gradual evolution of the edge from the nearly circular pattern of the near field. The pattern of (a), shown at greater exposure in (b), corresponds to $(l-f)\sim 1.5\mathrm{b}$. That of (c), shown at greater exposure in (d), corresponds to $(l-f)\sim 3b$. The edge appears in the shorter exposures as a flattening on the left side. The longer exposures bring out a fine structure which is relatively strong at these intermediate distances, but which becomes very weak in the far field.

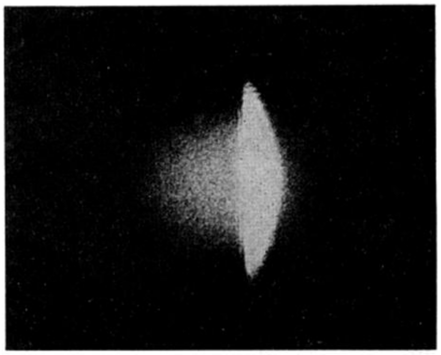

FIG. 4. Photograph showing both the fundamental (circular) and second-harmonic intensity patterns when $(l-f)\sim 10b$. Double refraction in the ADP crystal causes the edge to be displaced from the axis of the fundamental beam.

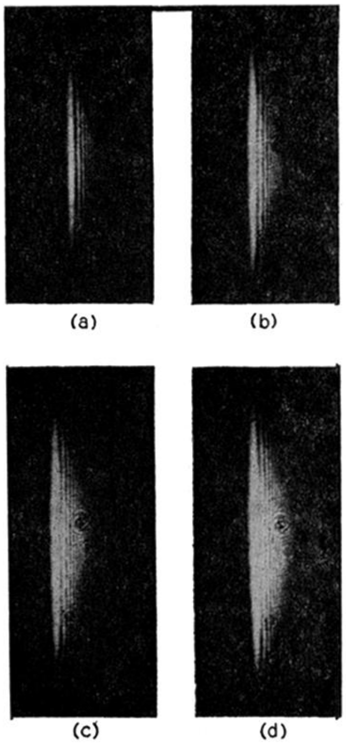
(a) (b) (c) (d)

FIG. 8. Photographs of the harmonic beam scanned in Fig. 5 taken at the exit surface with an optical magnification $m=6.85$. The over-all magnification of the reproduction shown here is ∼14×. Four exposures are shown to reveal the edge structure; longer exposures than (d) give a half-moon appearance like Fig. 4. This is well-developed edge structure.